PREDICTING THE SURFACE AREA TO VOLUME RATIO OF PORES IN IRON RICH SEDIMENTS FROM NUCLEAR MAGNETIC RESONANCE DATA

by

CHRISTINA ELIZABETH TROTTER

B.Sc. (Hons), McMaster University, 1999

A THESIS SUBMITTED IN PARTIAL FULFILLMENT OF

THE REQUIREMENTS FOR THE DEGREE OF

MASTER OF SCIENCE

in

THE FACULTY OF GRADUATE STUDIES

(Department of Earth and Ocean Sciences, Geophysics)

We accept this thesis as conforming

to the required standard

THE UNIVERSITY OF BRITISH COLUMBIA

December 2001

In presenting this thesis in partial fulfillment of the requirements for an advanced degree at the University of British Columbia, I agree that the Library shall make it freely available for reference and study. I further agree that permission for extensive copying of this thesis for scholarly purposes may be granted by the head of my department or by his or her representatives. It is understood that copying or publication of this thesis for financial gain shall not be allowed without my written permission.

Department of Earth and Ocean Sciences

The University of British Columbia

2219 Main Mall

Vancouver, B.C., Canada

V6T 1Z4

Date: December 17 2001

Abstract

In this thesis, I investigated two methods of recovering the surface area to volume ratio (S/V), or pore size distribution, of water filled porous geological materials using Nuclear Magnetic Resonance (NMR) data. The NMR relaxation times T_1 and T_2 depend on the quantity of magnetic sites on the solid pore surface, which is characterized by a parameter called the surface relaxivity, denoted as ρ_1 and ρ_2 respectively. This parameter must be estimated in order to determine the S/V.

Magnetic susceptibility was explored as a method of estimating ρ_1, as it also depends on the amount of magnetic material in a sample. Magnetite and hematite were combined with quartz for measurement. Mixtures of 0.5, 1 and 2 percent magnetite by weight and 2.1, 3, 6, 9, 12, 30 and 60 percent hematite by weight were created.

The magnetic susceptibility and ρ_1 of both the magnetite and hematite mixtures showed good correlation and the results indicate magnetic susceptibility could be used to predict ρ_1 for unconsolidated sediments.

A second method for determining the S/V using T_2 data was studied. T_2 is affected by diffusion of the protons through internal magnetic field inhomogeneities, a process that does not influence T_1. These inhomogeneities can be modeled as an effective gradient, G, which must be estimated.

A parameter estimation inversion code was developed to solve for ρ_2, S/V and G. Evaluation of the algorithm was completed on a synthetic data, which was created with 7% incorporated noise. G and the product of ρ_1 and S/V were reliably recovered but distinguishing between ρ_1 and S/V was not possible for this data set.

The inversion was then carried out on T_2 data from the same hematite samples discussed above. This data set allowed better distinction between ρ_2 and S/V. ρ_2 and G values were within the expected range, but the S/V was larger than expected, which was partly due to the sample geometry. This parameter estimation algorithm shows potential for determining the S/V of a pore space from T_2 measurements, but further experimentation is required.

Table of Contents

List of Tables

List of Figures

Acknowledgements

This research was supported in full by funding to R. Knight under Grant No. DE-FG07-96ER14711, Environmental Management Science Program, Office of Science and Technology, Office of Environment Management, United States Department of Energy (DOE). However, any opinions, findings, conclusions, or recommendations expressed herein are those of the authors and do not necessarily reflect the views of DOE.

I would like to express my appreciation to Dr. Alex Mackay for the use of the NMR Spectrometer, Pinder Dosanjh for the use of the SQUID and Mark Mathner of the Pacific Mineral Museum for supplying the minerals I required.

On a more personal level, I would first like to thank my supervisor Dr. Rosemary Knight for all of her guidance, support and counsel. Her intelligence, determination and outlook on life, has inspired me as a scientist and an individual.

I am exceedingly grateful to Dr. Doug Oldenburg for welcoming me to hang out with the GIF gang. I have benefited tremendously from his inversion expertise and it was a pleasure to work with him and a privilege to have been educated by him.

Thanks to Traci Bryar for all of our NMR talks, she was always willing and more than able to help me out with the fundamentals of this technique. I would also like to express my thanks to her for proof reading this thesis.

Thanks to Parisa Jourabchi for skillfully answering my numerous NMR questions and to Leonard Pasion, Daniel Trad, James Irving and Nigel Phillips for spending many an hour helping me understand inversion. UBC grad students are extremely lucky to work in such a supportive academic environment. The UBC geophysics community is a unique and exceptional group and these five individuals are largely responsible for that.

I'd also like to thank Matthew Skinner for the physics tutorials and for proofing this thesis. And also for making me go down the black diamonds long before I was ready.

Special thanks to the geophysics crowd and the extended geop family for making school such a riot. How is it possible that so many hilarious people ended up in geophysics? I'll miss the daily lunchtime stomachache resulting from uncontrollable laughter. Also, to my fellow rock-physicists, you guys are amazing, thanks for all the advice on school, research and everything else. And also for *finally* ending the ridicule of my store bought contributions to Rosemary's parties.

I'd also like to thank Care, Mere, Ariel, Andrea, Jen, Sue and Tracy for making 3440 so much fun. Hanging out with you girls was a very effective stress reliever.

Finally, I'd like to thank Steve for so many things that including them would double the size of this thesis.

Dedication

For my parents

1 - GENERAL INTRODUCTION

Proton Nuclear Magnetic Resonance (NMR) is a non-invasive geophysical technique that can be used to obtain information about the pore structure of geological materials and the fluids contained within them. Much of the interest in NMR is because it can be used to estimate the surface area to volume ratio of water filled pores in sedimentary materials. This in turn can be used to estimate permeability, a critical parameter in the assessment and modeling of fluid movement in the subsurface.

Unless otherwise specified, the following treatment of NMR theory is a summary of material presented by Ellis (1987), Kleinberg and Horsfield, (1990) and Kleinberg et al. (1994). Please refer to Appendix A for a detailed description of proton NMR relaxation mechanisms and measurements. NMR measures the time it takes water protons to equilibrate with the external environment. Since protons possess a magnetic moment and an angular momentum, they will align with, and precess about an external magnetic field. When perturbed by a second, weaker alternating magnetic field at the same frequency as the proton precession, known as the Larmor frequency, the protons will also begin to precess around this new field. When this second field is applied at 90 degrees to the primary field, the protons will tilt away from their alignment with the static field. An NMR experiment measures the restoration of the proton magnetization in the direction of the static field, upon removal of the alternating field.

The exponential build-up of magnetization as a function of time, t, is characterized by a relaxation time constant known as T_1 and is described by the equation:

$$M(t) = m\left[1 - 2\exp\left(\frac{-t}{T_1}\right)\right] \tag{1.1}$$

where m is proportional to the number of protons relaxing with the time constant T_1.

Bulk water has a relaxation time referred to as T_{1B}. When water exists in a pore, T_1 will depend on T_{1B}, the surface area to volume ratio of the pore, S/V, and the ability of the pore surface to assist in the relaxation. The equation that describes the controls on NMR T_1 relaxation of water in a porous medium is:

$$\frac{1}{T_1} = \frac{1}{T_{1B}} + \rho_1 \frac{S}{V} \tag{1.2}$$

where ρ_1 is the surface relaxivity, which quantifies the extent to which the relaxation rate is enhanced due to the presence of the solid surface (Brownstein and Tarr, 1979). The surface relaxivity depends primarily upon the number of unpaired electrons on the grain surfaces. In rocks, paramagnetic ions are common substances with unpaired electrons. Paramagnetic ions may exist sorbed to the surface of non-magnetic grains, or exposed on the surface of magnetic minerals (Krauskoph and Bird, 1995).

Equation 1.2 is valid only when the relaxation rate is limited by proton relaxation at the surface of the pore, which is the case when the following inequality is satisfied:

$$\frac{\rho_1 R}{D_o} \ll 1 \tag{1.3}$$

where R is the pore radius and D_o is the diffusion coefficient of bulk water. Under these conditions protons are continually moving to and from the surface, as a result of Brownian motion, and the magnetization within the pore remains uniform (Kenyon, 1997). The alternate situation is if the relaxation were limited by the diffusion of the protons to the pore surface, in which case NMR measurements could not be used to gain information about the pore structure. This diffusion regime may be observed in rocks with very large pores or when the surface relaxivity is very large. Kleinberg et al. (1994)

however, state that the vast majority of naturally occurring rocks obey equation 1.2 and relaxation is surface limited.

Many geological materials have a distribution of pore sizes, corresponding to a distribution of S/V values and as a result a distribution of T_1 time constants are measured by NMR relaxation. The relationship that describes the magnetization of the protons existing in numerous multi-sized pores is:

$$M(t) = \sum_i m_i \left[1 - 2\exp\left(\frac{-t}{T_{1i}} \right) \right] \tag{1.4}$$

where m_i is proportional to the number of protons relaxing with the time constant T_{1i}. Equation 1.2 is used to obtain an S/V from each T_1 value.

A second NMR relaxation time constant called T_2, characterizes the decay of the magnetization in the plane perpendicular to the static field. T_2 relaxation depends on the surface relaxivity, ρ_2, which is different from T_1 surface relaxivity and also depends on the surface area to volume ratio of the pore space and the bulk relaxation of the water. In addition, T_2 depends on the diffusion of water protons through internal magnetic field inhomogeneities resulting to a great extent from magnetic susceptibility differences between the pore fluid and the solid grain. The relaxation of the protons due to this diffusion, T_D, is defined by:

$$\frac{1}{T_D} = \frac{D_{eff} \gamma^2 G^2 t_e^2}{12} \tag{1.5}$$

where D_{eff} is the effective diffusion coefficient of the water in the pore space and γ is the gyromagnetic ratio of the proton, which is a constant. The parameter t_e is the echo time, a refocusing interval necessary for T_2 measurements. T_2 relaxation measurements are

usually made at several echo times. G is the internal magnetic field gradient experienced by the protons due to magnetic field inhomogeneities (Kenyon, 1997). It should be noted that diffusion due to Brownian motion does not cause enhanced T_2 relaxation of the protons (Kleinberg and Vinegar, 1996).

The gradient present outside a sphere of radius R_g is given by the following expression:

$$G = \frac{\mu_o H_o \Delta k}{4R_g} \tag{1.6}$$

where Δk is difference in magnetic susceptibility between the grain and the surrounding medium, H_o is the external magnetic field and μ_o is the permeability of free space (Glasel and Lee, 1974). In porous media however, the magnetic field inhomogeneities cannot be described as a simple gradient. Hurlimann (1998) proposed the field inhomogeneities could be represented by an effective gradient, defined as the average of the field inhomogeneities over the protons' dephasing length, which is the distance traversed by the proton during the relaxation process. The maximum effective gradient, G_{max}, for a given susceptibility difference in a pore space is given as:

$$G_{\max} = \frac{\Delta k\, B_o}{l} \tag{1.7}$$

where B_o is the magnetic field strength and l is a length scale that is characteristic of the magnetic susceptibility difference and depends on the pore size. The field strength and the magnetic susceptibility difference can vary significantly depending on the experiment and the sample under investigation. As a result, G can be quite variable and it is a difficult parameter to estimate.

The magnetic field gradients cause small random variations in the Larmor frequencies of each of the protons, causing them to relax more rapidly than they would if solely under the influence of surface and bulk processes. It has been shown that T_2 relaxation due to diffusion and surface effects are independent (Robertson, 1966) and therefore the processes can be summed to form the governing equation for T_2 relaxation:

$$\frac{1}{T_2} = \frac{1}{T_{2B}} + \rho_2 \frac{S}{V} + \frac{D_{eff}\gamma^2 G^2 t_e^2}{12} \tag{1.8}$$

When measurements are made on weakly magnetic rocks at low magnetic field strengths and short echo times, the diffusion term shown in equation 1.8 is very small and can be neglected (Kleinberg and Horsfield, 1990). Under these circumstances T_2 data can be interpreted using an equation analogous to that for T_1:

$$\frac{1}{T_2} = \frac{1}{T_{2B}} + \rho_2 \frac{S}{V} \tag{1.9}$$

However, even under these conditions, the measured T_1 and T_2 in a porous sample are not usually the same. This is a result of a greater probability of the surface aiding in T_2 relaxation than T_1 relaxation. Consequently, ρ_2 is greater than ρ_1. Kleinberg et al. (1993) reported a relationship of $T_1=1.5T_2$ for 48 sandstones at a Larmor frequency of 2 MHz. When internal gradients are significant, the relationship between T_1 and T_2 will depend on the magnetic content as shown by Foley et al. (1996).

In summary, T_2 data for rocks with low magnetic content that are measured at small magnetic field strengths and short echo times, which is the case for many sandstones, can be interpreted using equation 1.9 as Kleinberg et al. (1993) demonstrated. Equation 1.8 is required for materials with significant internal gradients, such as iron rich rocks, or a sample with some magnetic component measured at a large field strength.

One of the principle uses of NMR data in the petroleum industry is to obtain an estimate of permeability from the S/V values. The primary objective of this thesis is to extend this application to near surface problems where the rocks and sediments may have higher concentrations of magnetic material. In the past, using NMR for environmental problems was limited, as a method of remotely determining the surface relaxivity does not exist. Interpreters of NMR data commonly assign a constant value to this parameter, but this is an invalid assumption for near surface materials, considering the large variation in concentration of magnetic materials possible for these rocks and sediments. In order for NMR to be used for the accurate determination of S/V in a wide range of geological settings, a procedure is required for the analysis of T_1 and T_2 data that can properly account for varying magnetic content.

Two approaches are investigated in this thesis as potential methods of achieving this objective. The first, which is the focus of Chapter 2, is the use of magnetic susceptibility, a parameter highly dependent on the weight percent of magnetic material, to estimate the surface relaxivity of sediment samples. Relationships between surface relaxivity, ρ_1, calculated from high magnetic field T_1 measurements using equation 1.2, and magnetic susceptibility are investigated for two magnetic minerals. This procedure is valid for T_1 data and T_2 data for materials with small magnetic fractions measured at low magnetic field strengths and short echo times.

Chapter 3 investigates the use of high field T_2 measurements in which the diffusion term is important. Since T_2 is measured at several echo times, several data are obtained for a single sample. A parametric inversion is used in an attempt to obtain the three unknown parameters, S/V, ρ_2 and G. This may allow the independent

determination of the S/V and the surface relaxivity. This procedure is valid for T_2 measurements at high fields and T_2 measurements at low fields in which the internal gradients are significant.

2 - THE USE OF MAGNETIC SUSCEPTIBILITY MEASUREMENTS IN THE INTERPRETATION OF NMR DATA

2.1 - INTRODUCTION

The distribution of surface area to volume ratio in the pore space of a sedimentary material can be obtained from NMR measurements. What is required, however, is a value for the surface relaxivity. This is commonly accomplished by measuring T_1, T_{1B}, the surface area and the porosity of a representative set of samples. The surface area to volume ratio is then calculated and ρ_1 is determined from equation 1.2. This surface relaxivity could subsequently be used to calculate the S/V distributions in samples for which only T_1 or T_2 data are collected, such as borehole data. While this method has yielded reliable results (Kenyon and Kolleeny, 1995 and Borgia et al., 1996), it is labour intensive, requiring time-consuming laboratory measurements. Many core samples would require laboratory NMR analysis and surface area measurements to ensure the variation in surface relaxivity along the entire length of the borehole is captured.

Several studies have shown that the surface relaxivity of sedimentary samples correlates well with the amount of magnetic material measured by chemical analyses. Some experiments have related surface relaxivity to the concentration of paramagnetic ions sorbed to the surface of non-magnetic grains (Kenyon and Kolleeny, 1995 and Bryar et al., 2000). Foley et al. (1996) created calcium silicate sand with a known paramagnetic ion concentration distributed evenly through the grains and correlated that concentration with surface relaxivity. Dodge et al. (1995) found that the calculated surface relaxivity

and the total weight percent of iron in several sandstones also correlated well. In addition, Bryar et al. (2000) found that the surface relaxivity and the total amount of iron bearing pseudobrookite were related. Since surface relaxivity is dependent on the surface concentration of magnetic material, comparing it to the total weight percent of magnetic material is questionable. However, when the surface concentration and weight percent of magnetic materials are proportional, such as when the magnetic material exists as distinct grains of uniform size, the weight percent can be used to estimate surface relaxivity.

Using bulk chemical analyses to estimate ρ_1 would be time consuming. In addition, the same problem arises as for measuring the surface area to calculate the surface relaxivity. When using a borehole NMR instrument, core samples at regular intervals would have to be obtained and tested to accurately map the change in magnetic content throughout the section. An alternate method of determining the total magnetic fraction of a rock sample is to measure magnetic susceptibility. This measurement can be made with a borehole instrument, thus avoiding the need for core samples.

Magnetic susceptibility is a property of materials that is defined by:

$$\mathbf{M} = k\mathbf{H} \tag{2.1}$$

where **M** is the magnetic dipole moment per unit volume, **H** is the magnetic field and k is the magnetic susceptibility. This relationship holds for linear media such as paramagnetic materials, where any alignment of magnetic moments is exclusively a result of the presence of an external magnetic field. Ferromagnetic materials are non-linear and are capable of holding remanence and consequently this simple relationship for magnetic susceptibility is invalid. However, at very low field strengths (<1mT), equation 2.1 is an appropriate approximation for all mineral types (Collinson, 1983).

Similar to ρ_1, magnetic susceptibility is also heavily dependent on the magnetic content of a rock sample. For example, McNeill et al. (1996) presented a graph that compiled measurements made in several studies, which shows that magnetic susceptibility is strongly dependent on volume percent of magnetite. Also, Collinson (1983) showed that for many paramagnetic minerals, the magnetic susceptibility could be calculated based on the quantity and characteristics of the ions present by using the following equation:

$$k = \frac{\mu_B^2}{3RT}\left[xP_B^2(Fe(II)) + yP_B^2(Fe(III)) + zP_B^2(Mn(II))\right] \tag{2.2}$$

where μ_B denotes the Bohr magneton moment, which is the smallest element of the magnetic moment of the orbital moment of an electron and is equal to 9.3×10^{-24} J/T. R is the gas constant, T is the temperature, x, y and z are the gram ion numbers of each ion, and P_B is the effective Bohr magneton number for each ion, which are approximately 5.25-5.53 for Fe(II) and 5.58 for Fe(III) and Mn(II) (Nagata, 1961). The three ions, Fe(II), Fe(III) and Mn(II) are the most commonly occurring paramagnetic ions composing near surface rocks and sediments (Krauskoph and Bird, 1995).

Clark (1997) argued that the state and quantity of iron (and presumably manganese) primarily controls the overall magnitude of the magnetic susceptibility for most rocks. As long as each mineral is present in quantities less than 10 percent by volume, the magnetic susceptibility can be estimated as:

$$k_{total} = \sum \theta_i k_i \tag{2.3}$$

where θ_i is the volume percent of the i^{th} mineral in the material and k_i is the magnetic susceptibility of the i^{th} mineral. In other words, while in small quantities, the magnetic

susceptibility of every iron and manganese-bearing mineral is proportional to its volume percent. For a detailed treatment of the theory and measurement of magnetic susceptibility please see Appendix B.

Given that both surface relaxivity and magnetic susceptibility are related to the magnetic content of a rock sample, the question addressed in this chapter is: Can magnetic susceptibility be used to estimate the surface relaxivity of rocks and sediments? Since borehole instruments can measure both NMR relaxation and magnetic susceptibility, application of this method would allow the determination of the surface relaxivity without core analysis thereby facilitating entirely remote S/V and permeability estimates.

2.2 - BACKGROUND

The following section assesses the present status of NMR relaxation research. In doing so, the manner in which surface relaxivity varies with magnetic content is investigated and gaps in our current understanding are identified. Also, the benefits of using magnetic susceptibility to estimate magnetic content over chemical analyses are demonstrated.

Much is known about the dependence of surface relaxivity on magnetic content. Nevertheless, there are some discrepancies in the literature and disparity in our understanding. The first step in unraveling the relationship between surface relaxivity and magnetic content is to determine the value of the surface relaxivity in materials with no magnetic component. If surface relaxivity depends exclusively on the presence of

paramagnetic ions, or more specifically ions with unpaired electrons, then diamagnetic materials with only paired electrons, should have surface relaxivities close to zero. There are however, inconsistencies in the literature regarding the value of the surface relaxivity of these substances. Foley et al. (1996) calculated the theoretical value of ρ_1 that could result from intermolecular and intramolecular dipole coupling, which would be the strongest relaxing process in the absence of paramagnetic effects, to be 0.6 μm/s at a Larmor frequency of 2 MHz and 0.1 μm/s at 10 MHz. Bryar et al. (2000) measured the surface relaxivity of pure porous silica and found very low values for ρ_1 of 1.2×10^{-3} μm/s at 90 MHz. They ensured no paramagnetic impurities existed on the surface of the grains by cleaning the material upon acquisition from the manufacturer. The results of Bryar et al. (2000) are believed to be consistent with the theoretical values of Foley et al. (1996).

Foley et al. (1996) reported significantly higher values of ρ_1 for non-magnetic materials. They manufactured pseudowollstanite with known concentrations of Fe(III) and although they did not measure pure $CaSiO_3$, the extrapolated value of surface relaxivity at zero Fe(III) was 4 μm/s. They attributed this remarkably high value of surface relaxivity to crystal defects caused by the manner in which the samples were created. These defects resulted in unpaired electron spins in the grains, making some of the surface paramagnetic as opposed to diamagnetic, thereby enhancing the surface relaxivity. The study did not report if any chemical analyses were completed on the original calcium silicate.

Hinedi et al. (1997) reported contradictory T_1 surface relaxivities. They measured T_1 at 2.0×10^{2} MHz on porous silica materials and calculated surface relaxivities of 4.4×10^{-3} μm/s to 7.7×10^{-3} μm/s, but for silica sand they calculated higher ρ_1 values of

around 3 μm/s. They also did not clean the minerals once received from the manufacturer, nor did they undertake any chemical analyses.

In reviewing the studies of Foley et al. (1996) and Hinedi et al. (1997) it is not possible to eliminate unobserved magnetic contamination as the cause of the elevated values for the surface relaxivity they both measured. The crystal defects discussed by Foley et al. (1996) may have also contributed to the relaxation, but it is assumed they would also influence the magnetic susceptibility in much the same way as iron or manganese. The surface relaxivity for non-magnetic substances in the absence of these crystal defects is likely very close to zero, as was reported by Bryar et al. (2000) and observed by Hinedi et al. (1997) for their silica materials.

Several studies have investigated the variation of surface relaxivity in rocks, sediments and laboratory-engineered samples. As an initial reference, ρ_1 values calculated using surface areas measured by N_2 adsorption have been reported as low as 1×10^{-3} μm/s (Bryar et al., 2000) and as high as 24 μm/s (Kenyon and Kolleeny, 1995). Values for ρ_1 typically range from 1 μm/s to 11 μm/s (Borgia et al., 1996, Foley et al., 1996 and Hinedi et al., 1997). Low field T_2 surface relaxivities of natural and synthetic rocks have been reported between 1 μm/s and 27 μm/s (Dodge et al., 1995 and Foley et al., 1996).

There is some disagreement in the literature on the range of surface relaxivity values in magnetic rocks. Understanding how ρ_1 varies with the quantity of magnetic material is essential in determining its relationship with magnetic susceptibility. Studies that calculated surface relaxivity for several naturally occurring sandstone samples found different ranges for surface relaxivity. For example, Dodge et al. (1996) reported a four-

fold increase in ρ_1 for several samples while Roberts et al. (1995) observed a 13-fold increase for the rocks they measured.

Many researchers in the oil industry do not explicitly calculate surface relaxivity, but rather assign a cut-off value to the T_2 distribution that distinguishes water in pores that cannot be removed by centrifuging at a given speed. The oil industry also tends to work with T_2 rather than T_1, so we will think in terms of T_2 for a moment. These cut-offs vary depending on the amount of magnetic material in the sample. If it is assumed that that T_2 can be represented by equation 1.9, then a change in the cut-off value is inversely proportional to surface relaxivity. Researchers have used cut-offs as low as 3 ms (Rueslatten et al., 1998) for sedimentary rocks with high concentrations of the magnetic minerals glauconite and chlorite and as high as 92 ms for carbonates, which likely contain very little magnetic material (Chang et al., 1997). Both of these studies measured T_2 at 2 MHz and short echo times (0.4 ms). If equation 1.9 holds, a 30-fold variation in ρ_2 is possible for naturally occurring rock types. However, relaxation due to diffusion in internal gradients is likely significant in the more iron rich rocks, requiring equation 1.8 to be used for analysis. Consequently, the range of surface relaxivities is probably not quite this large.

Despite the number of T_1 surface relaxivity measurements that have been made, we still lack a good understanding of how the presence of magnetic materials affects this parameter. There do not appear to be any studies that systematically varied the quantity of magnetic minerals or materials to assess the bounds on the surface relaxivity.

In addition to the amount of magnetic material, surface relaxivity may be influenced by the occurrence of the magnetic material, in particular, the mineral type.

Bryar et al. (2000) compared the T_1 surface relaxivities of pseudobrookite, Fe_2TiO_5 and oxyhydroxide coatings, FeOOH. They found that pseudobrookite at a surface concentration of 2.3×10^{-9} mol Fe/m^2 had a surface relaxivity of 1.5×10^{-2} μm/s. The oxyhydroxide coatings at similar concentrations had surface relaxivities of 1.0×10^{-3} μm/s to 1.2×10^{-2} μm/s. The pseudobrookite appeared to be a more effective proton-relaxing agent than the oxyhydroxide coating, but there was a large amount of error associated with the oxyhydroxide coating measurements.

Conversely, Dodge et al. (1995) conducted experiments on sandstones with high concentrations of iron rich glauconite, chlorite and pyrite and their results suggested that for these minerals, the surface relaxivity was not dependent on the way in which the iron was incorporated into the crystal lattice. In other words, only the total amount of bulk iron present affected the surface relaxivity, not the mineralogy.

Chitale et al. (1999) showed a relationship between low field T_2 times and the specific clay mineralogy, but attributed this to differences in grain size and corresponding pore size, rather than to differences in surface relaxivity. They found that very short T_2 times (1 ms to 3 ms) were associated with the occurrence of illite, while 5 ms to 50 ms T_2 times correlated with kaolinite and chlorite. They did not discuss mineralogical controls on the surface relaxivity.

An additional challenge in determining the effect of magnetic materials on the surface relaxivity is the confusion in how the quantity of magnetic material is measured. Very different surface relaxivity values for what appears to be the same amount of magnetic material were reported in different studies. This is illustrated by comparing the Foley et al. (1996) and Kenyon and Kolleeny (1995) studies. Foley et al. (1996)

calculated a surface relaxivity of 2.6 μm/s for a surface concentration of Mn(II) of 3.8×10^{-5} mol Mn(II)/m^2 measured at 2 MHz, while Kenyon and Kolleeny (1995) measured a surface relaxivity of 24 μm/s for the same surface concentration, measured at 10 MHz. Also, Foley et al. (1996) measured a ρ_1 of 11 μm/s for a surface concentration of Fe(III) of 1.0×10^{-4} mol Fe(III)/m^2, while Kenyon and Kolleeny (1995) reported a value of 30 μm/s for the same amount of Fe(III). Both of these studies measured the amount of magnetic material through chemical analyses.

Although both experiments were well controlled, the discrepancies could be due to magnetic impurities. This illustrates how relating surface relaxivity to magnetic susceptibility rather than to the measured bulk magnetic content may be more reliable due to the uncertainty of chemical analyses. Foley et al. (1996) did measure the magnetic susceptibility, which verified that no magnetic impurities existed, while Kenyon and Kolleeny (1995), who measured the larger values of surface relaxivity, did not. Magnetic susceptibility also has the added advantage of being a remote measurement of magnetic content and does not require core samples to be brought to the surface and analyzed.

In summary, previous studies in NMR relaxation suggest that the development of a relationship between magnetic susceptibility and surface relaxivity is feasible. The value of surface relaxivity in materials with no magnetic content is likely close to zero, but the manner in which the surface relaxivity increases with increasing magnetic content requires systematic study. Also, the effect of minerals with different magnetic properties requires investigation to allow robust relationships to be developed. Finally, previous studies suggest that magnetic susceptibility could prove to be a more reliable method of

determining magnetic content than chemical analyses as the latter can have a large error associated with the measurement.

2.3 - SELECTION OF SAMPLES FOR STUDY

The focus of this research is the environmental application of NMR relaxation measurements, which most commonly deals with sedimentary rocks, unconsolidated sediments and soils. In addition, I wanted to assess the effect of iron-bearing minerals in varying quantities and with different magnetic properties on the NMR relaxation time. The minerals chosen for this study were quartz, hematite and magnetite.

2.3.1 - Quartz

Quartz (SiO_2) was chosen as the mineral with which the magnetic minerals were to be mixed. It is an extremely common mineral in sediments especially sandstones due to its resistance to weathering (Nesse, 1991 and Deer et al., 1992) and it can compose over 80% of some rocks (Raymond, 1995). Quartz is diamagnetic with an approximate mass susceptibility of -6.0×10^{-9} m^3/kg (Carmichael, 1989). Susceptibility is often reported as a dimensionless quantity and the mass susceptibility is this dimensionless constant divided by the density. The small susceptibility of quartz made it ideal to combine with the magnetic minerals, as it would not contribute significantly to the magnetic response.

2.3.2 - Hematite

Hematite (Fe_2O_3) was an obvious choice as it is a common iron-bearing mineral under oxidizing conditions. The abundance of hematite in soils and near surface sediments can vary widely, but is usually present in concentrations less than 10 percent by weight (Stucki et al., 1985 and Scollar et al., 1990). Hematite in sediments and sedimentary rocks commonly results from the oxidation of the surface of an iron-bearing mineral to hematite (Deer et al., 1992 and Krauskopf and Bird, 1995). It is also often found as a cementing medium in sandstones (Deer et al., 1992) and can form metasomatically from solution, with the iron having been derived from overlying sediments (Deer et al., 1992). In addition, bacteria catalyzed precipitation reactions, which use dissolved Fe(II) from aerated groundwater, can create hematite (Krauskopf and Bird, 1995). Hematite occurring as finely disseminated grains in clastic sedimentary rocks (Nesse, 1991) is also common and finally, when Fe(III) precipitation reactions are favorable, hematite colloids, which are small particles, may be formed that can be easily transported in surface waters (Krauskopf and Bird, 1995). Many of these occurrences can be modeled as distinct grains.

Hematite is antiferromagnetic and has mass susceptibilities between 1.0×10^{-7} m^3/kg to 6.0×10^{-6} m^3/kg, with an average value of 1.3×10^{-6} m^3/kg. This is on the same order of magnitude as most paramagnetic minerals (Carmichael, 1989).

2.3.3 - Magnetite

Magnetite (Fe_3O_4) is one of the most abundant oxide minerals and is found in a large number of sedimentary rocks (Thompson and Oldfield, 1986). The main occurrence of magnetite in sediments and sedimentary rocks is as a heavy detrital

mineral, which can also be modeled as distinct grains. In addition, bacteria can cause the formation of magnetite (Deer et al., 1992 and Nesse, 1991). In sediments and soils, magnetite abundances are usually less than 2 percent by weight, but depend heavily on the parent material, which is the rock from which the soil or sediment was derived (Nabighian, 1987). Magnetite is ferrimagnetic with an average mass susceptibility of 1.2×10^{-3} m^3/kg (Carmichael, 1989). It was chosen for this study largely due to its magnetic properties, as when this mineral is present in sediments it dominates the magnetic response. Understanding its effect on the surface relaxivity is essential in creating valid relationships with magnetic susceptibility.

2.4 - MATERIALS AND METHODS

2.4.1 - Minerals

The quartz was received crushed from Alfa Aesar and was 99.995% SiO_2. The grain diameter was reported as 4.0×10^2 μm, but smaller grain sizes were likely present as well. The hematite was received from the Pacific Mineral Museum and originated from a deposit in Coutlee, British Columbia, Canada. The magnetite was also received from the Pacific Mineral Museum and originated from a deposit in Texada, Gilles Bay, British Columbia, Canada.

2.4.2 - Description of Sample Preparation and Characterization

The quartz was tumbled for 24 hours in a 10% solution of hydrochloric acid to remove metal impurities. The acid was then decanted and the material was rinsed and tumbled with distilled, de-ionized water for two to three hours. This cycle was repeated

until the pH of the water was approximately 6 and remained unchanged for several cycles. This was assumed to be pure water in equilibrium with the air. The quartz was then transferred into beakers and placed in an oven to dry for 24 hours.

The magnetite was enclosed in plastic bags and paper towel and broken into cubic centimetre sized pieces using a rock hammer. A stainless steel rock grinder further reduced the material in size. The magnetite was then sieved for 30 minutes in copper sieves that isolated grains that were 1.4×10^2 mesh to 45 mesh, which corresponds to grain diameters of 1.1×10^2 μm and 3.6×10^2 μm and then stored in plastic containers.

The hematite was also manually broken into small chunks and ground by the stainless steel rock grinder. It was then sieved for 30 minutes in stainless steel sieves that separated grains between 1.5×10^2 mesh and 48 mesh, which corresponds to grain diameters of 1.0×10^2 μm to 3.3×10^2 μm. The material was then stored in plastic containers.

The densities of the hematite and magnetite were measured on a Micromeritics Multivolume helium pycnometer. The magnetite had a density of 5.12 g/cm^3 with an error of 0.43 g/cm^3, which was determined by measuring replicates. The literature value of the density of magnetite is 5.20 g/cm^3 (Carmichael, 1989). The density of the hematite was measured as 3.60 g/cm^3 with an error of 0.29 g/cm^3 and the literature value for hematite is 5.28 g/cm^3 (Carmichael, 1989). Discrepancies between the hematite density reported in the literature and the measured value prompted a whole rock analysis of the hematite by X-ray fluorescence (ALS Chemex, North Vancouver, BC, Canada). This procedure found that the mineral was in fact 59% Fe_2O_3 and 39% SiO_2. The remaining fraction consisted of various other metals. For clarity, the mineral composed of 59%

Fe_2O_3 will be referred to as sample hematite as to not confuse it with pure Fe_2O_3, which will simply be called hematite. The density of quartz is 2.65 g/cm^3 (Carmichael, 1989). The density (D) of each mineral mixture was calculated by:

$$D_{mixture} = \phi_{magnetite} D_{magnetite} + \phi_{sample\,hematite} D_{sample\,hematite} + \phi_{quartz} D_{quartz} \tag{2.4}$$

where ϕ is the fraction of the indicated mineral in the mixture. The error for the densities as well as all other calculated values, were determined using Gauss' equation for the propagation of random error, which assumes the errors are uncorrelated:

$$\varepsilon(f) = \sqrt{\left(\left(\frac{\partial f}{\partial x_1}\right)^2 (\varepsilon(x_1))^2 + \left(\frac{\partial f}{\partial x_2}\right)^2 (\varepsilon(x_2))^2 + \ldots + \left(\frac{\partial f}{\partial x_n}\right)^2 (\varepsilon(x_n))^2\right)} \tag{2.5}$$

where f is the function for which the error is being calculated, and $\varepsilon(x_n)$ is the error of the n^{th} variable x_n, of the function.

For the simple mathematical operations of addition and subtraction and also multiplication and division, equation 2.5 can be simplified to:

$$\varepsilon(x_1 - x_2) = \varepsilon(x_1 + x_2) = \sqrt{(\varepsilon(x_1))^2 + (\varepsilon(x_2))^2} \tag{2.6}$$

and

$$\frac{\varepsilon(x_1 x_2)}{x_1 x_2} = \frac{\varepsilon(x_1 / x_2)}{x_1 / x_2} = \sqrt{\left(\frac{\varepsilon(x_1)}{x_1}\right)^2 + \left(\frac{\varepsilon(x_2)}{x_2}\right)^2} \tag{2.7}$$

Surface area measurements of the quartz, hematite and magnetite were made using the Brunauer-Emmett-Teller (BET) N_2 adsorption method. Two samples of hematite, magnetite and quartz were measured and the average value was taken as the surface area of the mineral. The error in the surface area should reflect the measurement error and also the deviation of the two measurements from the average. The surface areas

of the pure hematite were 0.40 m^2/g and 0.57 m^2/g, which yielded an average surface area of 0.48 m^2/g. An error of 8.9×10^{-2} m^2/g, which is the difference between the average value and the two measured values, was assigned. The surface areas of the magnetite were 6.2×10^{-2} m^2/g and 7.7×10^{-2} m^2/g, with an average of 6.9×10^{-2} m^2/g, which differs from the measured values by approximately 10%. The surface areas measured for pure quartz were very similar for the two replicates and the average was 0.14 m^2/g and an error of 1% was assigned.

The total surface area (S) for each mineral mixture was calculated by:

$$S_{mixture} = \phi_{magnetite} S_{magnetite} + \phi_{sample\,hematite} S_{sample\,hematite} + \phi_{quartz} S_{quartz} \qquad (2.8)$$

and the error was determined for each surface area using equations 2.6 and 2.7.

Teflon containers, or cells, with volumes averaging 0.63 cm^3 were manufactured to contain the sediment samples for measurements. The containers were washed in toluene to remove any oils and then boiled in 10% hydrochloric acid solution to remove any metals from the surface of the cell.

Sample hematite and quartz mixtures were prepared in concentrations of 0, 3.5, 5, 10, 15, 20, 50 and 100 percent sample hematite by weight. Since the mineral believed to be hematite was actually a combination of hematite and SiO_2, the actual weight percents of the samples with respect to pure hematite were 0, 2.1, 3, 6, 9, 12, 30 and 60 percent hematite by weight. Magnetite and quartz samples were made in concentrations of 0.5, 1 and 2 percent by weight of magnetite

Sub-sets of each mixture were then tightly packed into the teflon cells and sealed with a permeable paper lining to inhibit grain movement through the perforated cell lid. Three sub-samples for the 2.1, 3, 6, 9 and 12 percent hematite mixtures were made, while

one sub-sample for the 0, 30 and 60 percent hematite samples were created. Two sub-samples were made for each weight percent of magnetite. The mass of each sample was measured in grams to the fourth decimal place. The maximum error of the balance was 1.0×10^{-3} g and this error was assigned to each mass. As a result of the sampling, there was also error in the mineral concentrations of each sub-sample and the stated weight percents of each mixture should be considered a guideline rather than the precise value. This error was difficult to quantify. It is possible that the samples with very small amounts of the magnetic mineral may have very large sampling errors, perhaps 100%, while the mixtures with larger magnetic fractions may have mixing errors closer to 5% or 10%. Fortunately, even large sampling errors for the lower weight percent mixtures will not significantly affect the density, surface area or porosity calculations, as the quartz primarily dominates these properties in these samples. An error of 10% was assigned to each weight percent. For discussion, when referring to the magnetic mineral content of the sub-samples, the terms approximate or intended weight percents will be used.

The porosity of each sample was calculated from the volume of the sample container, V_{cell}, and the volume of the solid grains, $V_{solid\ grains}$, using:

$$Porosity = \frac{V_{cell} - V_{solid\ grains}}{V_{cell}} \tag{2.9}$$

Table 2.1 and 2.2 summarize the physical properties for each of the mineral mixtures created, along with the error associated with each parameter. The hematite values are reported in weight percents corresponding to the pure hematite concentration rather than the sample hematite concentration. In table 2.1, only one replicate for each weight percent sub-sample is shown, as the calculated values are the same for each. In reality, the values for each replicate are expected to vary slightly due to the uncertainty in

the mixing procedure. Table 2.2 shows the masses and porosities specific to each sub-sample. The porosities are large, but within the typical range for unconsolidated sediments (Domenico and Schwartz, 1998).

In preparation for NMR and magnetic susceptibility measurements, the sediment samples were saturated with distilled, de-ionized (17 Mega-Ohm cm) water, which was de-gassed by boiling. A vacuum was created around the samples and the water was introduced and pressurized. The samples remained in this environment for 12 to 24 hours to ensure full saturation.

Sample Description: Weight Percent of Mineral Shown	Density of Mixture **Value** (g/cm^3)	Density of Mixture **Error** (g/cm^3)	Surface Area of Mixture **Value** (m^2/g)	Surface Area of Mixture **Error** (m^2/g)
100% Quartz	2.65	0.0200	0.140	0.0014
2.1% Hematite	2.68	0.256	0.152	0.0192
3% Hematite	2.70	0.253	0.158	0.0190
6% Hematite	2.74	0.243	0.174	0.0185
9% Hematite	2.79	0.236	0.191	0.0184
12% Hematite	2.83	0.231	0.208	0.0186
30% Hematite	3.11	0.265	0.310	0.0263
60% Hematite	3.57	0.290	0.483	0.00890
0.5% Magnetite	2.66	0.132	0.139	0.0155
1% Magnetite	2.67	0.131	0.138	0.0154
2% Magnetite	2.70	0.130	0.137	0.0152

Table 2.1 – Density and surface area of the mineral mixtures.

Sample Description: Weight Percent of Mineral Shown	Mass of Mixture **Value** (g)	Porosity of Mixture **Value**	Porosity of Mixture **Error**
100% Quartz	0.706	0.50	0.048
2.1% Hematite	0.729	0.53	0.048
3% Hematite	0.736	0.53	0.048
6% Hematite	0.714	0.54	0.048
9% Hematite	0.757	0.53	0.049
12% Hematite	0.750	0.54	0.048
2.1% Hematite	0.734	0.53	0.049
3% Hematite	0.749	0.52	0.049
6% Hematite	0.745	0.52	0.048
9% Hematite	0.745	0.53	0.048
12% Hematite	0.785	0.53	0.049
2.1% Hematite	0.790	0.53	0.050
3% Hematite	0.814	0.52	0.050
6% Hematite	0.812	0.52	0.050
9% Hematite	0.822	0.52	0.050
12% Hematite	0.844	0.52	0.050
30% Hematite	0.754	0.53	0.047
60% Hematite	0.798	0.57	0.046
0.5% Magnetite	0.823	0.51	0.051
1% Magnetite	0.783	0.53	0.050
2% Magnetite	0.816	0.51	0.050
0.5% Magnetite	0.801	0.52	0.050
1% Magnetite	0.803	0.52	0.050
2% Magnetite	0.823	0.51	0.050

Table 2.2 – Mass and porosities of the mineral mixtures. The error for each mass is 0.00141 g calculated using Gauss' equations.

2.4.3 - Nuclear Magnetic Resonance T_1 and Magnetic Susceptibility Measurements

Nuclear magnetic resonance T_1 measurements were made using a Bruker NMR Spectrometer operating at a magnetic field strength of 2.2 T, in which the Larmor frequency of protons is 90 MHz. A modified inversion-recovery pulse sequence was used to collect the relaxation data, which has the advantage of being less sensitive to imperfections in the 180° pulse. There was a dead time of 10 μs at the beginning of the relaxation process in which no data were collected. The T_1 of each mineral sample was

measured, then the pore fluid was separated from the solid grains by centrifuging and the T_1 of the bulk fluid was measured.

The multi-exponential relaxation data were inverted to obtain T_1 distributions using a regularized non-negative least squares algorithm similar to that provided in the commercial package WinDXP (Universal Systems, OH). This routine fits the data by 1.6×10^2 exponentially spaced T_1 values from 1 ms to 10 s. The small number of T_1 values keeps the processing time to a minimum. The logmean of the resulting distribution was used for surface relaxivity calculations and the error was determined by comparing the inversion results with a second, least distance inversion. For monomodal distributions, the logmean is approximately equal to the T_1 value obtained from a fit to a single-exponential decay if the distribution is sufficiently narrow. Most other averaging methods would also be adequate for these data.

The T_{1B} data was fit to a single exponential decay curve, as free water would be expected to decay exponentially with a single time constant. The error associated with this fit was assigned as the error on T_{1B}. A more detailed treatment of these inversion procedures is given in the Materials and Methods section of Chapter 3.

The surface area to volume ratio was calculated using the following relationship:

$$\frac{S}{V} = \frac{(Sample\ Density)(Surface\ Area)(1 - Porosity)}{Porosity} \tag{2.10}$$

These S/V values may not represent the mixing of the different sized grains of hematite and quartz and could be slightly smaller than is realistic. The T_1 data and the S/V were then used to calculate the surface relaxivity for each sample using equation 1.2.

Magnetic susceptibility measurements were completed on the same samples as those used for NMR measurements. A Quantum Design Superconducting Quantum

Interference Device (SQUID) magnetometer was used that measures the total magnetic moment in the direction of a static applied magnetic field. Values were reported in emu and were converted to SI by dividing by the mass and applying a conversion factor of $4\pi\times10^{-3}$ to obtain the mass susceptibility in m^3/kg. Magnetic susceptibility will be discussed in terms of the mass susceptibility. Susceptibility was measured on the magnetite at magnetic field strengths ranging from 5×10^{-5} T to 1×10^{-4} T and on the hematite at field strengths of 2×10^{-4} T to 1×10^{-3} T. Borehole instruments use field strengths of approximately 1.5×10^{-3} T. This value is for the centre of the loop generating the magnetic field and the field may be slightly smaller in the borehole and the rock. At all field strengths used in this study, any domain wall movement can be considered reversible and the susceptibility independent of the field strength (Collinson, 1983).

The susceptibility of each sample was measured five times, the average was taken and the standard deviation was recorded as the error. A teflon rod was used to suspend the samples in the SQUID. The containers and the rod were washed with ethanol prior to each measurement to remove any impurities. The signal resulting from the sample suspension apparatus, which was weakly diamagnetic, was subtracted out for the analysis. Appendix B outlines the various terminology used to describe the magnetic susceptibility.

2.5 - RESULTS

2.5.1 - Magnetite Results

The T_1 surface relaxivities calculated for each magnetite sample plotted against the weight percent are shown in figure 2.1. Due to magnetite's very large magnetic

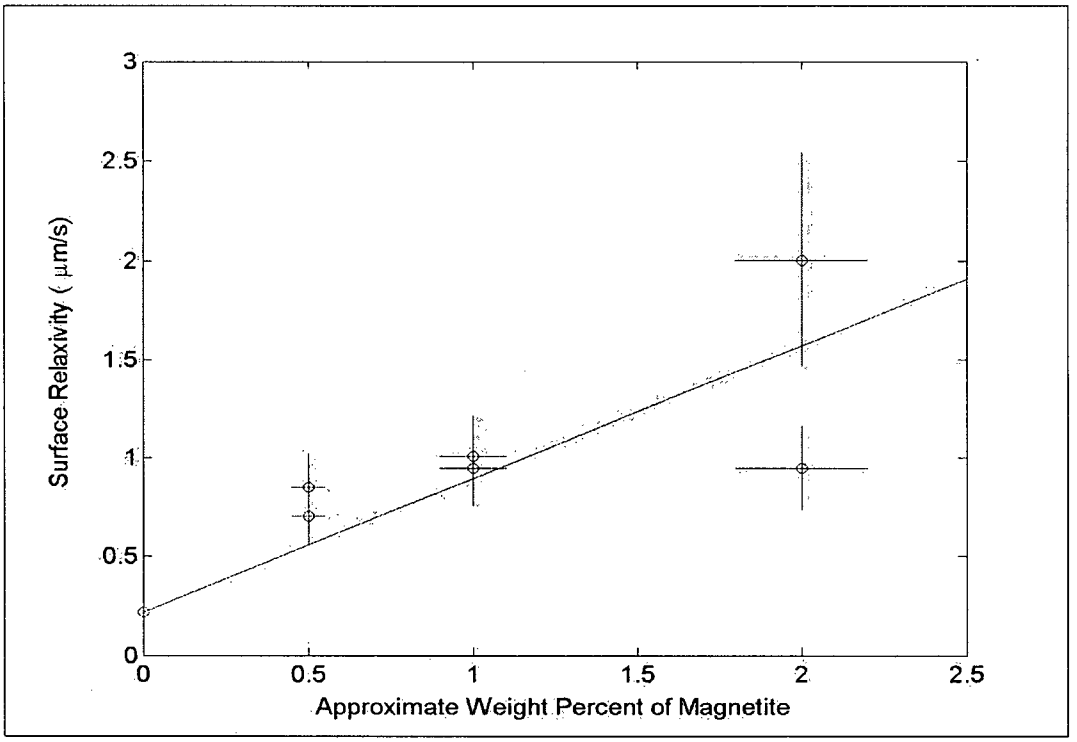

Figure 2.1 – T_1 surface relaxivity versus the approximate weight percent of magnetite for each magnetite mixture.

susceptibility, the T_2, which is required to measure T_1 (see Appendix A), was very fast and it was not possible to obtain T_1 values for weight percents larger than 2, as the signal decayed too quickly to be measured. The line of best fit shown on the diagram is a least squares best-fit line that was forced through the y axis at 0.22 μm/s, the measured value of the surface relaxivity of pure quartz. The R^2 value of this line is 0.59. The scatter in the data was interpreted primarily as error from the sample preparation, which lead to error in the weight percent of magnetite as was discussed in the previous section.

Figure 2.1 also indicates that the range of surface relaxivities is quite large for the small interval of magnetite compositions varying from 0.22 μm/s and 2.0 μm/s. This provides an opportunity to illustrate a key point. As discussed earlier, many interpreters of NMR relaxation data have assumed the surface relaxivity was a constant. If this notion was applied to the magnetite data, failing to take into account the surface

relaxivity effects on the value of T_1 could cause the surface area to pore volume ratio to be miscalculated by an order of magnitude using equation 1.2. This would extend to significant error in permeability calculations. Clearly, the surface relaxivity must be estimated to avoid such uncertainty. The error bars shown in figure 2.1 show there is significant error associated with the surface relaxivity, which is the result of the propagation of the error from each of the relevant parameters.

Table 2.3 shows the values for the surface relaxivity and the magnetic susceptibility for each magnetite sample and figure 2.2 is a plot of the same data illustrating the trends. Not shown in table 2.3 are the values for T_{1B}, which were very close for each sample, ranging from 2.6 s to 2.9 s.

Approximate Weight Percent of Magnetite	T_1 **Value** (s)	T_1 **Error** (s)	ρ_1 **Value** (μm/s)	ρ_1 **Error** (μm/s)	Mass Susceptibility **Value** (10^{-5} m^3/kg)	Mass Susceptibility **Error** (10^{-8} m^3/kg)
0.5	1.66	0.042	0.703	0.108	1.24	2.15
0.5	1.55	0.012	0.848	0.158	0.603	1.18
1.0	1.45	0.005	1.01	0.183	1.75	3.17
1.0	1.51	0.013	0.947	0.173	1.49	2.81
2.0	1.39	0.064	0.948	0.162	1.68	3.18
2.0	0.904	0.102	2.00	0.510	3.74	6.44

Table 2.3 – Surface relaxivity and mass susceptibility values for each magnetite mixture.

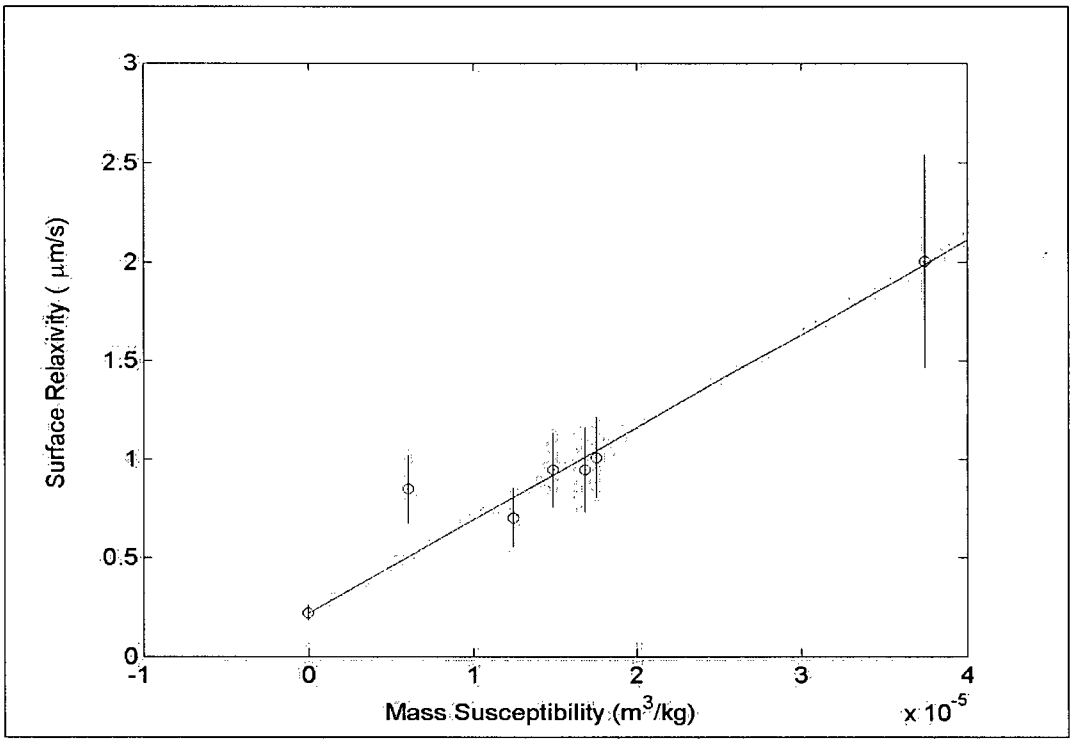

Figure 2.2 – T_1 surface relaxivity versus mass susceptibility for each magnetite mixture.

In figure 2.2, the line of best fit to the data, which was also constrained to pass through 0.22 μm/s, has an R^2 value of 0.92 demonstrating the excellent correlation between the surface relaxivity and the mass susceptibility of magnetite when magnetite is present in small proportions. The decrease in data scatter from figure 2.1 to figure 2.2 indicates that for these samples, using mass susceptibility to estimate the magnetic mineral content and surface relaxivity is superior to using the intended weight percent which is subject to mixing errors. The linear trend does depend largely on the data point for pure quartz. Fortunately, this point is well known and could be even smaller than 0.22 μm/s. Figure 2.2 lends support to the value of using mass susceptibility as a magnetic mineral indicator.

As an aside, the magnetic susceptibility can be used to determine the actual values of the magnetite weight percent in each sample. McNeill (1996) compiled the magnetic

susceptibility values of magnetite bearing rocks versus the volume percent from several studies. A reproduction of this is shown in figure 2.3.

Using the magnetic susceptibilities obtained in this study and the line of best fit through the McNeill (1996) data, the true volume percents were estimated, which in turn were converted to weight percents. The equation used was:

$$Volume\,Susceptibility = 2.6\times10^{-3}\,V^{1.33} \tag{2.11}$$

(Balsey and Buddington, 1958) where V is the volume percent of magnetite.

Table 2.4 shows the difference between the intended weight percents of the magnetite samples and the weight percents determined using figure 2.3. Caution must be exercised in applying relationships such as these as the susceptibility of magnetite does depend on the grain size, however the dependence decreases significantly at grain sizes larger than 1 μm (Mullins, 1977).

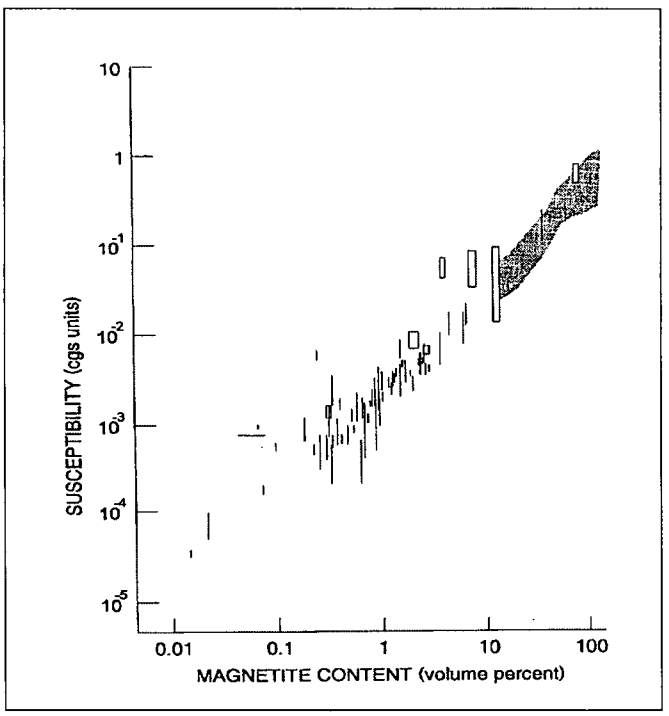

Figure 2.3 – Magnetic susceptibility of magnetite bearing rocks versus the volume percent of magnetite. Reproduced from McNeill (1996).

Sample Number	Intended Weight Percent	Weight Percent from McNeill (1996)
1	0.50	1.17
2	0.50	0.449
3	1.0	1.30
4	1.0	1.24
5	2.0	1.29
6	2.0	2.71

Table 2.4 – Approximate magnetite weight percents from sub-sampling and weight percents interpolated from McNeill's (1996) data.

The error in the weight percents does not considerably influence the calculation of the surface area and the density. Consequently, the surface relaxivity calculation is not notably altered due to the variation in the S/V calculation resulting from the different weight percents. Table 2.5 compares the surface relaxivities calculated using the initial estimate of S/V and the corrected value for S/V. The surface relaxivities originally presented in table 2.3 are denoted as the approximate surface relaxivities, while the values calculated using the corrected weight percents are called the corrected surface relaxivities.

Approximate ρ_1 **Value** (μm/s)	Approximate ρ_1 **Error** (μm/s)	Corrected ρ_1 **Value** (μm/s)	Corrected ρ_1 **Error** (μm/s)
0.703	0.108	0.705	0.138
0.848	0.158	0.850	0.157
1.01	0.183	1.01	0.183
0.947	0.173	0.944	0.173
0.948	0.162	0.947	0.199
2.00	0.510	2.01	0.510

Table 2.5 – Approximate surface relaxivities and corrected surface relaxivities for the magnetite mixtures.

In summary, the surface relaxivity is very sensitive to small changes in the ratio of magnetite grains to quartz grains. Figure 2.1 demonstrates that uneven sampling from the bulk mixture of each weight percent into sub-samples causes significant scatter in the surface relaxivity values due to slight differences in the amount of magnetite present in each sample. Mass susceptibility, which can also detect small differences in magnetite content, proves to be a good method of estimating the surface relaxivity as shown in figure 2.2. In addition, due to its linear dependence on magnetite content (figure 2.3), magnetic susceptibility can be used to calculate the true weight percent of magnetite in each sub-sample, as was shown in table 2.4.

2.5.2 - Hematite Results

The T_1 surface relaxivities calculated for each sample plotted against the approximate weight percent of pure hematite are shown in Figure 2.4. The weight percents of the pure hematite will be used for discussion. It was possible to measure T_1 on samples with large proportions of hematite as the magnetic susceptibility was much lower and consequently the NMR measurements were less affected by the diffusion through the internal magnetic field gradients.

The relationship between the surface relaxivity of the hematite mixtures and the approximate weight percent is more complicated than its magnetite counterpart. A logarithmic curve was fit to the data to illustrate the trends. The scatter of the data around the curve was again primarily attributed to errors in weight percent resulting from uneven sampling. The surface relaxivity increases significantly with weight percent of hematite at small fractions of hematite. At higher quantities, the surface relaxivity continues to increase as more hematite is added, but the rate of increase is much slower.

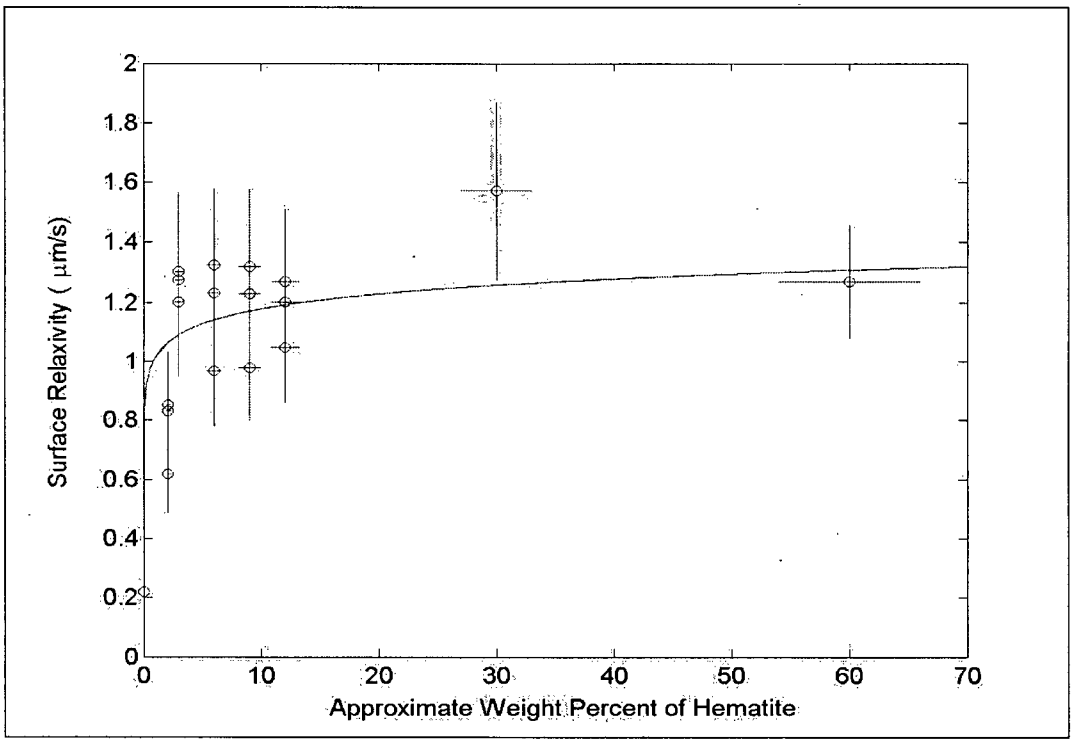

Figure 2.4 – T_1 surface relaxivity versus the approximate weight percent of hematite for each hematite mixture.

The surface appears to have less of a relaxing effect. This is reasonable as the probability of a water molecule encountering an Fe(III) site does not necessarily require the entire surface to be composed of these sites, as the molecule will likely encounter the surface on more than one occasion over the course of the relaxation experiment.

Kenyon and Kolleeny (1995) noted similar behavior for manganese ions sorbed to the surface of calcite particles at surface concentrations of 1.0×10^{-6} mol/m^2 to 8.0×10^{-6} mol/m^2. They described this effect as surface relaxivity saturation. If we postulate that in figure 2.4 the surface relaxivity begins to level off at 6% by weight of hematite, this corresponds to 4.3×10^{-3} mol of Fe(III)/m^2, which is much higher than the saturation concentrations seen by Kenyon and Kolleeny (1995).

The content of magnetic material at which surface relaxivity saturation is observed is expected to be smaller in materials with larger surface relaxivities. As a

result, the discrepancies between the Kenyon and Kolleeny data and the data presented in figure 2.4 could be a result of Mn(II) being a more efficient proton-relaxing agent than Fe(III). Kenyon and Kolleeny (1995) stated that they observed this type of behavior as well. In addition, sorbed ions may be more effective proton relaxers than distinct grains. The results of Bryar et al. (2000) suggest this is the case. Sorbed Fe(III) ions at a surface concentration of 1.0×10^{-9} mol of Fe(III)/m^2 had a surface relaxivity of 2.3×10^{-2} μm/s, while pseudobrookite grains in a concentration that provided a similar surface ion concentration had a surface relaxivity of about 1.2×10^{-2} μm/s.

As with the magnetite samples, there is significant error associated with the surface relaxivity. This is again due to the propagation of error from the parameters used for calculation.

Table 2.6 shows the surface relaxivities and mass susceptibilities for each hematite mixture, while figure 2.5 is a plot that demonstrates the relationship between the two parameters. Again, the T_{1B} values are not shown, but they were similar for each sample, ranging from 2.6 s to 2.8 s.

As with figure 2.4, a logarithmic curve is fit to the data to illustrate the trend of the surface relaxivity of hematite. The mass susceptibility is clearly related to the surface relaxivity and again, the surface relaxivity initially increases rapidly with mass susceptibility, but then levels off at higher magnetic susceptibilities. This relationship also depends largely on the values of the first few points, however we have discussed the relaxivity for pure quartz is well constrained. The scatter of the data around the curve is reduced from that observed in figure 2.4.

Approximate Weight Percent of Hematite	T_1 **Value** (s)	T_1 **Error** (s)	ρ_1 **Value** (μm/s)	ρ_1 **Error** (μm/s)	Mass Susceptibility **Value** (10^{-7} m^3/kg)	Mass Susceptibility **Error** (10^{-8} m^3/kg)
0	2.28	0.047	0.220	0.0390	-0.036	0.0030
2.1	1.51	0.034	0.854	0.179	1.51	0.318
3	1.18	0.022	1.30	0.263	3.80	3.05
6	1.08	0.025	1.33	0.253	7.59	6.37
9	1.06	0.051	1.23	0.243	4.81	3.54
12	1.02	0.033	1.20	0.219	4.41	2.64
2.1	1.65	0.030	0.619	0.131	1.67	0.297
3	1.22	0.044	1.20	0.255	3.40	1.38
6	1.26	0.018	0.967	0.186	3.36	1.63
9	1.21	0.008	0.979	0.178	3.59	0.948
12	1.07	0.006	1.05	0.188	6.99	5.53
2.1	1.52	0.073	0.832	0.193	1.44	0.337
6	1.12	0.028	1.23	0.244	6.10	2.50
9	1.00	0.037	1.32	0.257	2.25	5.00
12	0.943	0.034	1.27	0.242	5.30	1.35
30	0.590	0.035	1.57	0.297	13.0	6.37
60	0.502	0.018	1.27	0.187	49.7	8.18

Table 2.6 – Surface relaxivity and mass susceptibility values for each hematite mixture.

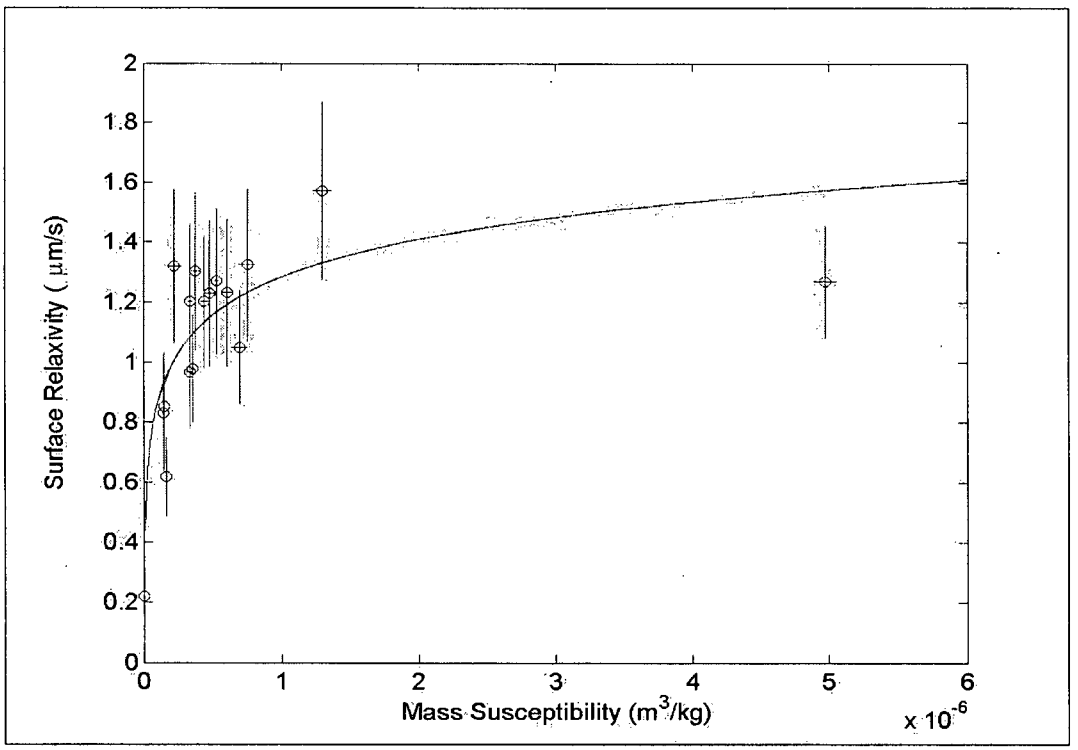

Figure 2.5 – T_1 surface relaxivity versus mass susceptibility for each hematite mixture.

As was mentioned, hematite has a range of potential mass susceptibilities, which can span from 1.0×10^{-7} m^3/kg to 7.0×10^{-6} m^3/kg, but the average value is 1.3×10^{-6} m^3/kg (Carmichael, 1989). Clearly, this may cause problems in using magnetic susceptibility to estimate hematite content and more importantly, surface relaxivity. However, the average value for pure hematite reported by Carmichael (1989) is 1.3×10^{-6} m^3/kg and it coincides well with the measured mass susceptibilities. Figure 2.6 is a plot of the mass susceptibilities measured at the various approximate weight percents of the dry mixtures, along with the average literature value for 100% hematite. With the exception of the value for 60 percent hematite by weight, which I hypothesize is inaccurate, the average pure hematite value corresponds well with the measured data. Figure 2.6-A is the relationship including the 60 percent hematite by weight data point and figure 2.6-B is the same plot excluding this data point. The scatter is partly due to the error in the weight percents.

This illustration was included to show that despite the potential range of hematite susceptibilities, the average value reported by Carmichael (1989) may be representative of most hematite samples. This would allow the relationships developed in this thesis to be used for most hematite bearing rocks.

There is also a grain size dependence on the magnetic susceptibility of hematite, which according to Nagata (1961), becomes insignificant at grains sizes that are larger than 100 μm. Nevertheless, according to Nagata (1961) the susceptibility only varies over a factor of 2.5 at smaller grains sizes.

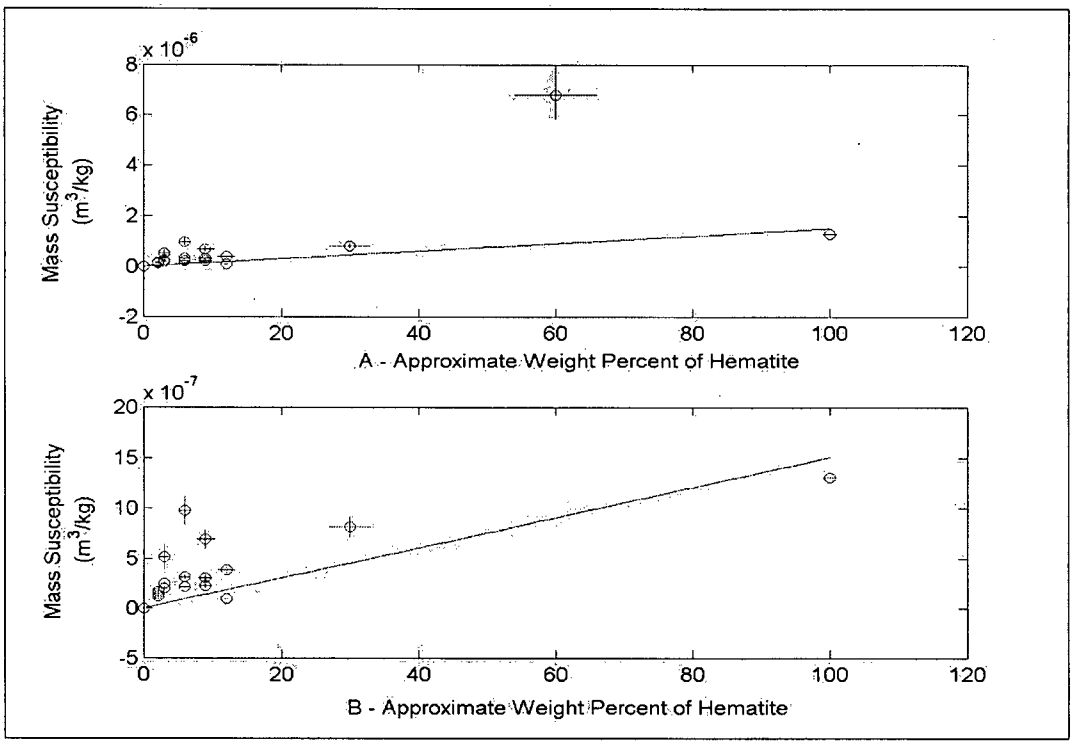

Figure 2.6 – Mass susceptibility versus the approximate weight percent of hematite for each hematite mixture and the literature value for 100% hematite. Figure 2.6-A is the plot for all the data, while figure 2.6-B excludes the erroneous data point at 60 percent hematite by weight.

In summary, there is a good correlation between the mass susceptibility and the surface relaxivity of hematite bearing samples shown in figure 2.5, which is similar to, but an improvement on the relationship of the surface relaxivity with weight percent of hematite shown in figure 2.4. Furthermore, even with the range of susceptibilities possible for hematite, figure 2.6 indicates the mass susceptibility could be used to obtain hematite content for many hematite-bearing rocks. The value for 60% hematite is believed to be erroneous as it departs significantly from the linear trend. It is possible this sample contains some magnetite impurities. To the best of my knowledge, a compilation of magnetic susceptibility values analogous to the one McNeill (1996) presented for magnetite has not been completed for hematite bearing rocks.

2.5.3 - Magnetite and Hematite Results Compared

Both the hematite and the magnetite samples show a correlation between the surface relaxivity and mass susceptibility. The magnetite trend is linear, whereas the hematite samples exhibit surface relaxivity saturation at higher mass susceptibilities. Since it has been shown the mass susceptibility in this study is a reliable measure of magnetic content, it will hereafter be assumed that the lower mass susceptibilities correspond to lower weight percents of the magnetic mineral in each sample.

I theorize the two minerals possess very similar trends and the observed discrepancies in their behavior with mass susceptibility is a result of differences in the range of the sample's magnetic mineral content. The surface relaxivity of magnetite is expected to saturate at higher weight percents and further experimentation at lower magnetic fields is required to investigate this hypothesis.

In addition, a linear trend can be used to approximate the behavior of hematite at low mass susceptibilities and is shown in figure 2.7. The trend line fits the data with an R^2 value of 0.58.

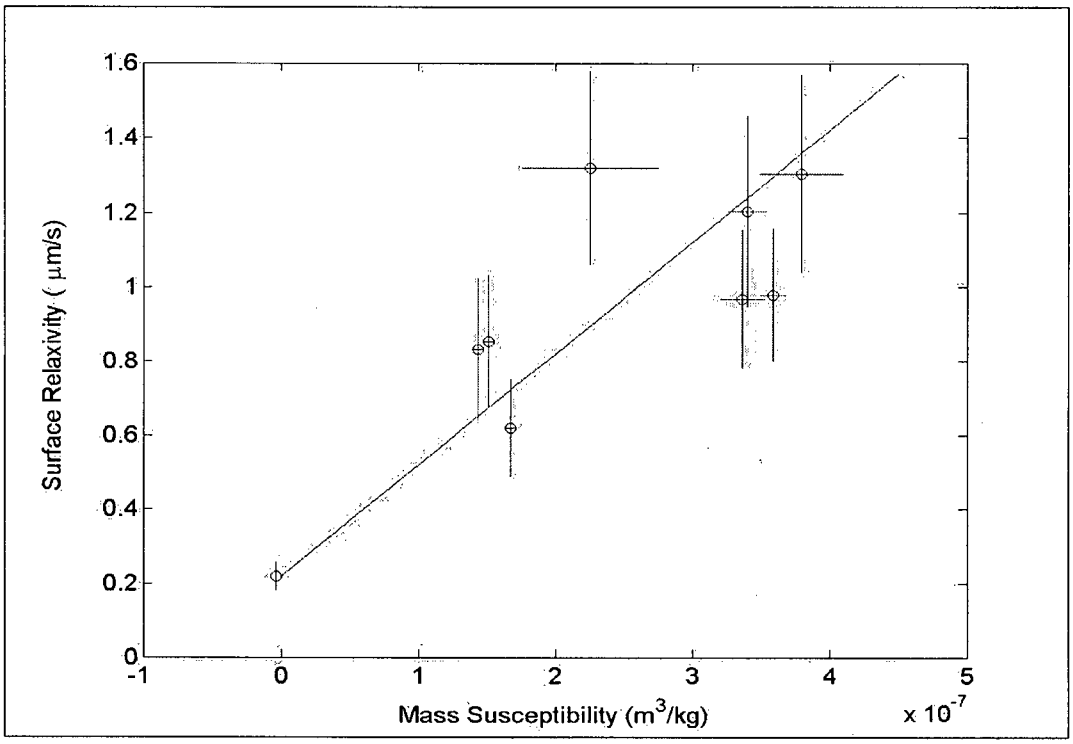

Figure 2.7 – T_1 surface relaxivity versus mass susceptibility for the hematite mixtures with low values of mass susceptibility.

Figure 2.8 shows the hematite and magnetite relationships in a single plot and illustrates that the relationship between the surface relaxivity and the magnetic susceptibility is not simple.

Hematite and magnetite cannot be combined into one all encompassing relationship. However, by examining figure 2.8 we see the lowest mass susceptibility measured for the magnetite samples was 6.0×10^{-6} m^3/kg for a sample with 0.45 percent magnetite by weight, while the maximum susceptibility measured for the hematite was 5.0×10^{-6} m^3/kg for a mixture of 60 percent hematite by weight. All mineral mixtures had grain sizes on the same order of magnitude (1×10^2 μm). I speculate that in this range of grain sizes, it is possible there may be little overlap in the mass susceptibilities for hematite and magnetite. In other words, a very small number of magnetite grains may have a larger magnetic susceptibility than the practical range of hematite susceptibilities.

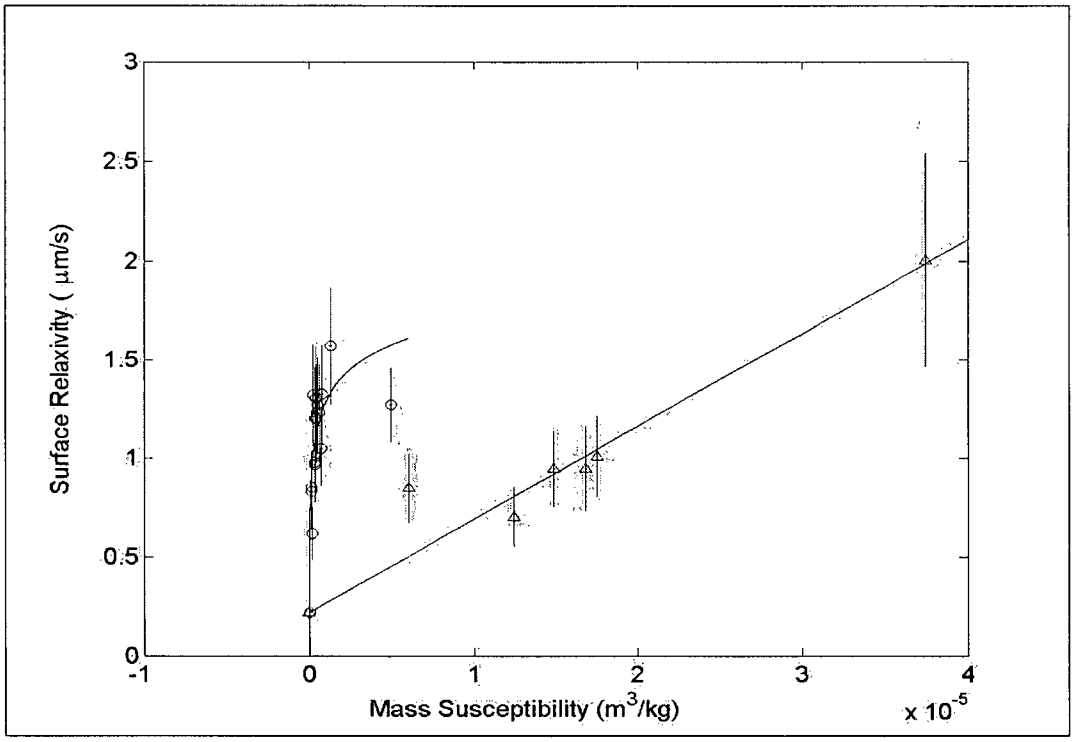

Figure 2.8 – T_1 surface relaxivity versus mass susceptibility for the hematite mixtures (circles) and magnetite mixtures (triangles).

The reasoning for this is as follows. A 0.45 percent by weight mixture of magnetite in quartz that weighs a total of 0.8 grams, does not contain a large number of magnetite grains and yet the mass susceptibility was larger, at 6.0×10^{-6} m^3/kg, than even a 60 percent by weight hematite sample. In addition, Scollar et al. (1990) stated that hematite content in most sedimentary materials would not exceed 10 percent by weight. Table 2.6 shows that the mass susceptibility of a 10 percent by weight hematite sample was approximately 5×10^{-7} m^3/kg, which is an order of magnitude lower than the minimum susceptibility for the magnetite sample. Hence, there may be no overlap in susceptibility values for typical concentrations of these two minerals in near surface rocks. If this theory is correct, the relationship between the mass susceptibility and the surface relaxivity would be much simpler than is indicated in figure 2.8, as there would

be one surface relaxivity value for each mass susceptibility value. Further research is required on very small quantities of magnetite to test this hypothesis.

Paramagnetic minerals such as pyrite and biotite are reported to have similar magnetic susceptibilities to hematite (Carmichael, 1989). Further experiments on these and other ubiquitous magnetic minerals are also required to ascertain if the relationships for ferrimagnetic minerals and antiferromagnetic and paramagnetic minerals are indeed distinct.

In terms of the surface relaxivity, both minerals exhibit a decrease in their surface relaxivity as larger quantities of the mineral are added. The surface relaxivity for the sample as a whole can be calculated from the contribution of the surface relaxivity from each mineral. Therefore, the magnetic mineral surface relaxivity can be determined by the following relationship (in the case of magnetite):

$$\rho_{1magnetite} = \frac{\rho_{1measured} - S_{quartz}\rho_{1quartz}}{S_{magnetite}} \tag{2.12}$$

where $\rho_{1\ measured}$ is the measured surface relaxivity of the entire sample, $S_{magnetite}$ and S_{quartz} are the fractions of the surface area in each mixture of the magnetite and quartz respectively and $\rho_{1\ magnetite}$ and $\rho_{1\ quartz}$ are the surface relaxivities of the magnetite and quartz surfaces. Figures 2.9 and 2.10 show the surface relaxivities and the surface fractions of the magnetite and hematite grains respectively. The surface fractions of the magnetite were calculated using the corrected weight percents from the McNeill (1996) data, while the hematite surface fractions are approximate values calculated using the approximate weight percents of the sample hematite.

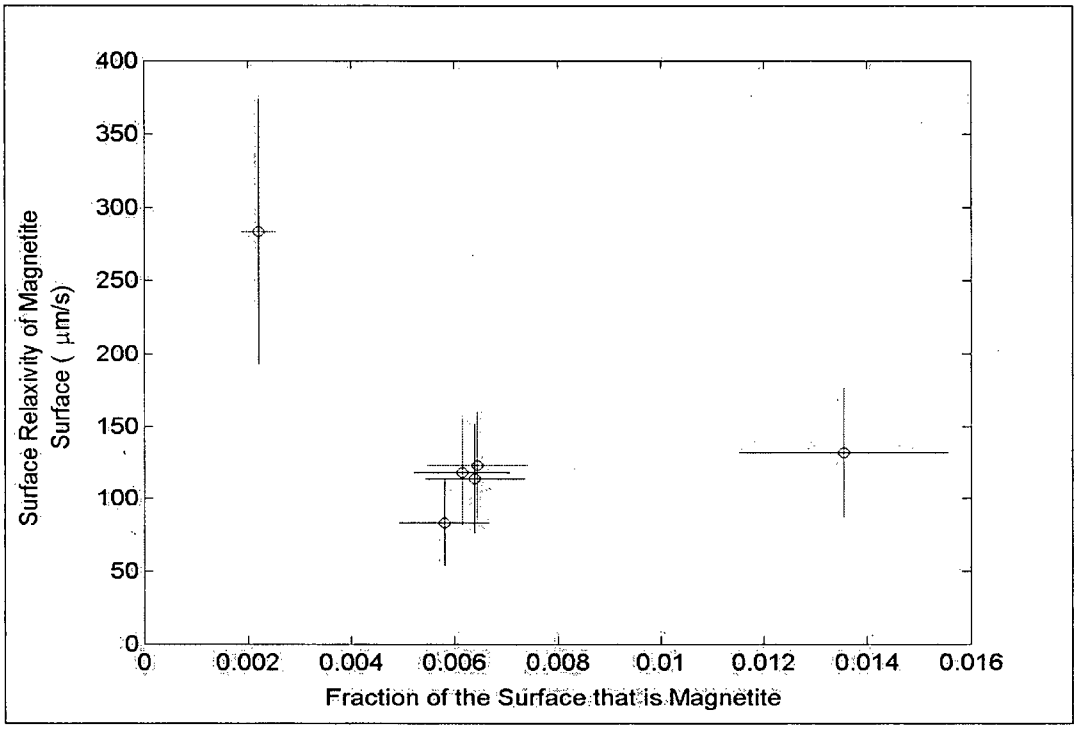

Figure 2.9 – T_1 surface relaxivity of the magnetite grains versus the fraction of the surface that is magnetite for each mixture.

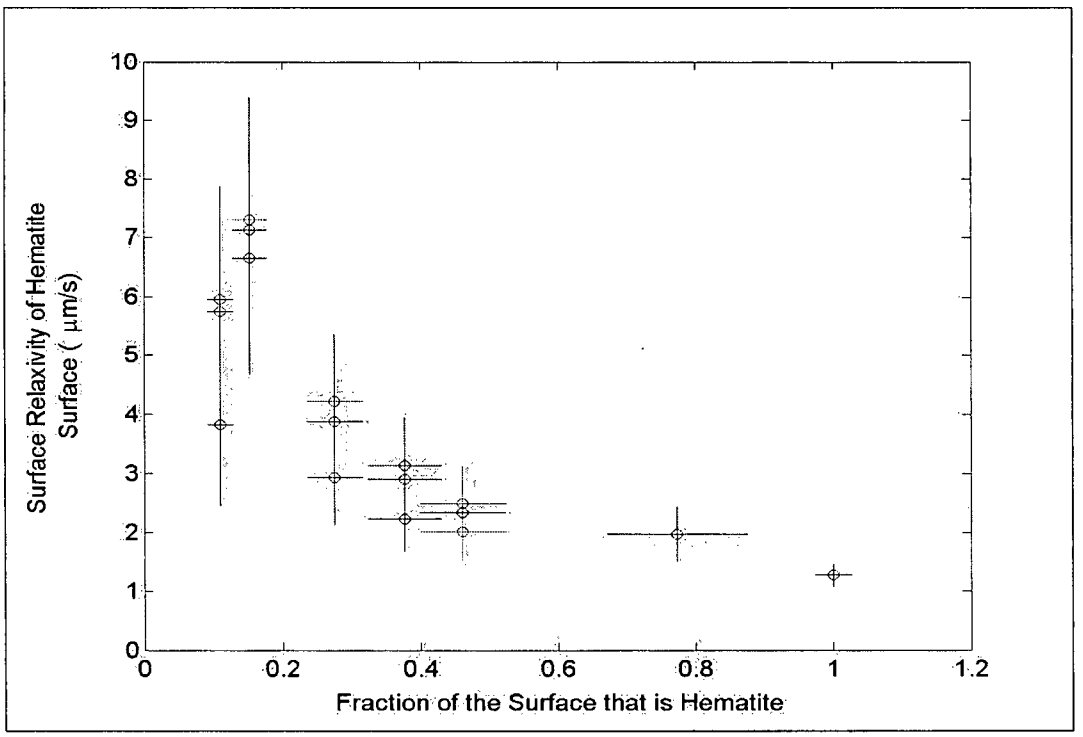

Figure 2.10 – T_1 surface relaxivity of the hematite grains versus the fraction of the surface that is hematite for each mixture.

Since the hematite grains were smaller than the magnetite grains, there is no overlap in the surface concentrations of the two minerals in the mixtures. Consequently, the surface relaxivity of the mineral surface cannot be directly compared for hematite and magnetite in similar concentrations. Nevertheless, figures 2.9 and 2.10 suggest the magnetite grains are more efficient proton relaxers than the hematite grains as the surface relaxivities are significantly larger for magnetite than hematite. This, in turn, indicates ferrimagnetic materials will have larger surface relaxivities than antiferromagnetic materials. This would be expected as ferrimagnetic materials will have a larger net magnetic field outside of each grain than will antiferromagnetic materials, which would result in enhanced surface relaxation (Myer Bloom, personal communication).

The surface relaxivities in the relationships presented in this chapter were calculated by equation 1.2. Utilization of this equation to calculate a single surface relaxivity from a single T_1 and S/V is valid as long as several conditions are met. Some earlier studies have applied equation 1.2 improperly and the result has been confusing and contradictory surface relaxivity values and relationships, some of which were discussed in the background section. The following section will identify the criteria that must be met to accurately utilize equation 1.2 and explain how the procedure used in this study attempted to meet these requirements.

2.6 – DISCUSSION

There are four aspects of the T_1 relaxation measurements and surface relaxivity calculations that require discussion to clarify exactly what the surface relaxivities

represent and illustrate the usefulness of the relationships with respect to natural geological environments. For each sample, a monomodal T_1 distribution was measured and its logmean was calculated and used as the T_1 in equation 1.2. Discussion as to what this distribution represents physically is necessary to understand what the T_1 used for surface relaxivity calculations characterizes. In addition, the position and shape of the T_1 distribution is dependent on the experimental conditions and on the inversion procedure employed and these effects need to be addressed. The surface area used to calculate the S/V is also subject to variability depending on the method utilized for measurement, which in turn leads to variation in the calculated surface relaxivities. Finally, in applying equation 1.2, the S/V value and the T_1 must correspond to the same pore size or average pore size. Under some circumstances this may be difficult to ensure. However, failing to do so also gives rise to erroneous surface relaxivity values.

2.6.1 - Sample Preparation and T_1 Distributions

Narrow monomodal T_1 distributions, such as the ones recorded in this study, usually indicate the sample under investigation has a narrow range of pore sizes. It is also typically assumed the water protons relaxing in the sample are each confined to a certain pore and each T_1 in the distribution represents one pore size. In unconsolidated materials there is the possibility that the protons are diffusing between pores, which would make the T_1 distribution more difficult to interpret, as a single T_1 would no longer represent a single S/V. Whether or not the protons will diffuse between pores depends on the size of the pores and the conduits connecting the pores, compared with the distance a proton diffuses over the course of the NMR experiment. If the diffusion distance is significantly larger than the pore size, it is probable there will be diffusion between pores

in unconsolidated materials, which tend to have large pore throats. Let us discuss the hematite and quartz samples used in this study and compare the pore size and the distance over which the protons will travel during an NMR T_1 relaxation measurement to determine the likelihood of inter-pore diffusion.

The hematite grain diameters varied from 1.0×10^2 μm to 3.3×10^2 μm. Assuming simple hexagonal packing of perfect spheres, the maximum pore radius resulting from the packing of monosized grains can be calculated using 0.53 × radius of the grain (Bourbie et al., 1987). As a result, the pores in a sample of pure hematite, could range from 53 μm to 1.1×10^2 μm in diameter, but could be smaller than 53 μm. The quartz, which had grain sizes as large as 4.0×10^2 μm, could have pores as large as 2.1×10^2 μm in diameter.

For the majority of the samples in which the hematite and the quartz existed together, the smaller grains of hematite likely filled in spaces created by the larger quartz grains. This effect would also likely occur in the pure minerals, which also had a narrow distribution of grain sizes. This conceivably resulted in smaller pores than predicted for either the hematite or quartz alone. Application of the following equation provides justification for this idea:

$$\frac{S}{V} = \frac{6((1/\theta)-1)}{d} \tag{2.13}$$

where θ is the porosity and this equation applies to the random packing of monosized spheres (Latour et al., 1993). Equation 2.13 can be used to calculate the pore size, S/V, of sediment from the diameter, d, of the grains and the porosity. The S/V values calculated using equation 2.13 were quite different from those calculated from the surface area measurements. For example, for the pure quartz sample, which is assumed to be

composed of grains approximately 4.0×10^2 μm in diameter, equation 2.13 calculated an S/V value of 2.3×10^2 1/cm. A porosity of 0.4, which is the theoretical value for a simple hexagonal packing of spheres, was used for consistency despite the fact the porosity values calculated for these samples were closer to 0.5. The measured value of surface area to volume ratio for the quartz sample was 3.7×10^3 1/cm ± 8.0×10^2 1/cm.

Since larger S/V values correspond to smaller pore sizes, equation 2.13 predicted a much larger pore size than was measured for the samples. This supports the theory of the smaller grains filling in spaces between larger grains and resulting in overall smaller pores. Minor surface roughness of the grains may also have contributed to the added surface area of the samples, as well as any departure from the spherical model of the grains, both of which would result in larger S/V values. Overall, the pore sizes of the hematite and quartz samples are presumably at the lower end of the calculated pore diameter range of 53 μm to 2.1×10^2 μm and perhaps even smaller. The S/V calculations for the hematite and quartz samples do not take into account additional pore size reduction due to grain size differences between the hematite and quartz and the measured S/V values may be slightly higher than were reported and the pore sizes will be even smaller.

To calculate approximately how far the protons diffused (l_d) during the relaxation process the following equation is used:

$$l_d = \sqrt{Dt} \tag{2.14}$$

where D is the diffusion coefficient of the proton and t is time. Initially, we will assume D is equal to the unrestricted self-diffusion coefficient of water at 40°C, which is the temperature at which the NMR measurements were made and this value is equal to

2.3×10^{-5} cm^2/s. In the pure quartz sample, which had the longest T_1 relaxation time of 2.3 s, the protons diffused a distance of 72 μm over the course of the experiment. In comparison, protons in the 60 percent hematite sample, which had the shortest T_1 time of 0.50 s, diffused a distance of 34 μm. When confined in a pore space, the diffusion coefficient is reduced (Latour et al., 1993). The degree to which it decreases depends on the amount of time the protons diffuse. For comparison, if the diffusion coefficient is reduced to 70% of its value, which Latour et al. (1993) showed was the limit for a sphere pack with diameters of 96 μm; the protons would diffuse 61 μm in the pure quartz and 28 μm in the 60 percent hematite sample. Since the pore diameters are likely less than the calculated range of 53 μm to 2.1×10^2 μm, the diffusion calculations indicate the protons in each pore are probing the extent of pore space and could also be traversing between pores.

Let us now address how this diffusion between pores would influence the T_1 distribution. Kenyon (1997) discussed that for T_1 measured on unconsolidated synthetic samples, diffusion would average out the pore sizes, causing a monomodal T_1 distribution to be measured. Ramakrishnan et al. (1999) also showed that for T_2 data, there would be an averaging effect between two different pore sizes, if diffusion was significant. Therefore, the T_1 distribution for unconsolidated samples will be an averaged distribution of the pore sizes and the logmean of the distribution will represent the average pore size for these samples. This averaging effect may break down if the pore sizes are significantly different, however the hematite and quartz mixtures have a pore size range that is small compared to the range possible in natural rocks (Ramakrishnan et al., 1999).

As it turns out, inter-pore diffusion is necessary to explain the results for some of the samples. In the mixtures with very small amounts of the magnetic mineral, some pores will have magnetic grains to aid in the surface relaxation, while others will have only quartz. If there were not communication between pores, one would expect to see two separate T_1 peaks, one representing the proton relaxation in pores with no magnetic grains and one representing pores with the enhanced relaxation. However, there was actually only one observable peak for each sample, requiring that each proton was experiencing the same surface relaxivity.

2.6.2 - T_1 Measurement and Calculation

In the last section, I described how the T_1 distribution arises from the geometry and physics of the pore space. In addition, the position and shape of the distribution depends on experimental and analysis procedures. Measurement of T_1 relaxation from a rock sample is dependent on the Larmor frequency at which the measurements are made. Bryar measured T_1 on the same sample at Larmor frequencies of 1 MHz and 90 MHz and surface relaxivities of 5.6 μm/s and 2.0 μm/s respectively were calculated from the distributions (Traci Bryar, personal communication). This illustrates that higher Larmor frequencies result in larger T_1 times. Kleinberg et al. (1993) also showed that the average value of a T_1 distribution for some naturally occurring sandstones, increased slightly as the Larmor frequency increased. Some question also exists as to whether temperature affects the NMR response, however several studies have shown that both T_1 and T_2 do not vary significantly with temperature (Latour et al., 1992, Roberts et al., 1995 and Foley et al., 1996).

To ensure the relationships developed between surface relaxivity and magnetic susceptibility are useful, all potential users should adopt a standard set of experimental parameters. This study measured T_1 at a Larmor frequency of 90 MHz. Borehole instruments tend to use Larmor frequencies of 1 MHz to 2 MHz. It would therefore be ideal to use similar frequencies for laboratory experiments. Due to instrument limitations, 90 MHz was the only option for this study.

The T_1 value used for analysis is affected by the manner in which the multi-exponential decay data are inverted and by the method used to average the resulting T_1 distribution, since most naturally occurring rocks have several pore sizes. Borgia et al. (1996) was the only study that analyzed the effects of different data representations on the calculated surface relaxivity value. They measured T_1 on 77 sandstones from 12 field sites. When a 5-component multi-exponential fit was used to interpret the raw data and the average T_1 of the resulting distribution was taken, ρ_1 varied from 0.92 to 7.1 μm/s. Alternatively, when a 5-component fit to the raw data was used with a geometric mean relaxation time, ρ_1 was between 0.22 and 2.3 μm/s. Finally, when another multi-exponential fitting procedure called a stretched exponential was used to determine the relaxation times, T_1 relaxivities ranged from 0.15 to 2.2 μm/s.

A consistent method of inverting for the T_1 distribution is required. In addition, a common method of averaging the resulting distribution is also needed. In the case of the study, the samples used were geometrically very simple and had a narrow range of pore sizes; thus each T_1 distribution was a narrow monomodal distribution. Averaging in this situation was simple and reliable as was discussed in the previous section. Most averaging methods would result in similar values.

2.6.3 - Measuring the Surface Area and Calculating S/V

Several methods exist for measuring surface area, each of which corresponds to a different length scale. The calculated surface relaxivity will be dependent upon the method applied. For example, Roberts et al. (1995) calculated ρ_1 for 10 sandstone plugs at 30 MHz and found a range from 9 μm/s to 1.2×10^2 μm/s. Borgia et al. (1996) calculated ρ_1 for 77 sandstone samples at 20 MHz and found a range of 0.92 to 7.1 μm/s for the surface relaxivities. Roberts et al. (1995) used a thin-slice back-scatter electron imaging method to determine the surface area to volume ratio, while Borgia et al. (1996), measured the surface area by BET N_2 adsorption and calculated the S/V using the grain density and the porosity. Roberts' method analyzes the pore surface at a larger length scale than Borgia's method and leads to smaller S/V values and larger calculated ρ_1 values. Since both studies failed to provide chemical analyses of the sandstones, the differences could also be partly due to the mineralogy.

Both methods are valid surface area measurements. Nonetheless, this obviously poses a problem in correlating the surface relaxivity with magnetic susceptibility if the value of the surface relaxivity is so sensitive to experimental methods. This study used the BET method to determine the surface area of the samples. Since there was no clay or very fine particles within the samples, it is believed that most methods would calculate similar surface area to volume ratios and the resulting surface relaxivity values would also be very close. There is the possibility that some surface roughness is present on the grain surfaces, which would result in higher surface area measurements for the BET N_2 technique than an optical method.

2.6.4 - Correlation of T_1 and S/V

In calculating the surface relaxivities for magnetic samples using equation 1.2, single values for T_1 and S/V value are typically used. In naturally occurring rocks, a distribution of T_1 values are usually measured and the surface area of the pore space varies with the method used for measurement. The surface relaxivity is normally calculated by averaging the T_1 distribution and using the measured S/V. In the case of a simple sandstone, there is a narrow distribution of pore sizes and each pore size is present in similar numbers. The S/V calculated from a surface area measurement in this case would probably represent the average pore size and using it in combination with an average T_1 to calculate surface relaxivity would be valid.

Under some circumstances the average T_1 and the measured S/V do not represent the same pore size. For example, if there is a significant amount of clay in the sample, it will dominate the BET surface area measurement, while the T_1 distribution may still correspond to the overall pore size distribution. Using the S/V calculated from the surface area measurement and the average of the T_1 distribution to calculate a surface relaxivity would be incorrect.

Hurlimann et al. (1994) suggested that optical methods measure surface area at the length scale which governs fluid flow, while N_2 BET measures surface area at a smaller scale that can be dominated by surface roughness, which is not as important for fluid flow. Separate relationships could be established between magnetic susceptibility and the surface relaxivity calculated using the average of the T_1 distribution and the two values of ρ_1, one calculated through BET measurements and one calculated by optical methods. Interpreters could then use the relationship that best suited their objective. This

procedure would provide a single S/V value for a T_1 distribution at the length scale desired.

The real strength of NMR however, is in its ability to resolve a wide range of pore sizes from a single sample. This study calculated the surface relaxivity of very simple samples that had a narrow pore size distribution, such that a single representative T_1 value could be calculated. The samples also lacked clay that dominates the surface area measurements. I believe the calculated S/V and the average of the T_1 distribution represented the same pore geometry and the relationships developed can be used to predict the surface relaxivity. As a result, ρ_1 can be used to calculate the S/V distribution from the T_1 distribution. These relationships are valid for rocks with a small clay fraction and rocks where the magnetic component exists as distinct grains.

2.7 - CONCLUSIONS

The primary objective of this chapter was to assess if a relationship exists between the magnetic susceptibility and the T_1 surface relaxivity of sediments in order to predict the surface area to volume ratio of the pore space. Mixtures of ferrimagnetic magnetite and antiferromagnetic hematite combined with quartz in varying quantities were created to mimic naturally occurring unconsolidated sediments. The magnetite samples and the hematite samples showed a good correlation between the T_1 surface relaxivity and the magnetic susceptibility. Since borehole instruments can make both measurements, these results indicate there is considerable potential for using the magnetic

susceptibility to estimate the surface relaxivity in borehole environments for unconsolidated sediments, which can then be used to estimate the pore size distribution.

A second significant contribution of these experiments was the systematic measurement of the surface relaxivity in sediments with varying concentrations of common iron-bearing minerals. Some studies have investigated the trends of laboratory-engineered samples in which paramagnetic ions were sorbed or imbedded on non-magnetic surfaces (Kenyon and Kolleeny, 1995 and Foley et al., 1996). These types of samples allow the methodical measurement of surface relaxivity, however the perfect distribution of magnetic ions throughout calcite and quartz grains is somewhat unrealistic in most geological environments. Other studies looked at rocks collected from field sites and calculated the surface relaxivities (Borgia et al., 1995 and Dodge et al., 1995). These types of experiments have the benefit of representing real geological systems, but determining the amount of magnetic material contributing to the surface relaxivity is more difficult.

The samples used in this thesis represent an intermediate scenario in which commonly occurring minerals were used, but the concentrations of each were carefully controlled. This allowed the variation in surface relaxivities to be examined in materials that were well characterized, but also representative of naturally occurring sediments. Bryar et al. (2000) undertook an investigation in which the trend of surface relaxivities for small concentrations of the mineral pseudobrookite were recorded, but did not look at higher concentrations.

One potential source of error in the surface relaxivity calculations may be that the S/V values used to calculate ρ_1 do not represent any additional decrease in the pore size

resulting from the mixture of the hematite and magnetite with quartz. I do not believe this effect will be large, however further experiments should be completed to quantify this influence. If this mixing effect was significant it would lower the surface relaxivities discussed in this chapter but the trends with the magnetic susceptibility and the weight percent of each magnetic mineral would not be altered.

The magnetite surface relaxivity showed a linear trend with increasing amounts of magnetite, while hematite's surface relaxivity showed a linear trend at smaller concentrations of the mineral and then leveled off at higher concentrations. These observations agree with previous studies on sediments with sorbed paramagnetic ions on non-magnetic surfaces (Kenyon and Kolleeny, 1995).

Finally, it was suggested that magnetite, which has a much larger magnetic susceptibility than hematite may also have a higher surface relaxivity than hematite for a given amount of the magnetic mineral. This suggests ferrimagnetic minerals will have larger surface relaxivities than antiferromagnetic minerals. This is a characteristic that was expected but had never been measured or quantified.

Future work could include investigation into the relationship between magnetic susceptibility and paramagnetic minerals. Additional measurements on small quantities hematite and magnetite and other ferrimagnetic minerals could be completed to solidify the trends introduced in this chapter. Finally, an assessment of the ability of the magnetic susceptibility and surface relaxivity relationships to predict the surface relaxivity in more complex rocks should be completed.

3 - PARAMETRIC INVERSION FOR NUCLEAR MAGNETIC RESONANCE T_2 DATA

3.1 - INTRODUCTION

In Chapter 2, it was demonstrated that magnetic susceptibility could be used to estimate ρ_1 from T_1 data, which could then be used to calculate the pore size of the material under investigation. In this chapter, a second method will be presented for the interpretation of T_2 data that under some circumstances can simultaneously estimate ρ_2 and S/V and also the internal gradient, G.

The NMR relaxation time T_2 depends on the surface relaxivity, the S/V and the relaxation of bulk water. In addition, equation 1.8 shows that diffusion of protons through local magnetic field inhomogeneities or effective internal gradients (Hurlimann, 1998) further decreases T_2. The diffusion term depends on the strength of these internal gradients, which in turn depends on the magnetic susceptibility difference between the pore fluid and the grain and also on the magnitude of the external field. If either of these quantities is large, T_2 will be significantly smaller than T_1. For example, in rocks with substantial amounts of iron bearing minerals the magnetic susceptibility difference can be very large and T_2 relaxation due to internal gradients is important. Often, a Carr-Purcell-Meiboom-Gill (CPMG) experiment is effective in removing the added relaxation in internal gradients by using short echo times and this method is widely used (Carr and Purcell, 1954 and Meiboom and Gill, 1958). Please see Appendix A for a detailed description. The usefulness of the CPMG sequence is reduced however, as the strength

of the internal gradient increases. Interpreting T_2 data are consequently much more difficult than interpretation of T_1.

A unique solution to this problem was proposed by Slijkerman and Hofman (1998) who showed that a modified version of equation 1.8 can be used to solve for the surface relaxivity and surface area to volume ratio when the unrestricted diffusion coefficient of the pore fluid and the internal gradient are known and T_2 was measured at two or more echo times. The modified equation is:

$$\frac{1}{T_2} - \frac{1}{T_{2B}} = \rho_2 \frac{S}{V} + \frac{D_o \gamma^2 G^2 t_e^2}{12} - D_o \frac{4}{9\pi} \frac{S}{V} \sqrt{D_o t_e} \frac{\gamma^2 G^2 t_e^2}{12} \tag{3.1}$$

where D_o is the free diffusion coefficient of water. They assumed that internal gradients were negligible and they applied an external field gradient, G. I suggest a similar approach could be used to determine ρ_2, S/V and the average internal magnetic field gradient, G, in samples that have significant internal field inhomogeneities induced by a uniform applied field.

In this study T_2 was measured and interpreted on the samples of hematite and quartz discussed in Chapter 2. Many of these mixtures have large susceptibility differences compared to the pore fluid. In addition, the relaxation times of the samples were measured at a uniform magnetic field strength of 2.2 Tesla. The relaxation due to internal gradients under these conditions could not be eliminated using a CPMG sequence. This situation is different from the one explored by Slijkerman and Hofman (1998), as the field gradients experienced by the protons are not known. However, since six measurements were made on each sample at different echo times, corresponding to six data, the three unknown parameters could potentially be obtained by error minimization.

An iterative, non-linear parameter estimation, as equation 3.1 is a non-linear equation, by error minimization can be accomplished using several methods. Local minimization methods attempt to find a set of model parameters that minimizes the difference between the observed data and the predicted data. A local minimization method known as the Newton method was used to solve for the surface relaxivity, surface area to volume ratio and the internal gradient for the hematite T_2 relaxation data.

3.2 - BACKGROUND

3.2.1 – Components of the Forward Model

The equation that describes relaxation time T_2 presented in Chapter 1 is equation 1.8:

$$\frac{1}{T_2} = \frac{1}{T_{2B}} + \rho_2 \frac{S}{V} + \frac{D_{eff}\gamma^2 G^2 t_e^2}{12}$$

There are two terms in this equation that require discussion as they complicate the interpretation of T_2 data. The effective diffusion coefficient of water, D_{eff}, depends on the environment of the diffusing protons and on the time the protons are allowed to diffuse. If the protons are unrestricted, D_{eff} equals the free diffusion coefficient of water (D_o), which varies with temperature and is 2.3×10^{-5} cm^2/s at 40°C. When water is contained in a pore space, the diffusion coefficient is reduced to some effective coefficient. Mitra et al (1993) showed that at short times D_{eff} is dependent upon the pore geometry:

$$\frac{D_{eff}}{D_o} = 1 - \frac{S}{V}\frac{4}{9\sqrt{\pi}}\sqrt{D_o t} - \frac{1}{12}(D_o t)\left\langle \frac{1}{R_1} + \frac{1}{R_2} \right\rangle + O\left((D_o t)^{3/2}\right) \qquad (3.2)$$

where R_1 and R_2 are radii of curvature of the pore space. At very short times, only the first two terms in equation 3.2 are important and D_{eff} becomes:

$$\frac{D_{eff}}{D_o} = 1 - \frac{S}{V}\frac{4}{9\sqrt{\pi}}\sqrt{D_o t} \tag{3.3}$$

(Latour et al., 1993).

At long observation times, the effective diffusion coefficient depends on the tortuosity, τ, of the pore space:

$$\frac{D_{eff}}{D_o} = \frac{1}{\tau} + \frac{\beta_1}{t} + \frac{\beta_2}{t^{3/2}} \tag{3.4}$$

where β_1 and β_2 are constants that depend on the microscopic properties of the pore space (Latour et al., 1993). The tortuosity of porous media is a measure of how well the pores are connected (Latour et al., 1995). Latour et al. (1993) interpolated between the short time and long time expressions by using a two point Pade approximant.

When T_2 relaxation is measured using a CPMG sequence the relevant observation time is the echo time, t_e, which can be kept very small (< 1ms). In this case the short time approximation for D_{eff} can be used and equation 3.3 can be written as:

$$\frac{D_{eff}}{D_o} = 1 - \frac{S}{V}\frac{4}{9\sqrt{\pi}}\sqrt{D_o t_e} \tag{3.5}$$

(Slijkerman and Hofman, 1998). This expression can be substituted for the D_{eff} term in equation 1.8 to form the forward operator for this inversion presented initially as equation 3.1:

$$\frac{1}{T_2} - \frac{1}{T_{2B}} = \rho_2 \frac{S}{V} + \frac{D_o \gamma^2 G^2 t_e^2}{12} - D_o \frac{4}{9\pi}\frac{S}{V}\sqrt{D_o t_e}\frac{\gamma^2 G^2 t_e^2}{12} \tag{3.6}$$

The range of echo times at which this approximation is relevant can be determined for a given pore size by comparing the second and third terms of equation 3.2. For the samples used in this study, T_2 measurements were made at echo times less than 1 ms and the approximation of equation 3.5 is valid.

The second issue in utilizing equation 1.8 is the internal gradient is extremely difficult to calculate. The terms internal gradient, effective gradient and internal field inhomogeneities are all used to described the same parameter G. As mentioned earlier, internal field inhomogeneities caused by the susceptibility differences between the pore fluid and the grains can be approximated as effective gradients over the distance the protons diffuse during the experiment. The maximum effective gradient can be estimated using equation 1.7 (Hurlimann, 1998). Many groups have used various methods to measure and calculate these internal field inhomogeneities or internal gradients in rocks, a summary of which is given in Zhang et al. (2000). This group also developed theoretical models for the gradient distribution in different types of porous media and compared them to measurements.

In rocks with grains of varying magnetic susceptibilities, there may be several environments with different effective gradients, which may in turn vary the relaxation time of the protons in each of these environments. The practical calculation of a single, representative G to be used in the forward modeling of NMR data is consequently very difficult.

Equation 3.6 shows the forward model in its entirety. The unknowns are the surface relaxivity, the surface area to volume ratio and the internal gradient. To the best

of my knowledge, Slijkerman and Hofman (1998) were the only other group to undertake a similar inversion to the one completed in this study.

3.2.2 – Features of the Forward Model

The shape of the function shown in equation 3.6 with respect to the echo time will vary depending on the size of the parameters ρ_2, S/V, G and also on the range of t_e. In the results section of this chapter, synthetic data were created using the model parameters $\rho_2=1.0\times10^{-3}$ cm/s, $S/V=4.7\times10^{3}$ 1/cm and $G=1\times10^{-2}$ T/cm. Figure 3.1 shows the shape of the forward model at these parameters for the echo times 0.1 ms to 1 ms, which is the typical range for T_2 experiments at high field strengths. The intercept of the function corresponds to the product of ρ_2 and S/V, which is 4.7/s in this example.

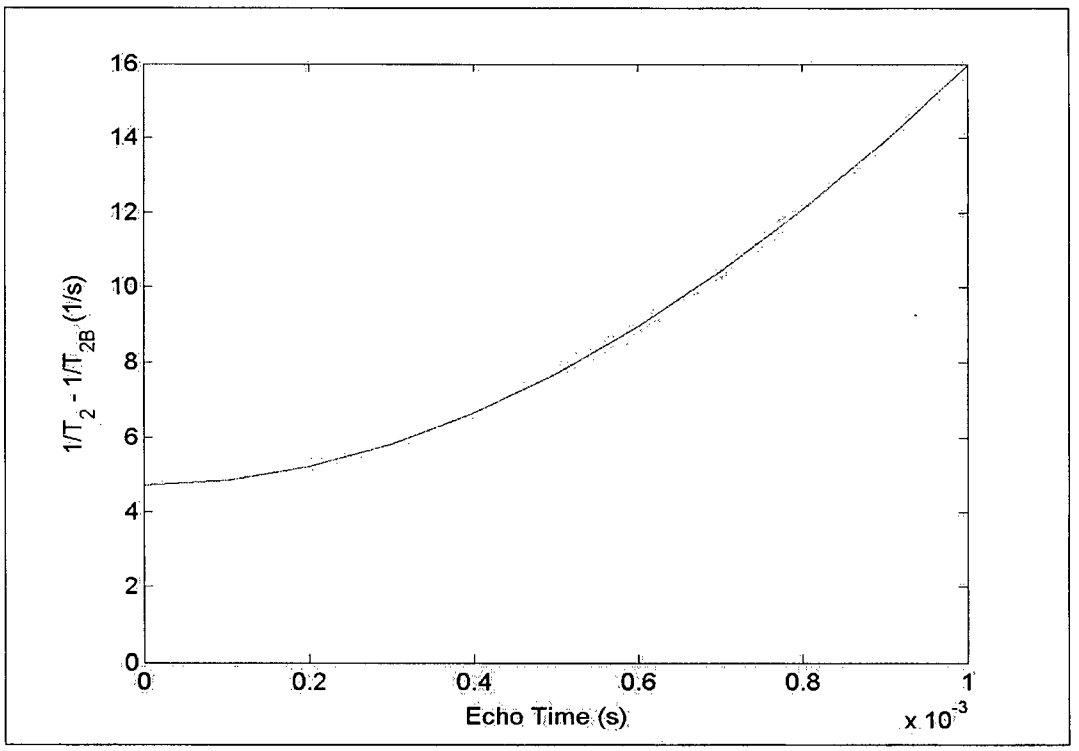

Figure 3.1 – Shape of the forward model for the parameter values $\rho_2=1.0\times10^{-3}$ cm/s, $S/V=4.7\times10^{3}$ 1/cm and $G=1.0\times10^{-2}$ T/cm over the echo times typically used in a high field T_2 experiment.

Taking a closer look at equation 3.6, one may recognize that the ability of the inversion to recover all three parameters will depend on the relative size of the three terms and on their size with respect to the noise in the data. In particular, the third term must be large compared to the noise, as it is required to distinguish between ρ_2 and S/V. If this condition is not met, only the product of ρ_2 and S/V can be determined from the data and we will see this in an issue for the synthetic data and to a lesser degree, the hematite data. As long as the second term is large compared to the error, the gradient can be estimated accurately from the data. Ideally, each of the three terms should be of similar size to extract the maximum amount of information about each parameter. Again, the fulfillment of these criteria will depend on the size of the parameters and the range of echo times used.

One method of increasing the size of the second and third terms would be to use large echo times. Figure 3.2 illustrates the shape of the forward model at the parameters $\rho_2=1.0\times10^{-3}$ cm/s, $S/V=4.7\times10^{3}$ 1/cm and $G=1\times10^{-2}$ T/cm for a large range of echo times.

The region of the curve in figure 3.2 where the slope is positive indicates the sum of the first and second term is increasing more quickly than the third term with increasing echo times. The region of the curve where the slope is negative represents the value of the third term beginning to "catch up" to the sum of the first and second terms. The second and third terms are of equal size when the value of the forward model equals the product of the surface relaxivity and the surface area to volume ratio. The third term becomes larger than the sum of the first and second term when the curve crosses the x-axis.

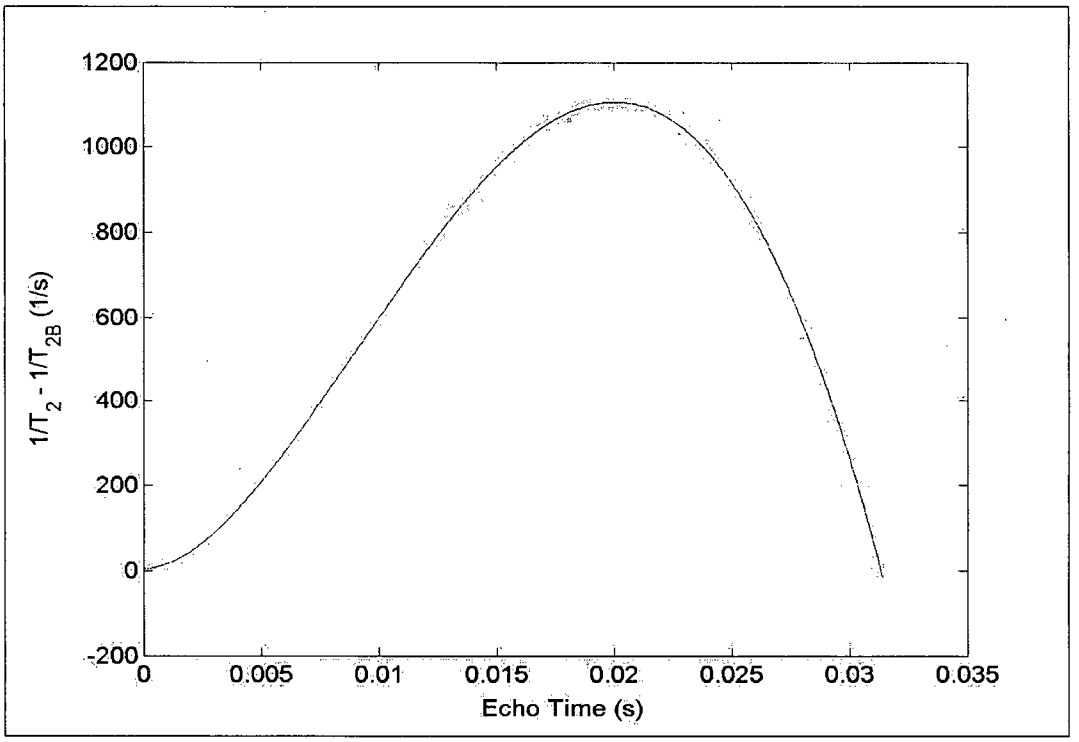

Figure 3.2 – Shape of the forward model for the parameter values $\rho_2=1.0\times10^{-3}$ cm/s, $S/V=4.7\times10^{3}$ 1/cm and $G=1.0\times10^{-2}$ T/cm over a large range of echo times.

Physically, this last case represents the point at which the $1/T_2$ is equal to the $1/T_{2B}$. This is the limiting case, as the relaxation time of the fluid in a pore space cannot be larger than the relaxation time of the bulk fluid.

In summary, close inspection of the forward model suggests there may be some issues in the interpretation of the T_2 data depending on the magnitudes of the parameters. It has been shown that increasing the echo time may help increase the influence of the third term on the data in order to resolve ρ_2 and S/V, however caution must be exercised, as the short time approximation of the forward model may become invalid at longer echo times.

3.3 - MATERIALS AND METHODS

3.3.1 - Nuclear Magnetic Resonance T_2 Measurements

NMR T_2 relaxation times were measured on the same hematite samples as those discussed in Chapter 2. For reference, mixtures of 2.1, 3, 6, 9, 12, 30 and 60 percent hematite by weight were used. T_2 and T_{2B} were measured at a 90 MHz Larmor frequency, which corresponds to a 2.2 T magnetic field strength. A CPMG sequence was used to collect the T_2 data, which partially removed the effects of the internal magnetic field gradients. Data were collected at echo times of 0.2, 0.3, 0.4, 0.5, 0.6 and 0.8 ms. As a result, only six data were obtained for each hematite sample, which will be an issue when applying statistical analyses to the results. This will be discussed further in the following section. The T_2 exponential relaxation data underwent a linear non-negative least squares (NNLS) regularized inversion to obtain the T_2 distributions. This inversion fits the multiexponential decay curve using a number of single exponentials. Specifically, a set of amplitudes, s_j, were solved for 160 single exponentially spaced T_{2j} values and the forward model is:

$$Data = y(t_i) = \sum_{j=1}^{M} s_j \exp\left(-\frac{t_i}{T_{2j}}\right) \tag{3.7}$$

There were 750 T_2 data points collected. The objective function that was minimized in this inversion was:

$$\phi_m = \sum_{i=1}^{N} \left\| \sum_{j=1}^{M} A_{ij} s_j - y_i \right\|^2 + \mu \sum_{j=1}^{M} s_j^2 \tag{3.8}$$

where A_{ij} is:

$$A_{ij} = \exp\left(-\frac{t_i}{T_{2j}}\right) \tag{3.9}$$

Each datum and corresponding row of **A** was normalized by the standard deviation of the noise. μ is the trade off parameter that describes how well the algorithm fits the data over the additional constraints. This algorithm fitted the data and also minimized the energy of the spectrum. In other words, the inversion fitted the data subject to the smallest model (Whittall and MacKay, 1989).

Unlike the T_1 data, the T_2 distribution was multi-modal. The logmean of the entire T_2 distribution was used as the T_2 value for the inversion discussed in this thesis. The multiple peaks are believed to be the influence of the effective internal gradients as opposed to several pore sizes, as the T_1 distributions for the same samples were monomodal. Figure 3.3 is a typical T_2 distribution for a 30% hematite sample measured at an echo time of 0.2 ms. The peaks at either edge of the spectrum are artifacts.

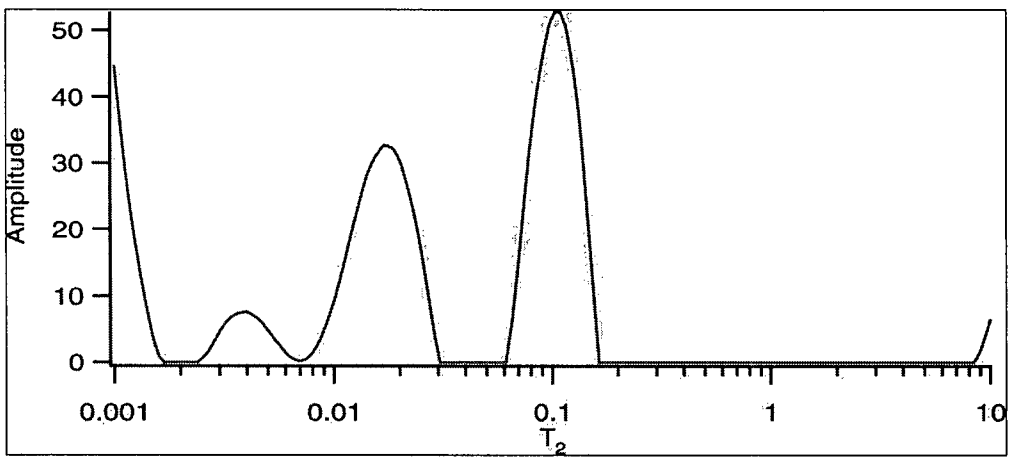

Figure 3.3 – Typical T_2 distribution for a 30% hematite by weight sample in quartz. Illustrates the multimodal characteristics of the distribution.

The error for each T_2 value was calculated by comparing the logmean value of the NNLS inversion with the logmean of the T_2 distribution that resulted from a least distance inversion completed on the same data. This second inversion minimized the objective function:

$$\phi_m = \sum_{i=1}^{N} \left| \sum_{j=1}^{M} A_{ij} s_j - y_i \right| + \mu \sum_{j=1}^{M-2} \left| s_{j+2} - 2s_{j+1} + s_j \right| \tag{3.10}$$

The absolute value of the misfit is minimized subject to minimizing the energy of the curvature of the spectrum (Whittall and MacKay, 1989). Calculating and comparing the logmean values for the resulting T_2 distributions from each inversion provided an estimate of the error associated with the inversion technique. This was deemed an appropriate error for the T_2 data.

The T_{2B} term was also calculated. The relaxation decay curve for the bulk water was fit to a single exponential with the time constant T_{2B}, as bulk water would be expected to decay with a single exponential. The error associated with this fit was used as the error for T_{2B}.

The data for this inversion were:

$$\frac{1}{T_2} - \frac{1}{T_{2B}}$$

and the total error on this data were calculated from the error on each relaxation time using Gauss' equations presented in equations 2.5, 2.6 and 2.7.

3.3.2 - Inversion

3.3.2.1 - The Newton Method of Minimization

The Newton method of local minimization is used to find the local minimum of a continuous function from a given starting point. The function to be minimized is called the misfit objective function, or simply the misfit, which is a measure of the difference between the measured data and the predicted data at a set of parameters or model (**m**). Specifically:

$$\phi_d(\mathbf{m}) = \frac{1}{2}\left\|\mathbf{W}_d(\mathbf{d}^{obs} - \mathbf{F}[\mathbf{m}])\right\|^2 \tag{3.11}$$

where $\mathbf{W}_d$ is a diagonal matrix of the inverse of the error associated with the each data point. The $\mathbf{d}_{obs}$ term is a vector containing the measured data at each echo time and the $\mathbf{F}[\mathbf{m}]$ term is a vector of the data predicted for each echo time, given a set of model parameters. The predicted data were calculated using the forward model for this problem, shown in equation 3.6. An L2 norm was used as opposed to an L1, as it penalizes large differences between the observed data and the predicted data.

To understand how the Newton method proceeds, one must first recognize that any non-linear function with r continuous derivatives can be approximated by a Taylor expansion (Garcia, 1994). In the case of a function of a single variable (m), the expansion around m_o is:

$$f(m_o + \partial m) = f(m_o) + f'(m_o)\partial m + \frac{1}{2}f''(m_o)\partial m^2 + \ldots + \frac{1}{r!}f^{(r)}(m_o)\partial m^r \tag{3.12}$$

The Newton method approximates non-linear functions as quadratics and equation 3.12 is estimated as:

$$\hat{f}(m_o + \partial m) = f(m_o) + f'(m_o)\partial m + \frac{1}{2} f''(m_o)\partial m^2 \tag{3.13}$$

Setting the first derivative of equation 3.13 with respect to ∂m to zero, will solve for ∂m at the minimum of $\hat{f}$. This procedure is repeated until the gradient of the function, f(m) is zero.

Convergence to a minimum will occur as long as it is ensured that each successive model is 'downhill' from the previous model or:

$$f[m_{i+1}] < f[m_i] \tag{3.14}$$

where m_i is the model at the i^{th} iteration. Figure 3.4 is a graphical representation of a single iteration for a function f(m) in one dimension. In the diagram, the function f(m) at m_i is approximated as a quadratic $\hat{f}$(m), ∂m_i is calculated, taken as the step length and the function is then evaluated at m_{i+1}.

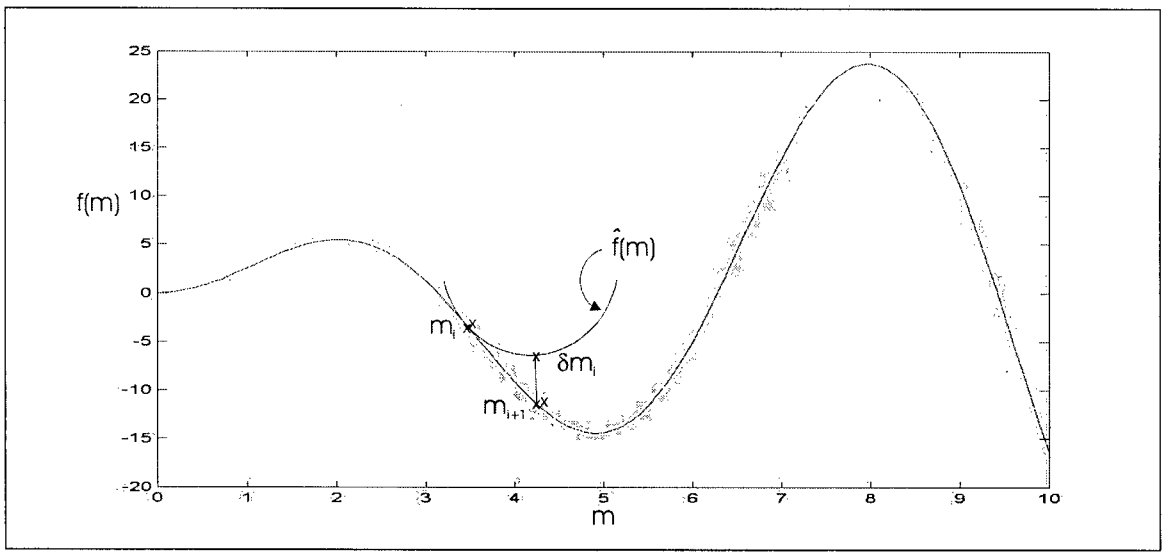

Figure 3.4 – Newton step in one dimension.

For multivariate functions such as our objective function $\phi(\mathbf{m})$ of equation 3.11, the same procedure is completed, it is just not as easy to visualize. The objective function is a non-linear function of three variables. Using the Taylor expansion, the quadratic approximation of ϕ is:

$$\tilde{\phi}(\mathbf{m}_i + \partial\mathbf{m}) = \phi(\mathbf{m}_i) + \nabla\phi(\mathbf{m}_i)^T \partial\mathbf{m} + \frac{1}{2}(\partial\mathbf{m})^T \nabla^2\phi(\mathbf{m}_i)\partial\mathbf{m} \tag{3.15}$$

(Garcia, 1994). $\partial\mathbf{m}$ is determined by computing the gradient of $\tilde{\phi}$ with respect to $\partial\mathbf{m}$, and setting it to zero. The equation to be solved is then:

$$\nabla\phi(\mathbf{m}_i) + \nabla^2\phi(\mathbf{m}_i)\partial\mathbf{m} = 0 \tag{3.16}$$

For ease of notation, the gradient of $\phi(\mathbf{m})$ is expressed as $\mathbf{g}$ and the second derivative of $\phi(\mathbf{m})$, which is known as the Hessian matrix, is denoted as $\mathbf{H}$.

The gradient at a given set of model parameters is calculated by:

$$\mathbf{g} = -\mathbf{J}^T \mathbf{W}_d^T \mathbf{W}_d (\mathbf{d}^{obs} - \mathbf{F}[\mathbf{m}]) \tag{3.17}$$

where $\mathbf{J}$ is the Jacobian sensitivity matrix, which is a measure of the sensitivity of the j^{th} predicted data point ($F_j[m]$) with respect to the k^{th} model parameter (m_k) and is calculated as:

$$\mathbf{J}_{jk} = \frac{\partial F_j[m]}{\partial m_k} \tag{3.18}$$

The Hessian is computed using the Jacobian sensitivity matrix, the error matrix and another matrix called $\mathbf{Q}$:

$$\mathbf{H} = \mathbf{J}^T \mathbf{W}_d^T \mathbf{W}_d \mathbf{J} + \mathbf{Q} \tag{3.19}$$

where **Q** is:

$$\mathbf{Q}_{kl} = -\sum_{j=1}^{N}(d_j^{obs} - F_j[m])\frac{\partial^2 F_j[m]}{\partial m_k \partial m_l} \tag{3.20}$$

which defines the second derivative of the j^{th} data point with respect to the k^{th} and l^{th} model parameter and sums over all the data points.

It is the Hessian matrix that is inverted to solve for $\partial\mathbf{m}$. The expression at each iteration is:

$$\partial\mathbf{m} = -\mathbf{H}(\mathbf{m}_i)^{-1}\,\mathbf{g}(\mathbf{m}_i) \tag{3.21}$$

This equation is equivalent to equation 3.16. $\partial\mathbf{m}$ points to a local minimum if the Hessian matrix is positive definite or equivalently, all of the eigenvalues of the matrix are positive. If some of the eigenvalues are negative, $\partial\mathbf{m}$ may still be in a descent direction and this can be confirmed if the following inequality is met:

$$\mathbf{g}(\mathbf{m}_i)^T\,\partial\mathbf{m} < 0 \tag{3.22}$$

Alternatively, an approach discussed in Bard (1974) can be implemented. At each iteration the absolute value of the eigenvalues can be taken by decomposing the Hessian such that:

$$\mathbf{H} = \mathbf{U}\Lambda\mathbf{U}^T \tag{3.23}$$

(Strang, 1988), where **U** is a matrix containing the eigenvectors and Λ is a diagonal matrix where Λ_{ii} is the i^{th} eigenvalue. The absolute value of Λ is computed and the Hessian is reconstructed with the positive eigenvalues and is now positive definite, which ensures a descent direction. This was the procedure used in this inversion.

Referring to figure 3.4, $\partial\mathbf{m}$ minimizes the quadratic approximation of the objective function, not the actual function. We know that $\partial\mathbf{m}$ points in a descent

direction and a line search is required to locate a local minimum of the objective function, a procedure not shown in figure 3.4. The line search investigates the objective function in the direction of $\phi(\mathbf{m} + \varepsilon\partial\mathbf{m})$ until it finds the value of ε, known as the step length, where the gradient is zero. The step length has an upper limit of 1, corresponding to the magnitude of $\partial\mathbf{m}$. Upon recovering ε, a new set of model parameters ($\mathbf{m}_{i+1}$) are calculated by:

$$\mathbf{m}_{i+1} = \mathbf{m}_i + \varepsilon\,\partial\mathbf{m} \tag{3.24}$$

The objective function is calculated at $\mathbf{m}_{i+1}$ and the entire procedure repeats.

The algorithm will continue until the stopping criterion is met. Since the goal is to find a local minimum of the objective function, when the gradient of the misfit is very close to zero (1.0×10^{-5}) indicating a local minimum has been located, the inversion will cease (Bard, 1974).

The preceding description describes the Newton method for local minimization and it is the basis for the inversion used to obtain the unknown parameters in the forward model of equation 3.6. Certain aspects of the method can be improved to increase the accuracy of the results and the speed of the convergence. In addition some features of the code and the parameters require further explanation and justification. Each of the features discussed below were incorporated into the algorithm used for this problem.

3.3.2.2 - Features of the Code

Scaling the Model Parameters

In many cases, the parameter values to be solved differ in size by several orders of magnitude. This may cause difficulties in the convergence of the algorithm, as the step length in one direction of the model space may be much larger than in other directions

and will consequently be favored. One solution to this problem is to scale the model parameters by the expected value of each parameter, which is achieved by constructing a diagonal matrix **M** such that:

$$(\mathbf{M})_{ij} = \frac{1}{m_i^{expected}} \quad where\ i = j \tag{3.25}$$

and the scaled model values are defined as:

$$\tilde{\mathbf{m}}_{scaled} = \mathbf{Mm} \tag{3.26}$$

The algorithm solves for the scaled values, which are then transformed back upon completion of the inversion. Implementing such a transformation may also result in a better-conditioned Hessian matrix if the parameters differ by many orders of magnitude, which was the case for this inversion.

Regularization

The condition number of a matrix is the ratio of the maximum eigenvalue to the minimum eigenvalue. If this number is very large, the matrix will approach singularity and will be difficult to invert. In the event of the Hessian having a condition number larger than the working precision of the computer, a small value is added to the diagonal, which reduces this number. This may change the search direction, but it will remain a descent direction. The path of the solution may be altered but not the solution itself.

Bounds on the parameters

The surface relaxivity, surface area to volume ratio and internal gradient are positive quantities. Accordingly, a constraint of positivity was placed on each parameter. This is accomplished by defining a new starting model such that:

$$\mathbf{m}_i = \tilde{\mathbf{m}}_i^2 \tag{3.27}$$

(Beveridge and Schechter, 1970) and the algorithm minimizes the objective function $\phi(\tilde{\mathbf{m}})$. The solution model $\tilde{\mathbf{m}}_{solution}$ is then transformed to $\mathbf{m}_{solution}$.

Upper bounds on each parameter may also be known, although imposing them in the minimization code can result in the algorithm stalling on a boundary. As a result, upper bounds were not incorporated into this inversion. However, if a successful solution included a parameter value that was unrealistic based on knowledge of its upper bound, the solution was discarded.

Random Starting Model Generation

Depending on the shape of the objective function, a solution found using the Newton method could depend on the starting model. There are two techniques that can be implemented to obtain a more reliable result. The first is to select a starting model that is a best guess of the solution model. Assuming the starting model is a good approximation, the algorithm will converge to the proper solution. Quite often, values for each parameter cannot be accurately estimated and the only a-priori information available is some knowledge of the range of model values. In this case, many random starting models are generated within the specified bounds and the inversion is completed for each. If a minimum for a particular starting model is not found, the solution is rejected. Otherwise, the solution is accepted and the inversion for the next model begins.

3.4 - RESULTS AND DISCUSSION

3.4.1 - Synthetic Data Results and Algorithm Validation

Prior to using this method to solve for the surface relaxivity, surface area to volume ratio and the internal gradient for the hematite samples, the accuracy and

shortcomings of the algorithm must be evaluated to provide some idea of the reliability of the solutions. This is achieved by creating a synthetic data set, in which the data are generated using a set of known parameters and adding Gaussian noise. The algorithm was evaluated based on its ability to solve for these known parameters.

As an aside, in the following discussion, there are two completely separate parameters that are known as the gradient. To minimize confusion, the unknown parameter G, for which we are attempting to solve, will be called the internal gradient or G. The gradient of the objective function will be called the gradient.

For reference, the maximum values of each parameter will first be discussed to aid in evaluating the validity of the solution models. The surface relaxivities in this section will be reported in cm/s rather than μm/s which were the units used in Chapter 2. Although the units of μm/s are somewhat easier to discuss as the T_2 surface relaxivity of rocks will be on the order of 1 μm/s to 10 μm/s, cm/s were used to maintain dimensional consistency with the other two parameters discussed at length in this chapter. The surface relaxivity is not expected to exceed 3.0×10^{-2} cm/s, as the highest literature value of surface relaxivity for T_2 measurements is 1.9×10^{-2} cm/s (Roberts et al., 1995). This value was measured at 0.7 T field strength, while the data collected for this inversion were measured at a field strength of 2.12 T. In Chapter 2, it was shown that increasing the field strength will decrease the surface relaxivity. An upper bound of 3.0×10^{-2} cm/s should therefore be much larger than would be expected for most rocks and sediments.

The maximum value anticipated for the surface area to volume ratio for any geological sample is 2.2×10^{6} 1/cm. This corresponds to the S/V for silica gel, which is understood to be an order of magnitude larger than a pure clay sample. Most sediments

composed of fine sand will have values of around 3.0×10^{3} 1/cm, however, in an effort to not bias the solution for a wide variety of rock types, a very high upper bound is appropriate.

A practical upper bound for the internal gradient is approximately 45 T/cm. Hurlimann (1998), showed that at a field strength of 5.5×10^{-2} T, an internal gradient of 1 T/cm was possible for rocks with very high susceptibility differences. Since the data for this inversion were collected at 2.12 T field strength which is 40 times greater than 5.5×10^{-2} T, the internal gradient could presumably be about 40 times larger than 1 T/cm according to equation 1.7. The maximum G was consequently set at 45 T/cm.

A synthetic data set was generated using equation 3.6 and the parameter values of $\rho_2=1.0\times10^{-3}$ cm/s, $S/V=4.7\times10^{3}$ 1/cm and $G=1\times10^{-2}$ T/cm. The data were polluted with 7% Gaussian noise. For a given realization of the noise, figure 3.5 shows a plot of the data versus the echo time for the six echo times used to measure T_2 on the hematite data. The trend line indicates the values for the exact data.

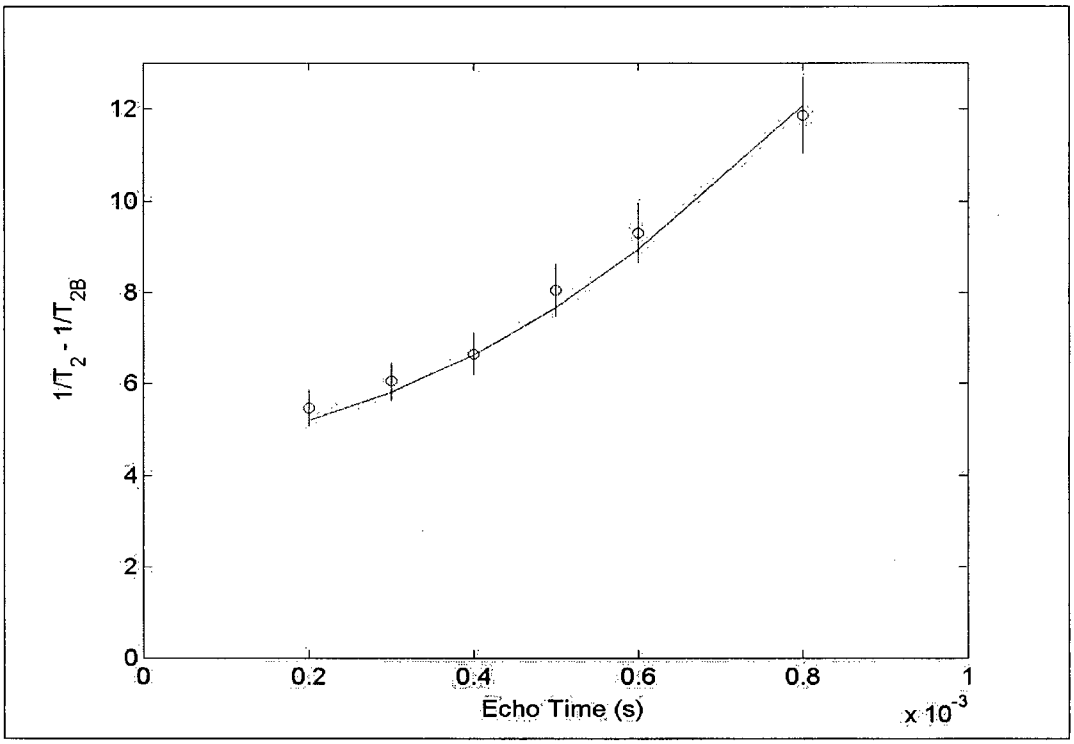

Figure 3.5 – The data (circles) versus the echo time for the synthetic data polluted with 7% noise at the parameter values ρ_2=1.0×10^{-3} cm/s, S/V=4.7×10^3 1/cm and G=1×10^{-2} T/cm. The line shows the values for the exact data.

Initially, analysis of solutions for the exact synthetic data and the noisy synthetic data, from a single starting model, will assess the accuracy of the algorithm. Next, to ascertain the dependence of the solution on the starting point, the inversion will be completed on the same synthetic data set from several starting models.

3.4.1.1 - Solution From a Single Starting Point

Figure 3.6 shows the value of the objective function for a range of values of the surface relaxivity and the surface area to volume ratio. This type of plot is also known as the objective function surface or the misfit surface. In this figure, the synthetic data were generated without noise and as a result the true model solution was obtained regardless of the starting point. Figure 3.6-A is the solution trajectory in the two dimensions of ρ_2 and S/V from a distant starting model of ρ_2=1.0×10^{-2} cm/s, S/V=5.0×10^4 1/cm and

$G=1.0\times10^{-1}$ T/cm and figure 3.6-B shows the path of solution near the true solution which again was $\rho_2=1.0\times10^{-3}$ cm/s, $S/V=4.7\times10^{3}$ 1/cm and $G=1.0\times10^{-2}$ T/cm. In computing the objective function surface, the internal gradient was held constant at 1.0×10^{-2} T/cm. The values of the misfit surface on the plot are the logarithm to the base ten of the misfit, which was observed to vary over several orders of magnitude for the range of S/V and ρ_2 values shown. Figure 3.7-A is the solution trajectory for the exact data for the surface relaxivity and the internal gradient, while figure 3.7-B illustrates the solution path for the surface area to volume ratio and the internal gradient.

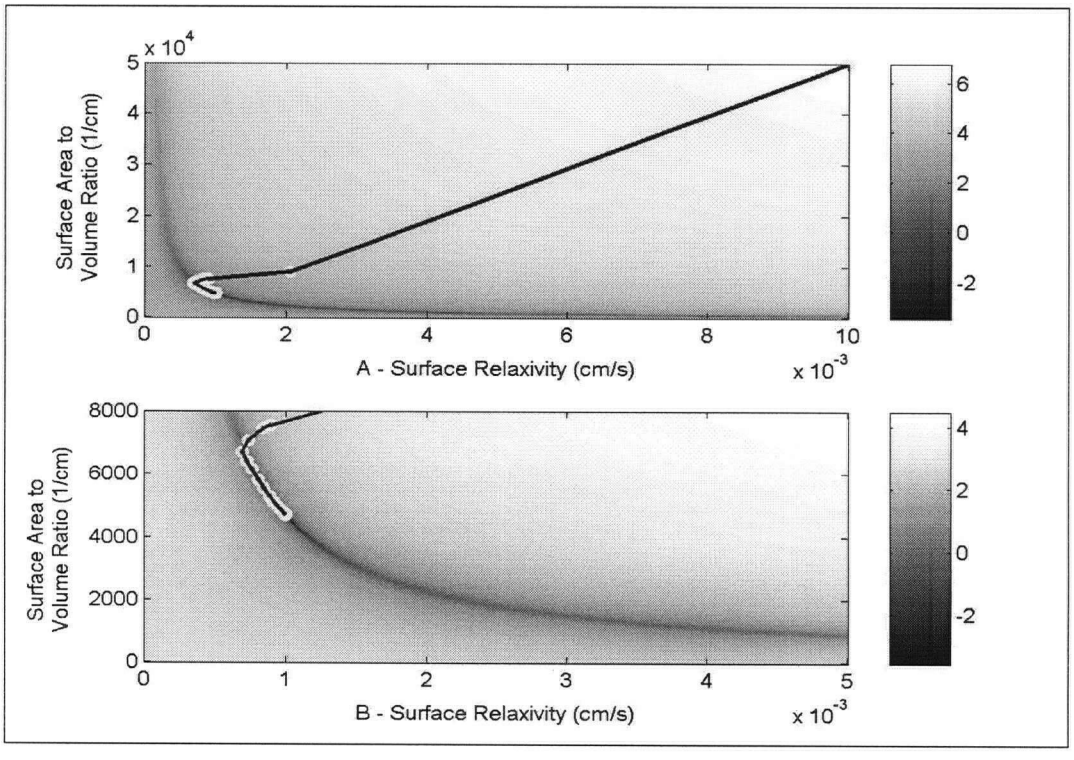

Figure 3.6 – Misfit surface for S/V and ρ_2 showing the trajectory of the solution for exact data. Figure 3.6-A shows the entire solution path, while 3.6-B shows the trajectory near the minimum. For plotting, a constant internal gradient of 1.0×10^{-2} T/cm was maintained.

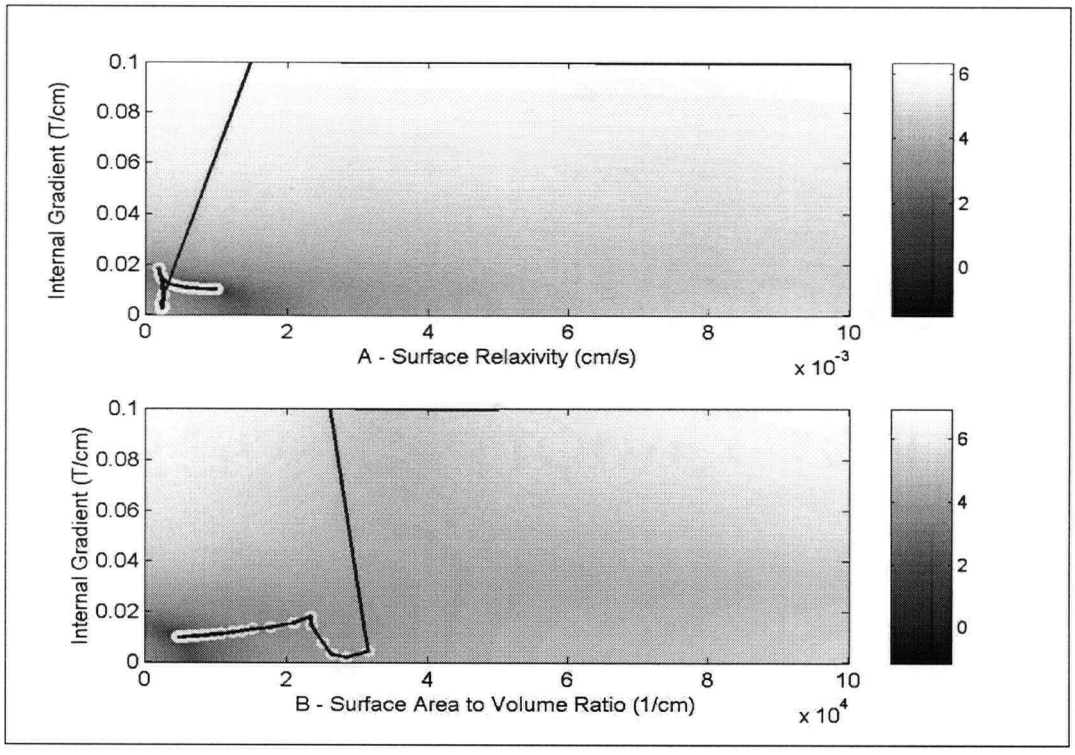

Figure 3.7 – Misfit surfaces for G and ρ_2 and G and S/V showing the trajectory of the solution of the exact data. In figure 3.7-A, the surface area to volume ratio was held constant at 4.7×10^3 1/cm for plotting and in figure 3.7-B, the surface relaxivity was held constant at 1.0×10^{-3} cm/s for plotting.

In most solutions, even those with a large error, the internal gradient was very stable. Hence for the sake of brevity, future plots will show only the trajectory of the solution for the surface relaxivity and the surface area to volume ratio.

The next step in evaluating the algorithm is to test its performance in minimizing data with incorporated noise. A brief discussion about expected values of misfit is initially required to aid in evaluating the recovered models.

Determining a value for the misfit that represents an appropriate fit to data that are polluted with noise is difficult when there are only six data points. Recall that the objective function is essentially the following:

$$\phi_d = \sum_{i=1}^{N} \left(\frac{d_i^{obs} - d_i^{true}}{\varepsilon_i} \right)^2 \tag{3.28}$$

This expression is equivalent to the χ^2 statistic. If each observed datum varies from the predicted datum by the stated error, the misfit should be equal to N, the number of data, which in this case are 6. With the small number of data used in this inversion, the usefulness of the χ^2 statistic is limited, but it is an appropriate guideline. We will assume that a misfit of approximately 6 represents a suitable fit between the observed and predicted data for both the synthetic data and the hematite data.

Figure 3.8 shows the trajectory of the solution for data polluted by 7% Gaussian noise from a starting point of $\rho_2=1.0\times10^{-2}$ cm/s, $S/V=5.0\times10^{4}$ 1/cm and $G=1.0\times10^{-1}$ T/cm. A solution model of $\rho_2=5.0\times10^{-4}$ cm/s +/- 5.0×10^{-7}, $S/V=9.7\times10^{3}$ +/- 9.6 1/cm and $G=9.4\times10^{-3}$ +/- 3.5×10^{-6} T/cm was recovered which had a misfit of 1.5.

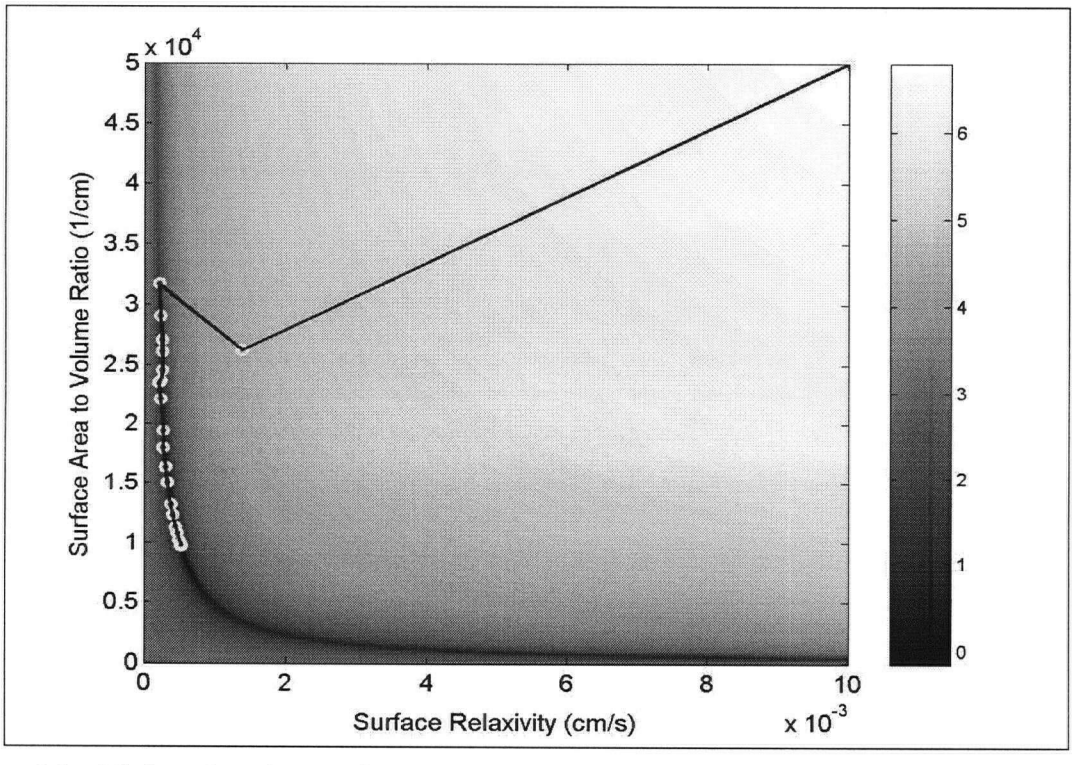

Figure 3.8 – Misfit surface showing the trajectory of the solution for synthetic data polluted with 7% noise. For plotting, the gradient was held constant at 1.0×10^{-2} T/cm.

The slightly erratic path of the solution in the first couple of steps was a result of change in the internal gradient. The discrepancy between the solution model and the true solution is a result of the path of the solution coupled with the noise realization. The solution trajectory encountered an area of very small misfit gradient and the algorithm terminated prematurely. The misfit value of 1.5 is smaller than the expected value of 6, but nonetheless represents a valid solution.

Error for each parameter value was calculated by generating a model covariance matrix:

$$[\text{cov } \mathbf{m}] = \mathbf{L}[\text{cov } \mathbf{d}]\mathbf{L}^T \tag{3.29}$$

where [covd] is the data covariance matrix:

$$[\text{cov } \mathbf{d}] = [\mathbf{W}_d{}^T \mathbf{W}_d]^{-1} \tag{3.30}$$

and L is the operator:

$$(\mathbf{J}^T \mathbf{W}_d{}^T \mathbf{W}_d \mathbf{J} + \mathbf{Q})^{-1} \mathbf{J}^T \mathbf{W}_d{}^T \mathbf{W}_d \tag{3.31}$$

J and **Q** in each case were calculated using the solution parameter values (Menke, 1984). The error on each model parameter was approximated as the diagonal values of the model covariance matrix, corresponding to the variance of the error of that parameter with respect to itself. The off-diagonal entries corresponding to the covariance between parameters were ignored. Finding the error on the model parameters in this manner can be misleading, as it assumes the only error associated with the inversion is that introduced through the observed data. As a result, the calculated errors may be smaller than are realistic.

Next, the dependence of the solution on the realization of the noise is examined. The algorithm was run from the same starting point of ρ_2=1.0×10^{-2} cm/s, S/V=5.0×10^4

1/cm and $G=1.0\times10^{-1}$ T/cm for several realizations of 7% noise. Table 3.1 shows the solution models recovered for ten sets of data, each with a different noise manifestation.

The data in table 3.1 convey several important attributes of the algorithm and the forward model. Solution models three and seven converged with extremely inaccurate values. This dependence of obtaining an accurate solution based on the realization of the noise is unfortunate, as with real data we have no control on how the noise may manifest.

The other solution models had values that were closer to the true solution. Many of the solutions exhibited a similar phenomenon illustrated in figure 3.8. The solution trajectory encountered a region in the misfit surface that had a very small gradient, before reaching the true solution. ρ_2 and S/V in each solution are quite variable. In every case however, the recovered internal gradient was very close to the true internal gradient despite the vast variation in the other two parameters. The internal gradient values varied from 8.9×10^{-3} T/cm to 1.3×10^{-2} T/cm.

Solution Model	ρ_2 ($\times10^{-4}$ cm/s) True value = 10	S/V ($\times10^{3}$ 1/cm) True Value = 4.7	G ($\times10^{-3}$ T/cm) True Value = 10
1	13 +/- 0.0020	4.1 +/- 0.00057	8.9 +/- 0.0047
2	3.0 +/- 0.0024	14 +/- 0.0059	13 +/- 0.0038
3	29000 +/- 270000	0.0015 +/- 0.014	9.5 +/- 0.0014
4	4.1 +/- 0.017	12 +/- 0.04	11 +/- 0.0093
5	5.7 +/- 0.12	8.2 +/- 0.16	11 +/- 0.011
6	2.7 +/- 0.0027	16 +/- 0.0032	13 +/- 0.0089
7	22000 +/- 160000	0.0022 +/- 0.0090	9.0 +/- 0.0047
8	6.2 +/- 0.0021	7.1 +/- 0.0018	11 +/- 0.0028
9	17 +/- 0.0032	2.8 +/- 0.00048	9.3 +/- 0.0043
10	8.6 +/- 0.0043	5.9 +/- 0.0026	9.7 +/- 0.0048

Table 3.1 – Solution model values for 10 different realizations of 7% noise. The same starting model was used for each: $\rho_2=1.0\times10^{-2}$ cm/s, $S/V=5.0\times10^{4}$ 1/cm and $G=1.0\times10^{-1}$ T/cm.

Taking a closer look at the solutions for ρ_2 and S/V in table 3.1, the product of the two parameters were well constrained for each noise realization, including the two extremely erroneous solutions. The product at the true minimum is 4.7/s and the products of the inverted solutions ranged from 4.0/s to 5.5/s. The algorithm for this particular set of synthetic data can solve for the internal gradient and the product of the surface relaxivity and the surface area to volume ratio very well, but the actual estimated quantities for ρ_2 and S/V may vary significantly.

This last observation can be explained by investigating the variation in the three terms of equation 3.6 for the synthetic data. Table 3.2 shows the value of each term at the true minimum of $\rho_2=1.0\times10^{-3}$ cm/s, $S/V=4.7\times10^{3}$ 1/cm and $G=1.0\times10^{-2}$ T/cm.

At the solution, term 3 is an order of magnitude smaller than term 2 and in most cases the noise in the data is larger than the value of the third term. As a result, very little information contained in term 3 is used to find a solution for the three parameters. Consequently, only the product of ρ_2 and S/V can be resolved well, along with the value of the internal gradient.

Echo Time (ms)	Data (1/s)	Error (1/s)	Term 1	Term 2	Term 3
0.2	5.2	0.36	4.7	0.55	0.044
0.3	5.8	0.41	4.7	1.2	0.12
0.4	6.6	0.46	4.7	2.2	0.25
0.5	7.7	0.54	4.7	3.4	0.43
0.6	9.0	0.63	4.7	4.9	0.68
0.8	12	0.84	4.7	8.8	1.4

Table 3.2 – Relative sizes of each term in equation 3.6 compared to the value of the data and the error in the data for the synthetic data set.

The data points at 0.6 ms and 0.8 ms do contain some information about the S/V, as term 3 is slightly larger than the noise. These data may place some constraint on the possible values of ρ_2 and S/V. For example, in all of the solutions shown in table 3.1, the S/V appears to have a maximum value that may not exceed 2.0×10^4 and ρ_2 appears to have a minimum value of approximately 2.0×10^{-4}.

As mentioned earlier, a potential solution to the inability to distinguish ρ_2 and S/V would be to lengthen the echo times, which would increase the size of terms 2 and 3 and help constrain the individual values of ρ_2 and S/V. This would have to be undertaken with care as to ensure the short time approximation for the diffusion coefficient was not invalidated.

3.4.1.2 - Solution Starting at Several Starting Points

In order to sample the model space thoroughly and to gain a better understanding of the solution dependence on the starting model, 100 random starting points were generated by the algorithm within the upper and lower bounds for each parameter. The inversion was then carried out for each. All solutions in which a zero gradient in the misfit was not found were rejected. Also rejected, were solutions in which one or more parameters exceeded the estimated bounds and solutions in which the misfit was much larger than the expected value of 6.

For a single realization of 7% noise in the synthetic data, only one acceptable solution model was recovered. This solution model was obtained from approximately 85 of the 100 starting points. The inversions from the other 15 starting points returned solution models that were unacceptable based on the criteria discussed above. The valid solution model had parameter values of $\rho_2=5.0\times10^{-4}$ cm/s, $S/V=7.7\times10^3$ 1/cm and

$G=1.2\times10^{-2}$ T/cm with a misfit of 1.9. These results indicate the solution model is not largely dependent on the starting point and most starting points will converge to an identical solution for a given realization of noise and model parameters.

In summary, the synthetic data results show that separating ρ_2 and S/V may be difficult. The relative sizes of the terms in the forward model are crucial in resolving the S/V from ρ_2. The values of the forward model terms will vary with the magnitudes of the parameters and the range of echo times used. According to the synthetic data results, G and the product of ρ_2 and S/V can be reliably obtained for all noise realizations.

3.4.2 - Hematite Data Results

The algorithm was applied to the T_2 relaxation data for the hematite samples, which ranged from 2.1% to 60% by weight of hematite. For each sample, the algorithm was run from 100 random starting models. Similar to the synthetic data, the algorithm recovered one acceptable solution model for each hematite sample and a few unacceptable models.

As an example, let us consider the inversion for a 6% hematite mixture. Of the 100 starting points, 95 of the solution models were identical, with parameter values of $\rho_2=8.9\times10^{-5}$ cm/s, $S/V=2.5\times10^{4}$ 1/cm and $G=1.9\times10^{-2}$ T/cm. The misfit of this solution model was 0.4 and is small compared to the expected misfit of 6. Table 3.3 shows the data and the error for this sample, along with the sizes of each of the terms of the forward model computed using the above solution parameters. The error is close to 10% for most of the data. This could be an overestimate of the true error, which would result in a smaller misfit than expected. In any case, this solution model is believed to represent a valid solution model for the data as the χ^2 statistic is once again simply an estimate.

Echo Time (ms)	Data (1/s)	Error (1/s)	Term 1	Term2	Term 3
0.2	3.3	0.20	2.2	2.0	0.82
0.3	4.8	0.55	2.2	4.5	2.3
0.4	5.2	0.51	2.2	7.9	4.7
0.5	6.3	0.70	2.2	12	8.2
0.6	7.2	0.44	2.2	17	13
0.8	7.4	0.13	2.2	32	27

Table 3.3 – Relative sizes of each term in equation 3.6 compared to the value of the data and the error in the data for a 6% hematite sample.

The other 5 solution models for this 6% hematite sample had very large misfits and the internal gradient values were on the order of 1×10^{-10}. This extremely low internal gradient indicates the second and third terms of forward model were essentially zero and a solution was recovered that represented the data at each echo time as a constant. Figures 3.1, 3.2 and 3.5 show that approximating the data in such a manner is completely inaccurate. The large misfits and incorrect representation of the data signify these alternate solution models are unacceptable.

Table 3.3 also shows that for the valid solution parameters, each term in the forward model is of similar magnitude. This suggests the specific values for the surface relaxivity and the surface area to volume ratio may be more reliable than those resulting from the synthetic data, in which the third term was very small.

Figure 3.9 shows the data collected for this 6% hematite sample, shown as the circles, along with the fit to the data by the forward model at the solution parameters, illustrated as the line. This figure illustrates the good match between the observed data and the predicted data at the solution parameters.

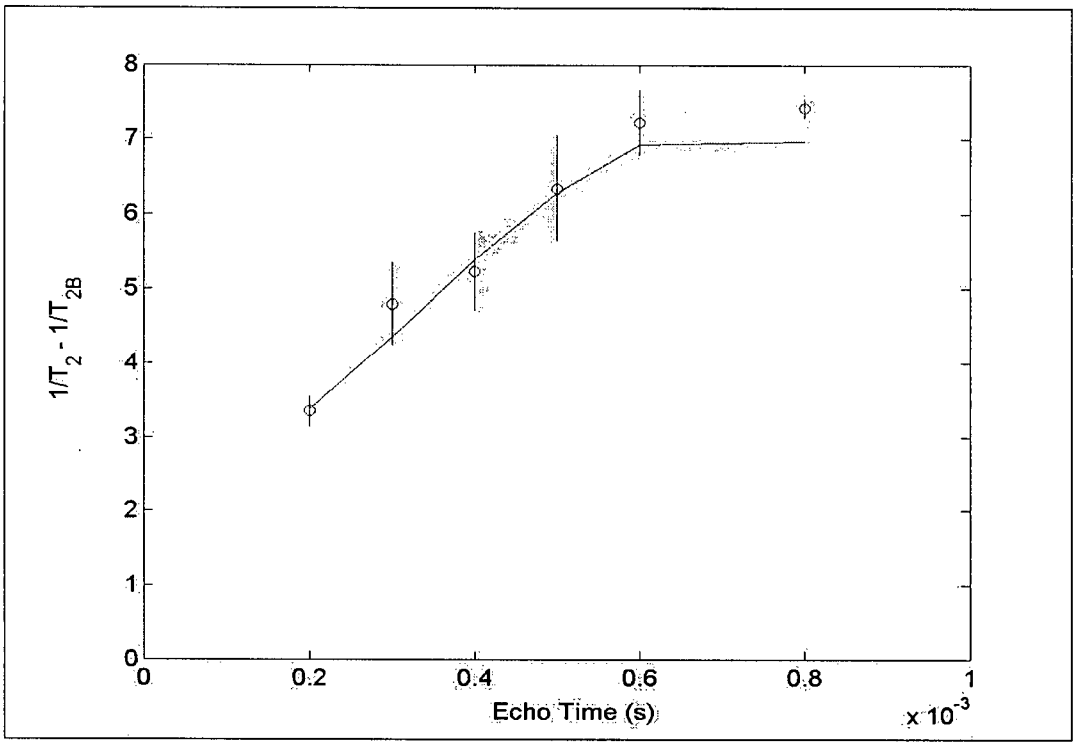

Figure 3.9 – The real data for a 6% hematite sample (circles) along with the fit to data by the forward model (line) at the solution parameters ρ_2=8.9×10^{-5} cm/s, S/V=2.5×10^4 1/cm and G=1.9×10^{-2} T/cm.

Each hematite sample returned similar results, in that most of the solutions from the randomly chosen starting points were identical and had a low misfit value, while the remaining solution models were invalid. The inversion therefore returned a single reliable solution for every hematite mixture, which was used for analysis and discussion.

Table 3.4 shows the inverted parameter values for each of the parameters for each of the hematite mixtures, along with the misfit values.

Sample Amount of Hematite	S/V ($\times 10^4$ 1/cm)	ρ_2 ($\times 10^{-4}$ cm/s)	G ($\times 10^{-2}$ T/cm)	Misfit
2.1%	1.2 +/- 0.00017	0.86 +/- 0.00019	0.57 +/- 0.00008	2.3
2.1%	2.4 +/- 0.0071	0.47 +/- 0.0035	0.78 +/- 0.0040	0.089
2.1%	1.1 +/- 0.017	1.4 +/- 0.027	0.51 +/- 0.0011	0.36
3%	2.3 +/- 0.0017	0.76 +/- 0.0018	1.1 +/- 0.0020	2.9
3%	1.8 +/- 0.087	1.4 +/- 0.080	0.78 +/- 0.020	0.32
6%	2.5 +/- 0.00024	0.89 +/- 0.0054	1.9 +/- 0.0024	0.4
6%	2.1 +/- 0.0019	2.0 +/- 0.030	1.4 +/- 0.0019	0.62
6%	1.2 +/- 0.0010	3.8 +/- 0.0068	0.99 +/- 0.0079	0.43
9%	2.6 +/- 0.00010	1.4 +/- 0.0033	2.8 +/- 0.0060	20
9%	2.1 +/- 0.0012	2.3 +/- 0.0028	1.7 +/- 0.0015	1.6
9%	2.0 +/- 0.0049	2.9 +/- 0.015	1.9 +/- 0.0052	0.29
12%	2.2 +/- 0.0012	2.9 +/- 0.0097	2.4 +/- 0.0028	0.63
12%	2.1 +/- 0.0013	3.2 +/- 0.0062	2.3 +/- 0.0019	4.6
30%	2.5 +/- 0.0018	0.61 +/- 0.73	7.7 +/- 0.017	1.6
60%	2.2 +/- 0.0066	1.2 +/- 0.12	9.0 +/- 0.011	8

Table 3.4 – Inverted values for S/V, ρ_2 and G for each hematite mixture.

Figure 3.10 shows the surface area to volume ratio results for each hematite sample. Figure 3.10-A are the inverted S/V values with respect to the weight percent of hematite. Since the hematite had smaller grain sizes than the quartz, it would be expected that the S/V would increase with increasing hematite. There is a broad linear trend seen in the data. Figure 3.10-B are the inverted S/V values compared to the measured S/V values and the 1:1 line is shown. According to the measured values, the S/V is overestimated in each case.

Figure 3.11 illustrates the inverted surface relaxivities compared to the weight percent of the hematite. Figure 3.11-A are all of the data points and figure 3.11-B shows the data excluding the two points with large error at the hematite concentrations of 30 and 60 percent by weight. Both plots are included to illustrate the how the trends in the data change if the two points with significant error are not included. A ρ_2 saturation effect is evident from figure 3.11-A, but is not as obvious in figure 3.11-B.

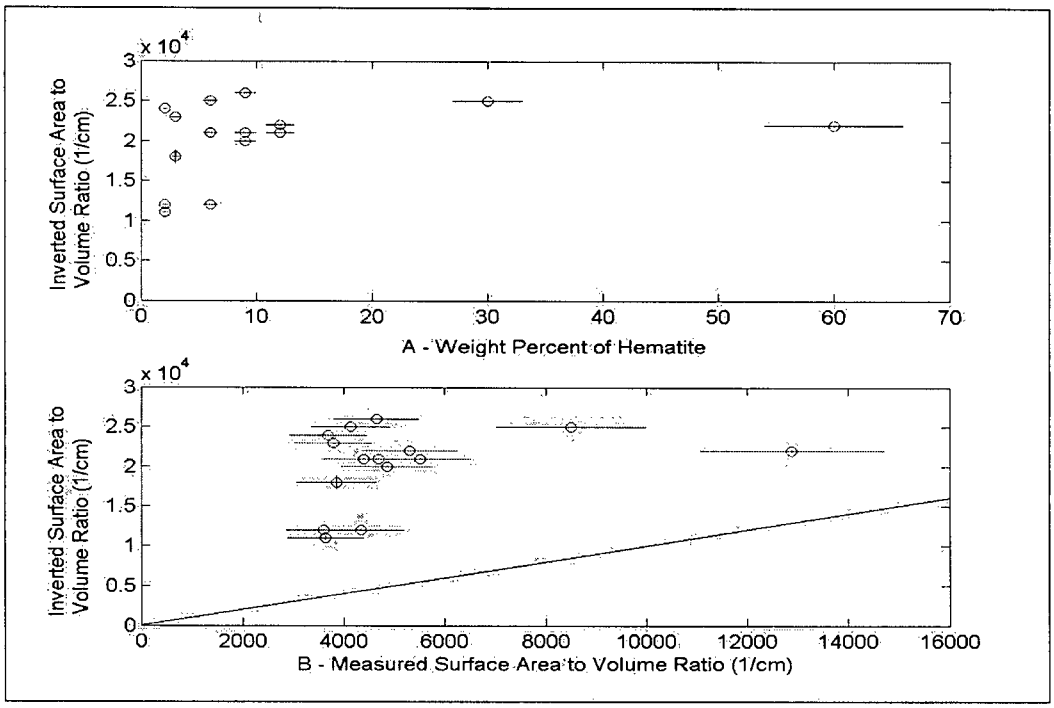

Figure 3.10 – Inverted surface area to volume ratios for each hematite mixture. Figure 3.10-A shows the results plotted against the weight percent of hematite and figure 3.10-B shows the values plotted against the measured surface area to volume ratio.

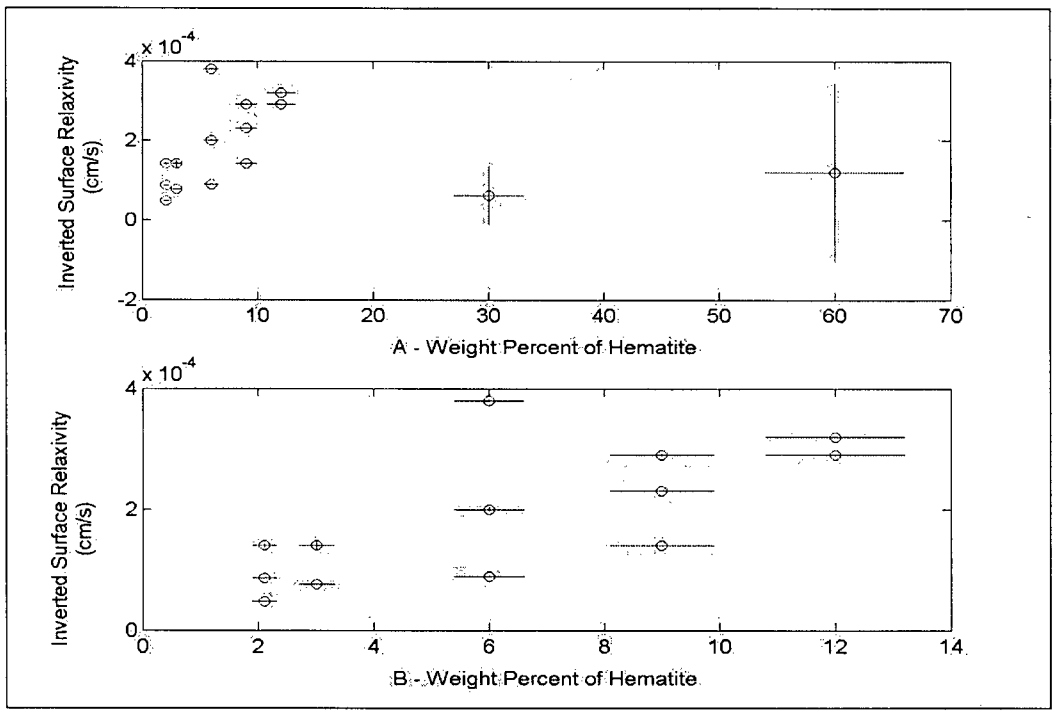

Figure 3.11 – Inverted T_2 surface relaxivities versus weight percent of hematite for each hematite mixture. Figure 3.11-A shows the results for all the mixtures, while figure 3.11-B shows the results for the data excluding the 30 and 60 percent by weight mixtures.

Figure 3.12 shows the relationship of the internal gradient compared with the weight percent of the hematite. There is an excellent linear trend between the two parameters.

3.4.3 - Hematite Data Discussion

In the synthetic data examples, we saw that the algorithm could predict the product of ρ_2 and S/V very well. The value of the internal gradient was also very well constrained for most realizations of noise. There were problems in extracting the individual values of ρ_2 and S/V resulting from the uncertainty in the data and the relative sizes of the three terms in the forward model. In the previous section, I showed that for the hematite data, more information on the particular values of ρ_2 and S/V is available. As a result, each unknown parameter will be discussed and evaluated individually.

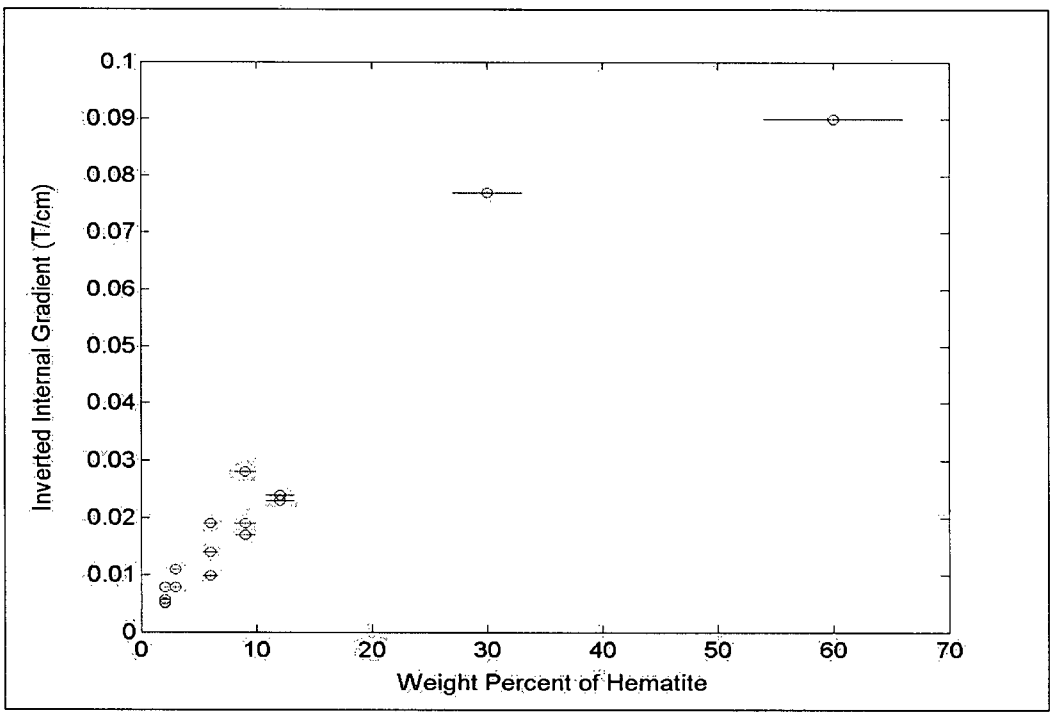

Figure 3.12 – Inverted internal gradient versus the weight percent of hematite for each hematite mixture.

3.4.3.1 - Surface Area to Volume Ratio

According to figure 3.10-B, the inverted S/V values are notably higher than were expected based on the surface area measurements of the samples, ranging from 1.1×10^4 1/cm to 2.6×10^4 1/cm compared with the measured values of 3.6×10^3 1/cm to 1.3×10^4 1/cm. These discrepancies must be a consequence of either the samples or the forward model and algorithm.

In terms of the hematite mixtures, the measured S/V values are merely estimates based on surface area measurements on the pure minerals. It is possible that when the larger quartz grains were combined with the smaller hematite grains, the smaller grains may have in-filled the spaces between the larger grains causing the pore sizes to be smaller than would result from either of the two minerals alone. This would increase the surface area to volume ratio of the pore space overall, which is an effect that was not captured in the S/V calculation for each mixture.

It is also possible there may be some problems with the forward operator. Perhaps the surface area to volume ratio is not properly represented in this equation, causing erroneous values to be recovered.

3.4.3.2 - Surface Relaxivity

The inverted surface relaxivities range from 4.7×10^{-5} cm/s to 3.8×10^{-4} cm/s for the hematite samples. These values correspond well to results obtained by Dodge et al. (1995) who reported surface relaxivities between 1×10^{-4} cm/s to 3.9×10^{-4} cm/s, where the smaller value was for a rock sample with 2% Fe_2O_3 and the larger value corresponded to a 14% Fe_2O_3 sample. Figure 3.11-A shows that the surface relaxivity levels off, or saturates, which is consistent with the results from Chapter 2. This observation is based

on the two points with the largest associated error and the saturation effect is not as obvious when these two points are excluded as seen in figure 3.11-B. Nonetheless, the relaxivities increase as expected and have reasonable magnitudes. Finally, the ρ_2 values are between 1 and 4 times larger than the measured ρ_1 values of Chapter 2, which approximately coincides with expectations (Kleinberg et al., 1993).

Both the inverted ρ_2 and S/V results show significant scatter in their relationships with the weight percent of hematite. This may be partly due to the inability of the forward model to accurately separate the two parameters although as mentioned above, the values should be more reliable than was shown for the synthetic data.

3.4.3.3 - Internal Gradient

The internal gradient values are between 5.1×10^{-3} T/cm to 9.0×10^{-2} T/cm. Hurlimann (1998) who presented the maximum effective gradients possible based on the susceptibility difference between the grain and pore fluid, showed the gradient resulting from the hematite could be as high as 1 T/cm for samples in a 5.5×10^{-2} T magnetic field. The field strength used in the NMR instrument was 2.2 T and hence, according their approximation the internal gradient in a pure hematite sample could be as large as 45 T/cm. The samples used in this experiment however were hematite mixed with quartz and the internal gradient measured is an average value and therefore not expected to be this high. Hurlimann (1998) also showed maximum effective gradients for some typical sandstones ranged from 1.9×10^{-3} T/cm to 0.18 T/cm at a magnetic field strength of 5.5×10^{-2} T, which corresponds to effective gradients of 7.6×10^{-2} T/cm to 7.2 T/cm at a

2.2 T field. Recalling that these values are maximum quantities, they correspond well with the internal gradients shown in figure 3.12.

There is also an excellent linear trend between the internal gradient and the weight percent of hematite. This would be expected as this single value for the internal gradient represents the internal gradients experienced by every proton in the system. As more hematite is added, more protons will experience the large gradient resulting from the susceptibility difference between the hematite grains and the pore fluid, as opposed to the weaker gradient resulting from the quartz grains.

Based on the internal gradient values coinciding with theoretical and measured values and on the excellent linear trend with hematite content, I believe this value is very well constrained by the inversion, similar to the results for the synthetic data.

3.5 - CONCLUSIONS

In this chapter, the objective was to develop a parameter estimation inversion algorithm capable of simultaneously estimating the T_2 surface relaxivity, surface area to volume ratio and internal gradient of rocks and sediments. Realization of this objective was limited, however the results suggest it is a promising method of determining these parameters.

The same hematite samples used in Chapter 2 were utilized to test the algorithm. Most of these samples were expected to have significant internal gradients that would affect the T_2 value. Slijkerman and Hofman (1998) are the only group to have used this type of inversion. They solved for the surface relaxivity and the surface area to volume

ratio and assumed that internal field inhomogeneities due to susceptibility differences were negligible. They applied an external magnetic field gradient as the value of G.

The algorithm developed for this study used a Newton solution with a line search to solve for the three NMR parameters ρ_2, S/V and G. Applying the algorithm to a synthetic data set indicated that G could be reliably recovered as could the product of ρ_2 and S/V for most noise realizations, but the two values could not be separated into the individual terms. There was some constraint on the potential values, as there appeared to be an upper limit for S/V and a lower limit for ρ_2. The ability of the algorithm to resolve ρ_2 and S/V depends on the sizes of the three terms in the forward model and will therefore depend on the value of each parameter and on the range of the echo times used for measurement.

For the hematite data, the values of each of the parameters are expected to be more reliable as information from each term in the forward model was available. There were differences between the S/V that was inverted and that which was measured. It was discussed that these discrepancies could be partly explained by differences in the grain sizes of the hematite and the quartz. In addition, the overestimation of this parameter could be a result of inaccuracies in the forward model.

This technique shows some potential for interpreting T_2 data and recovering the surface area to volume ratio. It can currently predict the internal gradient and the product of ρ_2 and S/V extremely well in the presence of noise.

I would like to see further experiments completed using larger ranges of echo times to extract the maximum amount of information from the forward model. It may be possible to identify ideal echo times for different rock types, with different properties,

that optimize the amount of information that can be obtained. Variation in the usable echo times may be limited due to the short time approximation of the diffusion coefficient that is incorporated in the forward model and this must be dealt with for a given S/V.

In addition, the forward model requires some study to identify any potential weaknesses and to understand its applicability to rocks with different geometries. Completing experiments on materials in which the S/V, ρ_2 and G are very well known and using appropriate echo times will indicate whether or not the forward model is suitable. Finally, the errors on the inverted parameters could be improved by incorporating error due to the forward model.

4 - FINAL SUMMARY

In conclusion, two methods for estimating the surface area to volume ratio of a pore space from NMR measurements were developed. Magnetic susceptibility was shown to correlate well with the T_1 surface relaxivity and could potentially be used to predict ρ_1 in a borehole setting. The S/V of the porous material under investigation could then be calculated using equation 1.2. Implementation of this technique would facilitate the remote calculation of permeability.

In addition, the manner in which the surface relaxivity of hematite and magnetite varied with mineral content was quantified. The magnetite showed a linear trend with weight percent, while the hematite surface relaxivity became saturated at large weight percents of the mineral. This was the first time NMR T_1 measurements and ρ_1 calculations were made for systematically varying concentrations of these two commonly occurring minerals. Furthermore, the surface relaxivities of ferrimagnetic magnetite compared to antiferromagnetic hematite were examined and measured. Magnetite was postulated to have larger ρ_1 values than hematite based on these measurements, suggesting ferrimagnetic minerals have larger surface relaxivities than antiferromagnetic minerals.

The second half of this thesis involved the development of an inversion algorithm to simultaneously estimate ρ_2, S/V and G from T_2 data. The algorithm was tested on synthetic data and the hematite and quartz T_2 data. The success of this algorithm was variable. For almost every realization of noise, the product of surface relaxivity and the surface area to volume ratio could be reliably determined, as could the internal gradient.

However, the individual values of ρ_2 and S/V could only be resolved under some circumstances. Although a similar inversion was completed by Slijkerman and Hofman (1998) who solved for ρ_2 and S/V, this study extended the technique to solve for the internal gradient as well. The inversion code shows potential for obtaining the surface area to volume ratio from T_2 data, but requires more work to fully realize its abilities and limitations.

REFERENCES

Bard, Y., 1974, Non-Linear Parameter Estimation: Academic Press.

Beveridge, G.S.G., and Schechter, R.S., 1970, Optimization: Theory and Practice: McGraw-Hill Book Company.

Borgia, G.C., Brown, R.J.S., and Fantazzini, P., 1996, Nuclear Magnetic Resonance Relaxivity and Surface-to-Volume Ratio in Porous Media With a Wide Distribution of Pore Sizes: Journal of Applied Physics, **79**, 3656-3664.

Bourbie, T., Coussy, O., and Zinszner, B., 1987, Acoustics of Porous Media: Gulf Publishing Co.

Brownstein, K.R., and Tarr, C.E., 1979, Importance of Classical Diffusion in NMR Studies of Water in Biological Cells: Physical Review A, **19**, 2446-2453.

Bryar, T.R., Daughney, C.J., and Knight, R.J., 2000, Paramagnetic Effects of Iron(III) Species on Nuclear Magnetic Relaxation of Fluid Protons in Porous Media: Journal of Magnetic Resonance, **142**, 74-85.

Carmichael, R.S., Ed., 1989, Practical Handbook of Physical Properties of Rocks and Minerals: CRC Press, Inc.

Carr, H.Y., and Purcell, E.M., 1954, Effects of Diffusion on Free Precession in Nuclear Magnetic Resonance Experiments: Physical Review, **94**, 630-638.

Chang, D., Vinegar, H., Morriss, C., and Straley, C., 1997, Effective Porosity, Producible Fluid, and Permeability in Carbonates from NMR Logging: The Log Analyst, **38**, 60-72.

Chitale, D.V., Day, P.I., and Coates, G.R., 1999, Petrophysical Implications of Laboratory NMR and Petrographical Investigation on a Shaly Sand Core: 74th Annual Technical Conference and Exhibition Proceedings, Society of Professional Engineers, 607-625.

Clark, D.A., 1997, Magnetic Petrophysics and Magnetic Petrology: Aids to Geological Interpretation of Magnetic Surveys: AGSO Journal of Australian Geology and Geophysics, **17**, 83-103.

Collinson, D.W., 1983, Methods in Rock Magnetism and Palaeomagnetism. Techniques and Instrumentation: Chapman and Hall.

Cukauskas, E.J., Vincent, D.A., and Deaver, B.S., 1974, Magnetic Susceptibility Measurements Using a Superconducting Magnetometer: Review of Scientific Instrumentation, **45**, 1-6.

REFERENCES

Deer, W.A., Howie, R.A., and Zussman, J., 1992, An Introduction to the Rock-Forming Minerals, 2nd Ed.: Longman Scientific and Technical.

Dodge, W.M.S., Shafer, J.L., and Guzman-Garcia, A.G., 1995, Core and Log NMR Measurements of an Iron-Rich Glauconitic Sandstone Reservoir: 36th Annual Logging Symposium Transactions, Society of Professional Well Log Analysts, O1-O12.

Domenico, P.A., and Schwartz, F.W., 1998, Physical and Chemical Hydrogeology, 2nd Ed.: John Wiley and Sons, Inc.

Ellis, D.V., 1987, Well Logging for Earth Scientists: Elsevier.

Foley, I., Farooqui, S.A., and Kleinberg, R.L., 1996, Effect of Paramagnetic Ions on NMR Relaxation of Fluids at Solid Surfaces: Journal of Magnetic Resonance, Series A, **123**, 95-104.

Garcia, A.L., 1994, Numerical Methods for Physics: Prentice-Hall.

Glasel, J.A., and Lee, K.H., 1974, On the Interpretation of Water Nuclear Magnetic Resonance Relaxation Times in Heterogeneous Systems: Journal of the American Chemical Society, **96**, 970-978.

Griffiths, D.J., 1989, Introduction to Electrodynamics, 2nd Ed: Prentice-Hall.

Hinedi, Z.R., Chang, A.C., Anderson, M.A., and Borchardt, D.B., 1997, Quantification of Microporosity by Nuclear Magnetic Resonance Relaxation of Water Imbibed in Porous Media: Water Resources Research, **33**, 2697-2704.

Hurlimann, M.D., Helmer, K.G., Latour, L.L., and Sotak, C.H., 1994, Restricted Diffusion in Sedimentary Rocks. Determination of the Surface Area to Volume Ratio and Surface Relaxivity: Journal of Magnetic Resonance, Series A, **111**, 169-178.

Hurlimann, M.D., 1998, Effective Gradients in Porous Media Due to Susceptibility Differences: Journal of Magnetic Resonance, **131**, 232-240.

Kenyon, W.E., and Kolleeny, J.A., 1995, NMR Surface Relaxivity of Calcite with Adsorbed Mn^{2+}: Journal of Colloid and Interface Science, **170**, 502-514.

Kenyon, W.E., 1997, Petrophysical Principles of Applications of NMR Logging: The Log Analyst, **38**, 21-43.

Kleinberg, R.L., and Horsfield, M.A., 1990, Transverse Relaxation Processes in Porous Sedimentary Rock: Journal of Magnetic Resonance, **88**, 9-19.

Kleinberg, R.L., Farooqui, S.A., and Horsfield, M.A., 1993, T_1/T_2 Ratio and Frequency Dependence of NMR Relaxation in Porous Sedimentary Rocks: Journal of Colloid and Interface Science, **158**, 195-198.

Kleinberg, R.L., Kenyon, W.E., and Mitra, P.P., 1994, Mechanism of NMR Relaxation of Fluids in Rock: Journal of Magnetic Resonance, Series A, **108**, 206-214.

Kleinberg, R.L., and Vinegar, H.J., 1996, NMR Properties of Reservoir Fluids: The Log Analyst, **37**, 20-32.

Krauskopf, K.B., and Bird, D.K., 1995, Introduction to Geochemistry, 3rd Ed: McGraw-Hill, Inc.

Latour, L.L., Kleinberg, R.L., and Sezginer, A., 1992, Nuclear Magnetic Resonance Properties of Rocks at Elevated Temperatures: Journal of Colloid Interface Science, **150**, 535-548.

Latour, L.L., Mitra, P.P., Kleinberg, R.L., and Sotak, C.H., 1993, Time-Dependent Diffusion Coefficient of Fluids in Porous Media as a Probe of Surface-to-Volume Ratio: Journal of Magnetic Resonance, Series A, **101**, 342-346.

Latour, L.L., Kleinberg, R.L., Mitra, P.P. and Sotak, C.H., 1995, Pore Size Distributions and Tortuosity in Heterogeneous Porous Media: Journal of Magnetic Resonance, **112**, 83-91.

McNeill, J.D., Hunter, J.A., and Bosnar, M., 1996, Application of a Borehole Induction Magnetic Susceptibility Logger to Shallow Lithological Mapping: Journal of Environmental and Engineering Geophysics, **0**, 77-90.

Meiboom, S., and Gill, D., 1958, Modified Spin-Echo Method for Measuring Nuclear Relaxation Times: Review of Scientific Instruments, **29,** 688-691.

Menke, W., 1984, Geophysical Data Analysis: Discrete Inverse Theory: Academic Press.

Mitra, P.P., Sen, P.N., and Schwartz, L.M., 1993, Short-time Behavior of the Diffusion Coefficient as a Geometrical Probe of Porous Media: Physical Review B, **47**, 8565-8574.

Mullins, C.E., 1977, Magnetic Susceptibility of the Soil and its Significance in Soil Science – A Review: Journal of Soil Science, **28**, 223-246.

Nabighian, M.N., Ed., 1987, Electromagnetic Methods in Applied Geophysics – Theory, Volume 1: Society of Exploration Geophysicists.

Nagata, T., 1961, Rock Magnetism: Maruzen Company Ltd.

Nesse, W.D., 1991, Introduction to Optical Mineralogy, 2nd Ed.: Oxford University Press.

Ramakrishnan, T.S., Schwartz, L.M., Fordham, E.J., Kenyon, W.E., and Wilkinson, D.J., 1999, Forward Models for Nuclear Magnetic Resonance in Carbonate Rocks: The Log Analyst, **40**, 260-270.

Raymond, L.A., 1995, Petrology: The Study of Igneous, Sedimentary and Metamorphic Rocks: WCB/McGraw- Hill.

Reynolds, J.M., 1998, An Introduction to Applied and Environmental Geophysics: John Wiley and Sons.

Roberts, S.P., McDonald, P.J., and Pritchard, T., 1995, A Bulk and Spatially Resolved NMR Relaxation Study of Sandstone Rock Plugs: Journal of Magnetic Resonance, Series A, **116**, 189-195.

Robertson, B., 1966, Spin-Echo Decay of Spins Diffusing in a Bounded Region: Physical Review, **151**, 273-277.

Rueslatten, H., Eidesmo, T., Slot-Peterson, C., and White, J., 1998, NMR Studies of an Iron-Rich Sandstone Oil Reservoir: International Symposium Proceedings, Society of Core Analysts, Paper SCA-9821, 1-10.

Scollar, I., Tabbagh, A., Hesse, A., and Herzog, I., 1990, Archaeological Prospecting and Remote Sensing: Cambridge University Press.

Singer, M.J., Verosub, K.L., Fine, P., and TenPas, J., 1996, A Conceptual Model for the Enhancement of Magnetic Susceptibility in Soils: Quaternary International, **34**, 243-248.

Slijkerman, W.F.J. and Hofman, J.P., 1998, Determination of Surface Relaxivity From NMR Diffusion Measurements: Magnetic Resonance Imaging, **16**, 541-544.

Song, Y-Q., 2000, Determining Pore Sizes Using an Internal Magnetic Field: Journal of Magnetic Resonance, **143**, 397-401.

Song, Y-Q., 2001, Pore Sizes and Pore Connectivity in Rocks Using the Effect of Internal Field: Magnetic Resonance Imaging, **19**, 417-421.

Strang, G., 1988, Linear Algebra and its Applications, 3rd Ed.: Harcourt Brace Jovanovich College Publishers.

Stucki, J.W., Goodman, B.A., and Schwertmann, U., 1985, Iron in Soil and Clay Minerals: D. Reidel Publishing Company.

Thompson, R., and Oldfield, F., 1986, Environmental Magnetism: Allen and Unwin.

Whittall, K.P., MacKay, A.L., 1989, Quantitative Interpretation of NMR Relaxation Data: Journal of Magnetic Resonance, **84**, 134-152.

Zhang, G.Q., Hirasaki, G.J., and House, W.V., 2000, Internal Field Gradients in Porous Media: 41st Annual Logging Symposium Transactions, Society of Professional Well Log Analysts, AA1-AA12.

APPENDIX A - NMR THEORY AND MEASUREMENT

THE BEHAVIOR OF PROTONS IN MAGNETIC FIELDS

Ellis (1987) provides an excellent introduction to the behavior of protons in magnetic fields, a summary of which is provided here. In classical terms, protons can be modeled as magnetic dipoles with an intrinsic angular momentum or spin. When exposed to an external static magnetic field, B_o, protons will align with the magnetic field lines. Because the angular momentum vector and the magnetic moment are coaxial, the interaction between the magnetic moment of the proton and the magnetic field result in the proton precessing about the external field. The frequency at which the proton precesses is referred to as the Larmor frequency and is directly proportional to the static field strength. The equation that defines the angular precession, w_L, is:

$$w_L = \gamma B_o \tag{A.1}$$

where γ is the gyromagnetic ratio of the proton and B_o is the external field strength. The Larmor frequency, f_L, is defined as:

$$f_L = \frac{w_L}{2\pi} \tag{A.2}$$

The precession about an external field results in the proton generating a magnetic field of its own (Griffiths, 1989). In the case of electron magnetization in matter, the induced magnetic dipole moment per unit volume (**M**) is proportional to the applied field strength (**H**) and is expressed as:

$$\mathbf{M} = k\mathbf{H} \tag{A.3}$$

where k is the magnetic susceptibility of the material being magnetized, and **H** in linear media is related to **B** by:

$$\mathbf{B} = \mu \mathbf{H} \tag{A.4}$$

where μ is the permeability of the medium (Griffiths, 1989). Nuclear magnetization can be represented in a similar manner, but the magnitude of the induced magnetization is orders of magnitude less than that for electrons. As a result, proton magnetization cannot be measured directly. Magnetic susceptibility is further examined in Appendix B. The behavior of the induced magnetization of protons in the presence of static and time varying magnetic fields is the basis of NMR measurements.

NMR MEASUREMENTS

In the NMR measurements made in this study, the static magnetic field is applied to a porous, water filled rock or sediment sample. The protons within the sample are allowed time to align in the direction of the field, taken to be along the z-axis in three-dimensional space. A second, weaker alternating magnetic field is then applied 90° to the primary field and is referred to as a radio frequency or rf pulse. The frequency of this second field is selected to match the Larmor frequency of the protons. The protons begin to precess around this second field in addition to the precession around the static field. Figure A.1 depicts the movement of the magnetic dipoles in the presence of the two fields. **M** represents the net magnetization of all the protons. Figure A.1-A is the motion of the proton in the stationary lab frame in which the second field is oscillating at the same frequency as the proton. Figure A.1-B shows the motion of the proton if it is

observed from a frame of reference that is rotating at the Larmor frequency. The effect of the alternating field, illustrated in figure A.1-B, is to tilt the proton away from the direction of the static field. The duration of the rf pulse controls the angle at which the proton is tilted.

There are two NMR relaxation time constants, T_1 and T_2. T_1, or the longitudinal time constant, is characteristic of the build-up of magnetization in the direction of the static field, upon removal of the secondary alternating field. It is a measure of the return of the magnetization vector to align with the static field. In typical T_1 measurements, a tilt angle of 180° is used and is called an 180° pulse. The second time constant, T_2, is the transverse relaxation time and represents the decay of magnetization in the plane perpendicular to the static magnetic field. To best observe this relaxation, T_2 measurements tilt the magnetization by 90°, placing the magnetization vector in the x-y plane if the static field is oriented along z. The rf pulse in this case is known as a 90° pulse. Upon removal of the alternating field, in addition to the magnetization vector re-aligning with the static field, the protons will spread out or "dephase" in the x-y plane.

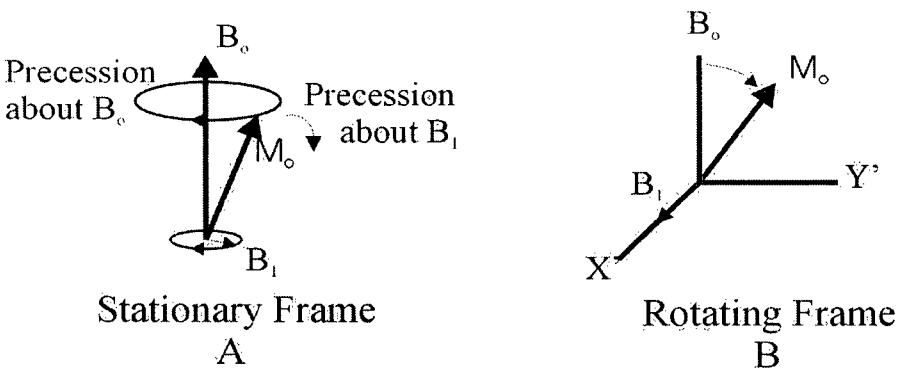

Figure A.1 – Motion of a magnetic dipole in the presence of a static field and a weaker alternating field. Stationary and rotating frames of reference are shown. Reproduced from Ellis (1987).

The decay of the magnetization due to this dephasing is characterized by the time constant T_2. Figure A.2 shows the orientation of the protons in the rotating frame of reference, in the plane perpendicular to the static field. Figure A.2-A shows the orientation of the protons with B_o, pointing out of the page, before the alternating field has been applied. Figure A.2-B shows the position of the protons, represented by the arrow, immediately after the 90° pulse. Figure A.2-C depicts the dephasing effect some time after the alternating field is removed. The re-alignment of the protons with B_o will also result in a decrease in the net magnetization in the x-y plane.

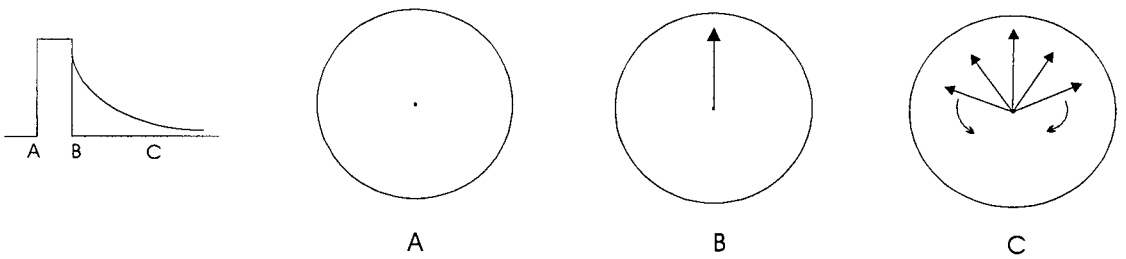

Figure A.2 – The components of the magnetization vector during an NMR experiment. Reproduced from Ellis (1987).

MEASUREMENT OF T_2

The method used to measure T_2 will be described first as the T_1 measurement technique extends directly from the T_2 description. Referring to figure A.1-A, when the magnetization vector is tilted by 90°, it rotates about the z-axis, in the x-y plane. Motion of the magnetization vector will induce an alternating current in a pick-up loop. Due to the dephasing of the spins, the magnetization decays in the x-y plane causing the alternating signal to decay. Intuitively, one might expect the decay of the magnetization to be characterized by T_1, but since the dephasing of the protons in the x-y plane occurs much faster than the return of the magnetization to the z-axis, it is T_2 that is measured by the coil. Strictly speaking, the relaxation time measured by the coil is called T_2^*. It includes the processes illustrated in equation 1.8, in addition to any dephasing due to inhomogeneities in external field, not to be confused with magnetic field inhomogeneities caused by susceptibility differences of the grains and pore fluid. The time constant representing the dephasing effects resulting from the characteristics of the sample, is called T_2.

A special pulse sequence called the Carr-Purcell-Meiboom-Gill (CPMG) sequence is used to cancel the effects of the external field inhomogeneities and reduce the effects of the internal field inhomogeneities (Carr and Purcell, 1954; Meiboom and Gill, 1958). Initially, the protons are placed in the static field long enough to ensure the magnetization is completely aligned. Next a 90° pulse is applied, followed by a wait time, τ. An 180° pulse is then applied and again τ is allowed to elapse. The amplitude of the sinusoid in the coil is then measured, referred to as the echo. The pulse sequence for one echo is:

$$90^o - \tau - 180 - \tau - echo$$

(Carr and Purcell, 1954 and Meiboom and Gill, 1958). The echo time t_e, is defined as 2τ. This sequence is repeated for many echoes and is denoted as:

$$90^o - \tau - \left[180^o - t_e\right]$$

where the echo is measured half way through each t_e. The physical explanation for this is as follows: After the 90° pulse, the protons are allowed to dephase for τ, this is followed by an 180° pulse which inverts the direction of motion of the dipole moments of the protons. This causes them to dephase in the opposite direction for another τ before the amplitude of the signal is acquired. The goal of this sequence is to attempt to reverse the effects of the dephasing by diffusion in the internal gradients. Dephasing due to surface interactions are irreversible (Kleinberg and Vinegar, 1996) and are therefore unaffected by the pulse sequence. As can be seen by examining equation 1.8, as the echo time approaches zero, the diffusion term also approaches zero. The diffusion term cannot be completely removed by this procedure, but for small echo times and low field strengths, the term can be assumed to be negligible.

MEASUREMENT OF T_1

Since the receiver coil cannot directly measure T_1, a procedure called inversion recovery must be used. The sample is placed in the static magnetic field for a sufficient amount of time to allow the magnetization to equilibrate. An 180° pulse is then applied and the magnetization is inverted. A wait time, t, follows to allow some longitudinal relaxation. A final 90° pulse is then applied to position the net magnetization in the x-y

plane, where it is allowed to decay, at a rate of $1/T_2^*$. The peak amplitude of the signal is recorded. This procedure is repeated for several values of t, to map the progression of the longitudinal relaxation. Peak amplitude is plotted against t and the resulting curve (if measuring water relaxing in a single pore) is defined by:

$$M(t) = m\left[1 - 2\exp\left(\frac{-t}{T_1}\right)\right] \tag{A.5}$$

(Ellis, 1987), thereby defining the T_1 of the system.

APPENDIX B - MAGNETIC SUSCEPTIBILITY: PROPERTIES AND MEASUREMENT

MAGNETIC SUSCEPTIBILITY THEORY

Unless otherwise specified, the following section is based on theory described by Griffiths (1989).

Magnetic susceptibility, k, is a fundamental property of materials that relates the magnetic dipole per unit volume, or magnetization, **M**, of a material due to an applied magnetic field, **H**, to the magnitude and direction of that field:

$$\mathbf{M} = k\mathbf{H} \tag{B.1}$$

Magnetic fields arise from the movement of electric charges. Electrons spinning on their axes and orbiting around nuclei create the current that generates magnetic fields in matter. The Biot-Savart law describes the magnetic field produced by steady line currents:

$$\mathbf{B}(P) = \frac{\mu_o}{4\pi}\int\frac{\mathbf{I}\times\hat{\mathbf{r}}}{\mathbf{r}^2}dl \tag{B.2}$$

where **B**(P) is the magnetic field at a point P that is a distance **r** from the length element dl of a wire in which the current **I** is flowing. In the case of electrons, dl is a length element of the path of the electron. μ_o is the permeability of free space. In matter, each electron spinning on its axis generates a magnetic field and can be represented as a tiny dipole. In many materials, every electron exists as one half of a pair and the two are aligned anti-parallel to each other. The resultant magnetic fields are consequently canceled out. Some substances contain one or more unpaired electrons in each atom, but

due to the random orientation of the atoms, the magnetic fields also cancel each other out. However, in the presence of an external magnetic field some of the dipoles of the unpaired electrons will align with the field and the effect is a net magnetization.

The overall induced magnetic field in a substance due to each of these magnetic dipoles, together represented as a bound current, as they are polarizing as opposed to physically moving, can be calculated by summing the vector potential (**A**) of all of the dipoles:

$$\mathbf{A} = \frac{\mu_o}{4\pi} \int \frac{\mathbf{M} \times \hat{\mathbf{r}}}{\mathbf{r}^2} d\tau \tag{B.3}$$

where **M** is the magnetic dipole per volume element τ and **r** is the distance from the volume element. The vector potential is a quantity that arises from the properties of the static magnetic field. The divergence of the magnetic field is given by Maxwell's second equation:

$$\nabla \cdot \mathbf{B} = 0 \tag{B.4}$$

and allows the definition of the vector potential. A vector identity states that the divergence of a curl must equal zero, therefore there must be some vector potential, **A**, such that:

$$\nabla \cdot (\nabla \times \mathbf{A}) = 0 \tag{B.5}$$

where

$$\mathbf{B} = \nabla \times \mathbf{A} \tag{B.6}$$

By defining the vector potential of a material using equation B.3, which is dependent on the magnetization vector as a result of the external magnetic field, which in turn is dependent on the magnetic susceptibility, the magnetic field due to the induced

magnetization can be calculated. This is an important phenomenon, and is imperative to measuring magnetic susceptibility.

The discussion to this point has dealt only with materials that obey equation B.1 and are called paramagnets, which exhibit small positive magnetic susceptibilities on the order of 1.0×10^{-7} m^3/kg to 1.0×10^{-6} m^3/kg. In these types of substances each dipole acts independently from every other dipole. The net magnetization resulting from the alignment of the dipoles in the external magnetic field is only maintained while the external field is present. Upon removal of the field, thermal agitation quickly causes the dipoles to become randomly oriented. While exposed to the external field, thermal agitation and the torque exerted by the external magnetic field work against one another and the magnetic susceptibility is consequently dependent on temperature. This is known as the Curie law of paramagnetic susceptibility (Collinson, 1983). The magnetic susceptibility of paramagnetic materials can theoretically be calculated by:

$$k = \frac{\mu_B^2}{3RT}\left[\left(xP_B^2(Fe^{2+}\right) + yP_B^2(Fe^{3+}) + zP_B^2(Mn^{2+})\right] \qquad \text{(B.7)}$$

where μ_B is the Bohr magneton, which is equal to $9.274\text{x}10^{-24}$ J/T. R is the universal gas constant, T is the temperature, x, y and z are the gram ion numbers of each ion, and P_B is the effective Bohr magneton number for each ion, which are approximately 5.25-5.53 and 5.58 for Fe(II) and Fe(III) respectively (Nagata, 1961).

Substances that do not obey equation B.1 are non-linear. A common non-linear material is a ferromagnet. These substances do not require an external magnetic field to maintain magnetic alignment. They can sustain what is known as remanence, which is a result of an interaction between adjacent dipoles, causing them to align in the same direction. These patches of magnetized dipoles are called domains. Usually in a

multidomained material, which is the situation for this study, each domain is randomly oriented and the substance as a whole has no net magnetization. It should be noted that there could be some preferential alignment along one of the crystallographic axes. In an external magnetic field, the domain boundaries will shift, favouring the domain with the magnetization closest to the direction of the external field. At large inducing fields, this process is irreversible and upon the removal of the field, the induced magnetization will be maintained for a period of time.

The magnetic susceptibility of a ferromagnet refers to a differential increase in **M** as a result of a differential increase in **H**. Thus, k is not a constant, but rather a function of **H**. At low magnetic field strengths, shifts in the domain walls can be approximated as reversible and the magnetic susceptibility can be approximated as constant (Collinson, 1983). The susceptibilities of ferromagnets are positive and much larger than for paramagnets, on the order of 1.0×10^{-4} m^3/kg to 1.0×10^{-3} m^3/kg.

Antiferromagnetism is similar to ferromagnetism except in a single domain, the magnetic dipoles are aligned in an anti-parallel manner. The susceptibilities of these materials are comparable to paramagnets and hematite is an example of an antiferromagnetic material. In nature, ferromagnetism occurs very rarely. Minerals that can hold remanence tend to be ferrimagnetic, which means the moments in the domains are aligned anti-parallel, but the magnetization is stronger in one direction than the other, resulting in a net magnetization of each domain (Collinson, 1983). Magnetite is a ferrimagnetic mineral and the susceptibilities of it and other ferrimagnets are comparable to ferromagnetic materials. Figure B1 illustrates the positions of the domains for these three types of magnetism.

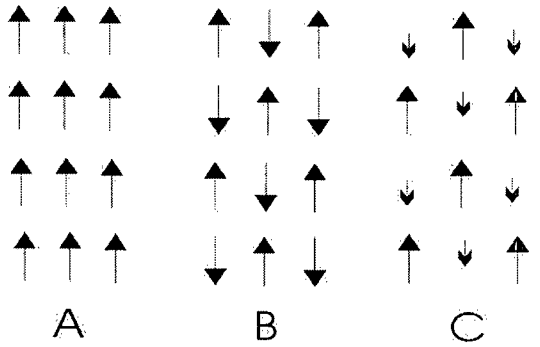

Figure B.1- Magnetic moments in ferromagnetic (A), antiferromagnetic (B), ferrimagnetic (C) matter. Reproduced from Reynolds (1998).

The magnetic field generated by a non-linear material in the presence of an external magnetic field will be the sum of the magnetization due to the external field plus the component of the remnant magnetization in the direction of the external field.

The final type of magnetization that occurs in matter is diamagnetism. Diamagnetic materials are linear and obey equation B.1. This phenomenon is a result of the external magnetic field altering the velocity of the electron around the nucleus, which in turn alters the orbital dipole moment, as opposed to the spin dipole moment, which is the cause of the other types of magnetization discussed above. The result is the orientation of the nuclear dipoles in such a way as to oppose the applied field. The magnetic susceptibility of diamagnets is negative, on the order of -1.0×10^{-8} m^3/kg. Although all materials will exhibit diamagnetism, it is much weaker than even paramagnetism and is therefore only observed in materials with paired electrons, such as quartz.

At low magnetic field strengths, the induced magnetization resulting from an applied field can be estimated as reversible for all types of magnetization and the magnetic susceptibility is called the initial magnetic susceptibility (Collinson, 1983). This is the susceptibility that was measured and analyzed in this study.

MAGNETIC SUSCEPTIBILITY MEASUREMENT

There are several methods used to measure magnetic susceptibility that use either direct, or alternating applied fields. Magnetic susceptibility in this study was measured using a Superconducting QUantum Interference Device (SQUID) magnetometer. The theory and mechanics of a SQUID are extremely complex and the following is merely a brief overview.

There are four pick-up loops wound as shown in figure B.2. A static magnetic field is set up around the sample, inducing some magnetization. The sample traverses from completely outside the bottom loop, to completely outside the top loop. There is a change in flux in each of the loops as the sample goes from one loop to another. Flux (ϕ) is defined as:

$$\phi = \int \mathbf{B}_o \cdot d\mathbf{a} \tag{B.8}$$

where **a** is the cross-sectional area of the loop. When the coil has several turns, the total flux is the product of the flux through one turn and the total number of turns. The field generated by the sample as a result of the inducing field is proportional to the magnetic susceptibility and the flux through the coils is dependent on this field strength. Thus, the magnetic susceptibility can be estimated by this procedure.

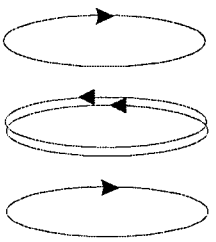

Figure B.2 – Schematic diagram of the orientation of the pick-up loops used in the SQUID magnetometer. Arrows indicate the direction each loop is wound.

The flux change due to the sample movement through the pickup loops induces a current in the coils as:

$$emf = -\frac{d\phi}{dt} \tag{B.9}$$

where emf is the electromotive force on the charges in the coil due to the flux change. Then:

$$I = \frac{emf}{R} \tag{B.10}$$

where I is the current induced in the coil due to the flux change resulting from the sample movement. The movement of charge though the pickup loop generates a magnetic field and there is a corresponding flux change through the weakly linked superconducting ring and a current is induced in it as well (Cukauskas et al., 1974). The ability of the pickup loops to transfer energy to the weakly linked superconducting ring, which actually measures the flux change, depends on the self-inductance of each of the coils and the mutual inductance between the two coils.

The theory behind the superconducting ring and its ability to measure the magnetic field is quite in depth and requires a considerable understanding of superconducters. Collinson (1983) provides a basic account of how the system works. The superconducting ring is cooled to below its critical temperature, which is the point at which the substance becomes superconducting, in the presence of an external field. If the external field then changes, causing a corresponding flux change, a current will be induced in the ring that induces a field that exactly cancels the change in flux, which is proportional to the magnetic susceptibility. It is desirable for the superconducting ring to be able to record very small changes in the field. This is accomplished by reducing the

diameter of the superconducting ring in one area to a very small value (1 μm), which is known as the Josephson weak link or the Josephson junction. One property of superconducters is that they have a critical current, which when exceeded causes the material to lose its superconducting ability. The weak link allows the critical current to be exceeded by extremely small currents, specifically, currents induced by a single flux quanta (magnetic flux has discrete values, or quanta). The actual method of measuring these flux changes is by superimposing a driving alternating field on the external field and the superconducting ring that has an amplitude large enough that the current density is exceeded. When the critical current is exceeded, flux quanta enter the ring, as the current in the ring is no longer perfectly countering the change in flux. The change in flux is detected by voltage spike in another pickup coil. Finally, when the external field changes due to the sample, the point at which the superconducting ring becomes resistive changes, and the output voltage also changes, which is characteristic of the field change due to the sample and therefore the susceptibility of the sample. This type of setup is called an rf SQUID and the driving frequency is usually between 20 MHz and 30 MHz.

This measurement technique is obviously very complex, but allows extremely accurate measurements of the flux changes to be made. Susceptibilities of about 1×10^{-12} SI can be resolved using this instrument.

Some clarification of the different susceptibilities referred to in the literature is required. The initial magnetic susceptibility was defined above as being the magnetic susceptibility measured at low field strengths. The intrinsic, or true, magnetic susceptibility and the observed and measured magnetic susceptibility are equivalent in paramagnetic and diamagnetic materials but this is not the case for ferromagnetic,

ferrimagnetic and antiferromagnetic minerals. In these substances the applied magnetic field is altered by what is known as a demagnetizing field, which arises from magnetic poles forming at each end of the sample due to the magnetization. This field is characterized by a demagnetizing factor (**N**), which is completely dependent on the shape of the grain. For an isolated grain the field inside the particle is:

$$\mathbf{H}_i = \mathbf{H} - \mathbf{NM} \tag{B.11}$$

or

$$\mathbf{H}_i = \mathbf{H} - \mathbf{N}k_i\mathbf{H}_i \tag{B.12}$$

where k_i is the intrinsic susceptibility. Then the observed susceptibility is the ratio of the magnetization to the applied field:

$$k = \frac{k_i \mathbf{H}_i}{\mathbf{H}} \tag{B.13}$$

Materials with low intrinsic susceptibilities will only show small differences between the intrinsic and observed susceptibilities. Magnetite however, has a large intrinsic magnetic susceptibility and the two values could be quite different depending on the magnitude of the demagnetizing field. Collinson (1983) reports that the demagnetizing fields in hematite are very small and the intrinsic susceptibility is what is measured, similar to paramagnetic materials.

There are also different ways to express the observed magnetic susceptibility. Volume susceptibility (k) is the dimensionless quantity and is the value defined by equation B.1. It is known as the volume susceptibility because it relates the magnetization per unit volume (**M**) to the external field strength. **M** and **H** have the same units and therefore the volume susceptibility is dimensionless. Quite often, susceptibility

is reported as the mass susceptibility which has the SI units m^3/kg, this can be obtained from the volume susceptibility by dividing by the density of the sample. The mass susceptibility was the parameter used in this study, but can be easily converted to volume susceptibility.